Insights into the sources and processes influencing atmospheric particulate reactive nitrogen species using stable isotopes

A thesis submitted in partial fulfilment of the requirements

for the degree of

Doctor of Philosophy

by

Chandrima Shaw

(Roll No. 20330006)

With the guidance of

Prof. Neeraj Rastogi

Geosciences Division

Physical Research Laboratory

Ahmedabad, India

Discipline of Earth Sciences

Indian Institute of Technology Gandhinagar, India

2025

DECLARATION

I, Chandrima Shaw, solemnly declare that this thesis titled "**Insights into the sources and processes influencing atmospheric particulate reactive nitrogen species using stable isotopes**" is the result of my own work, pursued with the guidance of Prof. Neeraj Rastogi. All sources consulted or referred to have been duly cited and acknowledged within this document. I affirm that this work has not been submitted elsewhere for any other degree or qualification. Furthermore, I declare that all contributions from co-authors, if any, have been appropriately acknowledged and credited. Any assistance received in preparing this thesis from individuals or institutions has been acknowledged in the text or listed in the acknowledgments section. I understand that any violation of academic integrity, including plagiarism or misrepresentation of facts, can lead to severe consequences, including the revocation of this degree.

Date: 26/08/2025

Place: Ahmedabad

Chandrima Shaw

Chandrima Shaw

(Roll No. 20330006)

Discipline of Earth Sciences
Indian Institute of Technology, Gandhinagar
Gujarat-382355

CERTIFICATE

It is certified that the work contained in the thesis titled "**Insights into the sources and processes influencing atmospheric particulate reactive nitrogen species using stable isotopes**" by Ms. Chandrima Shaw (Roll no: 20330006) has been carried out under my supervision and that this work has not been submitted elsewhere for a degree. I have read this dissertation, and I believe it is fully adequate, in scope and quality, for the degree of Doctor of Philosophy.

Date: 26-08-2025

Prof. Neeraj Rastogi
(Thesis Supervisor)
Geosciences Division,
Physical Research Laboratory
Ahmedabad India

Acknowledgement

I would like to express a heartfelt gratitude to my supervisor, Prof. Neeraj Rastogi without whom this thesis would have been impossible. I never intended on joining him initially being from a pure Geology background, but it turned out it was probably one of the best decisions for my PhD. He gave me the freedom to pursue a topic I wanted although it was new for him and gave efforts (maybe more than me) to understand it. Most remarkably, he taught me how to handle rejections gracefully. Being a long time, (I will say) survivor of clinical depression, getting a supportive supervisor with whom I could maintain complete transparency was a blessing. I thank him for bearing with me the past 4 years and congratulate him for this thesis as his efforts behind it is no less than mine.

I also like to thank my DSC members, Dr A.K Sudheer, Dr. Vineet Goswami and Prof. Harish Gadhavi for their valuable feedbacks and comments during my DSC seminars which *have enriched the quality of my research work. I also thank everyone in the Computer Centre in PRL for always listening and solving my problems be it Wi-Fi or a forgotten or expired password.*

I express my deepest thanks to my collaborative partners, Prof. Sanjeev Kumar (PRL), Prof. Prasanta Sanyal (IISER Kolkata), Dr. Atinderpal Singh (Delhi University) and Dr. Arup Borgohain (NESAC, Umiam). Without their contributions and immense support, my work would have been incomplete. I also thank Swati and Ritwick for helping me out in samplings and analysis. I would also extend my gratitude towards all members in the Chemistry lab, which felt like home for the past 4 years. I thank all my seniors, Punnet, Deva and Anil bhaiya for helping me out whenever I needed. I would also like to thank Rohit for helping me out on everything that is within his scope, be it teaching instruments to sampling to introducing me to the series Squid Game, which became my all-time favourite.

I will be forever gratefully to the doctors of PRL, Dr. Samir Dani and Dr. Sheetal Patel for making sure I was well and helping me whenever I needed, time didn't matter. I would also thank Dr. Ankita for making sure I was not cleaning or thinking too much. I remember her word "If you people, who are pursuing the highest degree hesitate to talk about mental health, what will happen to us then?" She is right, education let alone a PhD is meaningless if it fails to broaden our mind far beyond the existing societal norms and judgements. Once I started sharing, self-acceptance and healing came on its own.

The past five years would have been pretty dull without my batchmates, Kamran, Dharmendra, Debashish, Guru bhai, Trinesh, Aditya, Sanjay, Arup, Mallika. Spending time

with these folks, be it smashing birthday cakes to doing non senses, brought immense joy and laughter.

I would like to mention Akanksha for being with me for the past five years. Her continuous support, annoyance, nagging, complaining, listening, giving advices (some pretty useful, other useless) became a daily part of my life during this time. From doing each other's nails, hairs and makeups to wasting money on unnecessary stuffs and pretty bad movies, these past five years have been filled with countless memories. I hope we keep going like this, with you still spilling food on my bed.

I would also like to express my heartfelt gratitude towards my parents and brother, who supported me through every failure and success. One can never truly thank their own family enough, for this bond goes far beyond words of gratitude. I would also like to mention my boyfriend for being with me during my worst for the past one decade and accepting me for who I am. From figuring out structural geology to figuring life, from failing entrance exams together to qualifying side by side, we have shared countless ups and downs over the last ten years. I truly hope we continue to share our lives in the coming days. Oh, and guess what, I found a grey hair on my head today. Maybe that's the universe saying it's time we tie the knot… say, in a month or two??

I guess I should thank myself too, for dragging myself to work with a broken leg (I was oblivious of the broken bone), turning recovery into a DIY experiment, and somehow juggling depression and deadlines. Not perfect, not graceful, but somehow, I survived.

This acknowledgement will be incomplete without mentioning my four-legged fur babies (Zoro, Hanchi, Noori, Madhuri, Kuttu), each of whom brought sunshine to the gloomiest days.

Abstract

Reactive nitrogen (Nr) species, like NH_3, NO_x and their particulate counterparts NH_4^+ and NO_3^-, are important components of the atmosphere. They play a pivotal role in the formation of $PM_{2.5}$, perturbation of nutrient cycles, air quality degradation, and climate feedbacks. Recent satellite-based observations have identified India as a global hotspot for Nr. Despite the increasing trend in NH_3 and NO_x emissions over India, there is lack of a comprehensive understanding of the sources and formation mechanisms of Nr on a regional and seasonal scale. The present work focuses on understanding the behaviour, sources, and formation pathways of Nr using stable isotopic signatures of NH_4^+($\delta^{15}N$ of NH_4^+), NO_3^-($\delta^{15}N$ and $\delta^{18}O$ of NO_3^-), sensitivity regime and critical pH framework. A multi-site approach was adopted to capture the contrasting meteorological and emission conditions in the Indo-Gangetic Plain, western and the northeastern India.

Sensitivity regimes based on existing aerosol pH and liquid water content (ALWC) revealed that over most of the regions, HNO_3 to NO_3^- partitioning was the limiting factor in influencing PM levels. The sensitivity regime was also affected by fine dusts, as observed over Ahmedabad during summer, where non-volatile cations (NVCS) from dusts enhanced the pH and shifted the regime towards HNO_3 sensitivity. Further, a good agreement between the sensitivity regime derived from theoretical pH and partitioning factor at a fixed ALWC and that obtained from the actual existing pH and ALWC was observed. This revealed that the transition within sensitivity regimes was driven mainly by aerosol pH, whereas ALWC controlled the shift from sensitivity to insensitivity. The effects of meteorology (temperature and relative humidity) on the $\delta^{15}N$-NH_4^+ revealed two contrasting scenarios. Temperature and relative humidity influenced $\delta^{15}N$-NH_4^+ negatively and positively, when NH_4^+ existed in stable form as $(NH_4)_2SO_4$, this was observed over Ahmedabad(summer) and Patiala(post-monsoon). The effects were reversed, as low relative humidity and high temperature resulted in elevated $\delta^{15}N$-NH_4^+ over Delhi and Patiala during winter. This was due to the presence of NH_4^+ as semi-volatile species NH_4NO_3, where low relative humidity and elevated temperature caused volatilization loss. This resulted in the isotopic enrichment of the residual particulate NH_4^+. Source apportionment of NH_3 using $\delta^{15}N$-NH_4^+ and MixSIAR revealed regional and seasonal variations. Over Patiala, where winter sowed

a high contribution of NH_3 from coal-fired power plants (CFPPs), post-monsoon showed enhanced emissions from biomass burning and agricultural activities. Agricultural and urban wastes dominated NH_3 emission over Delhi during the post-monsoon. A shift in source profile was observed in winter, which was dominated mainly by combustion-related sources. Ahmedabad also revealed a similar seasonal shift in NH_3 sources, where winter was primarily dominated by combustion-related emissions and summer by emissions from urban and agricultural wastes. Increase in urban and agricultural emissions during summer was likely related to the high ambient temperature (~34°C), which favoured the volatilization of NH_3 from these sources. Agricultural emissions were the dominant source of NH_3 in both the northeastern sites, Dibrugarh and Shillong. This was related to the fact that both these regions are predominantly rural with high agricultural practices and livestock breeding.

Dual isotope of NO_3^- ($\delta^{15}N$ and $\delta^{18}O$) revealed its formation pathways over Patiala and Ahmedabad. In Patiala, the presence of day-time residual NO_3^- at night-time was observed. This was attributed to the presence of NO_3^- in stable compounds with NVCs, the occurrence of a shallow nocturnal boundary layer, and the higher atmospheric residence time of NO_3^- relative to the sampling duration. Over Ahmedabad, a significant diurnal shift in the formation pathways of NO_3^- was observed. Day-time showed a higher contribution of NO_3^- formed via OH oxidation, whereas night-time NO_3^- showed a higher contribution from heterogeneous hydrolysis involving N_2O_5. This was related to the low ambient temperature at night and the thermal sensitivity of N_2O_5. In contrast, no clear diurnal variability in NO_3^- pathway contributions were observed during summer, which could be attributed to a deeper boundary layer and enhanced vertical mixing, leading to greater diurnal homogeneity. Source apportionment revealed that traffic exhausts and biomass burning were the largest contributors, accounting for nearly 40% and 30% of total NO_x emissions over Patiala. Ahmedabad was marked by a seasonal trend in NO_x source. Traffic was the dominant contributor in winter, whereas summer showed nearly equal contributions from traffic exhausts and soil-related emissions. This seasonal trend reflected increased microbial activity in warmer months that enhances NO_x volatilization from urban and livestock waste as well as fertilized soils.

In conclusion, this thesis shows that reactive nitrogen formation and chemistry in India are shaped by meteorology, partitioning dynamics, sources and isotopic fractionation; these in turn vary spatially and temporally. The multi-site analysis

provides new insights into how sources of NH_3 and NO_x and formation pathways their particulate counterparts NH_4^+ and NO_3^- vary across different environments. These results contribute to a better scientific basis for air quality management and highlight the importance of nitrogen cycling for climate and ecosystem impacts.

Key words: Atmospheric Aerosols, Reactive nitrogen species, Sensitivity regime, Critical pH, $\delta^{15}N\text{-}NH_4^+$, Dual isotope of NO_3^-, MixSIAR, Source apportionment, Formation pathways, Meteorology.

Content

List of Figures

List of Table

Abbreviations & Symbols

ALWC:	Aerosol Liquid Water Content
BLH:	Boundary Layer Height
CCN:	Cloud Condensation Nuclei
CFPPs:	Coal-Fired Power Plants
CO:	Carbon Monoxide
CO_2:	Carbon Dioxide
CPCB:	Central Pollution Control Board (India)
DRH:	Deliquescence Relative Humidity
HONO:	Nitrous Acid
IGP:	Indo-Gangetic Plain
KNO_3:	Potassium Nitrate
MARGA:	Monitor for Aerosols and Gases in Ambient Air
MW:	Molecular Weight
NMB:	Normalized Mean Bias
NH_3:	Ammonia
NH_4^+:	Ammonium ion
NH_x:	Total ammonia ($NH_3 + NH_4^+$)
NH_3^T:	Total ammonia ($NH_3 + NH_4^+$)
NO:	Nitric Oxide
NO_2:	Nitrogen Dioxide

NO_3^- :	Nitrate ion
NO_x:	Oxides of Nitrogen (NO + NO_2)
NO_3^T:	Total nitrate (HNO_3 + NO_3^-)
NH_4NO_3:	Ammonium Nitrate
NH_4Cl:	Ammonium Chloride
$(NH_4)_2SO_4$:	Ammonium Sulphate
NOR:	Nitrate Oxidation Ratio
NVCs:	Non-volatile cations (e.g., Ca^{2+}, Mg^{2+}, K^+)
OH:	Hydroxyl Radical
O_3:	Ozone
PBL:	Planetary Boundary Layer
PM:	Particulate Matter
$PM_{2.5}$:	Particulate matter ≤ 2.5 µm
PM_{10}:	Particulate matter ≤ 10 µm
RH:	Relative Humidity
SCR:	Selective Catalytic Reduction
SIA:	Secondary Inorganic Aerosol
SO_2:	Sulphur Dioxide
SO_4^{2-} :	Sulphate ion
TSP:	Total Suspended Particulates
VOCs:	Volatile Organic Compounds

pH′: Critical pH for HNO_3 sensitivity

pH″: Critical pH for NH_3 sensitivity

f: Partitioning factor of NH_4^+ (fraction of NH_3^T in particulate phase)

$\varepsilon(NH_4^+)$: Equilibrium partitioning factor for NH_4^+

$\varepsilon(NO_3^-)$: Equilibrium partitioning factor for NO_3^-

fNO_3^-: Nitrate partitioning ratio (NO_3^-/NO_3^T)

$\delta^{15}N\text{-}NH_4^+$: Stable nitrogen isotope ratio of NH_4^+ particulate

$\delta^{15}N\text{-}NH_3$: Stable nitrogen isotope ratio of NH_3 gas

$\delta^{15}N\text{-}NO_3^-$: Stable nitrogen isotope ratio of NO_3^- particulate

$\delta^{18}O\text{-}NO_3^-$: Stable oxygen isotope ratio of NO_3^- particulate

R1–R7: Numbered chemical reactions referenced in the text

Chapter 1

Introduction

1.1 Overview of atmospheric Aerosols

Pollutants in atmosphere can be classified into two broad categories: gaseous and aerosols. Gaseous species like carbon monoxide (CO), ozone (O_3), nitrogen oxides (NO_x), and sulphur dioxide (SO_2) are among the most common air pollutants. In contrast, aerosols consist of tiny solid or liquid particles suspended in the atmosphere, encompassing a complex mixture of chemical constituents from different sources. While aerosols technically include both solid and liquid particles, the term particulate matter (PM) typically refers to the solid fraction, especially when discussing air quality. PM spans a broad range of sizes, starting from a few nanometres to several tens of micrometres in aerodynamic diameter, and typically resides in the lower troposphere for about a week (Seinfeld, 2016; Textor et al., 2006).

Aerosols can originate from both natural and anthropogenic sources. While natural sources include emissions from volcanic eruptions, sea spray, forest fires, and wind-blown dust; anthropogenic sources consist of biomass burning, vehicular emissions, industrial processes, agricultural activities etc. Once emitted into the atmosphere, these particles undergo chemical transformation as well as physical processing like coagulation, condensation, and evaporation, resulting in changes to their size and composition. Aerosols have relatively short life-time resulting in their strong spatial and temporal heterogeneity (Jacob et al., 1999). Despite their short residence times, aerosols play a critical role in modulating climate, atmospheric chemistry, visibility, public health, and nutrient cycling. They are removed from the atmosphere via dry and wet deposition, with the efficiency of removal dependent on particle size, where coarser particle tends to get removed faster than the finer ones.

Aerosols are typically classified based on their size, composition, and origin. Based on their sizes, aerosol can be coarse (≥2.5 μm), fine (0.1 to 2.5 μm), and ultrafine particles (≤0.1 μm). Coarse particles such as dust are generated by mechanical processes like erosion or grinding and generally exceed 1-2 μm in diameter.

Anthropogenic aerosols, which dominate in urban and industrial regions, tend to be finer in size and chemically more complex. These include components such as sulphate, nitrate, ammonium, chloride, sodium, mineral dust, trace metals, and water. Among them, sulphate, nitrate, ammonium, and certain transition metals are particularly significant due to their roles in radiative forcing, air pollution, human health risks, and atmospheric acidity (Cohen et al., 2017). The fine and ultrafine nature of these particles allows them to persist longer in the atmosphere and penetrate deep into the human respiratory system, making them especially concerning from a public health perspective.

1.2 Effects of aerosol

Aerosols influence Earth's climate through both direct and indirect effects (Figure 1.1). Direct effects include scattering or absorption of solar radiation by the particulates, thus affecting the Earth's radiative balance. Indirectly, aerosols influence the climate by altering microphysical properties of cloud, acting as cloud condensation nuclei (CCN) (Lohmann & Feichter, 2005). They can further affect cloud albedo, droplet number concentration, and precipitation efficiency. Since the late 20th century, growing evidence has shown that aerosols can also exert a cooling effect by reflecting incoming sunlight and enhancing cloud brightness, thereby partially offsetting the warming caused by greenhouse gases. The extent to which aerosols affect the radiative balance depends on their size, composition, shape, and refractive index, as well as environmental factors like relative humidity and surface reflectivity. While some aerosols, such as certain mineral dusts, absorb sunlight and cause warming others, like sulphate, nitrate, and ammonium, scatter sunlight, contributing to a net cooling effect (Rosenfeld et al., 2014). These processes influence regional temperatures, atmospheric stability, cloud formation, and precipitation patterns.

1.2.1 Air quality and Health

Aerosols, aside from their role in climate regulations, are critically important in shaping air quality and influencing human health. Finer particulates like $PM_{2.5}$, owing to their ability to enter deep into lungs and blood stream poses a severe risk in polluted regions like the Indo-Gangetic Plain. Once they enter the body, these particulates can cause a plethora of serious health conditions, like cardiovascular

diseases, chronic obstructive pulmonary disease (COPD), stroke, and lung cancer. In India alone, long term exposure to fine particulates is linked to nearly a million premature death per year (Cohen et al., 2017). To reduce these health impacts, the World Health Organization (WHO) recommends limiting 24-hour average $PM_{2.5}$ concentrations to no more than 15 µg/m³.

Aerosols are either emitted directly (primary aerosols) in the atmosphere or they can form secondarily through atmospheric chemical processes. Secondary formation happens when gases like SO_2, NH_3, and volatile organic compounds (VOCs) undergo oxidation and convert into particulate matter. These transformations are driven by homogeneous and heterogeneous reactions involving oxidants like ozone, hydroxyl radicals, and nitrogen oxides. Atmospheric aging through such reactions has been shown to significantly enhance the ability of the particles to induce oxidative stress and inflammation in biological systems (Kuhn et al., 2025; Patel & Rastogi, 2023; Singh et al., 2023). Understanding the evolving chemical nature of aerosols is therefore critical for evaluating their health effects and formulating effective air quality control measures. Recent studies have focused on the health impacts of $PM_{2.5}$ across different regions, like Europe, North America, and Asia. Early studies are typically based on community-level ambient $PM_{2.5}$ data from monitoring stations. This limited the exposure assessments to areas which were near those stations and provided only broad population-level estimates. However, recent advancements have shown a great improvement in spatial and temporal resolution of exposure modelling. These improvements are transforming epidemiological research and enhancing our

understanding of how long-term exposure to particulate pollution affects population health in diverse geographic settings (Shiraiwa et al., 2017).

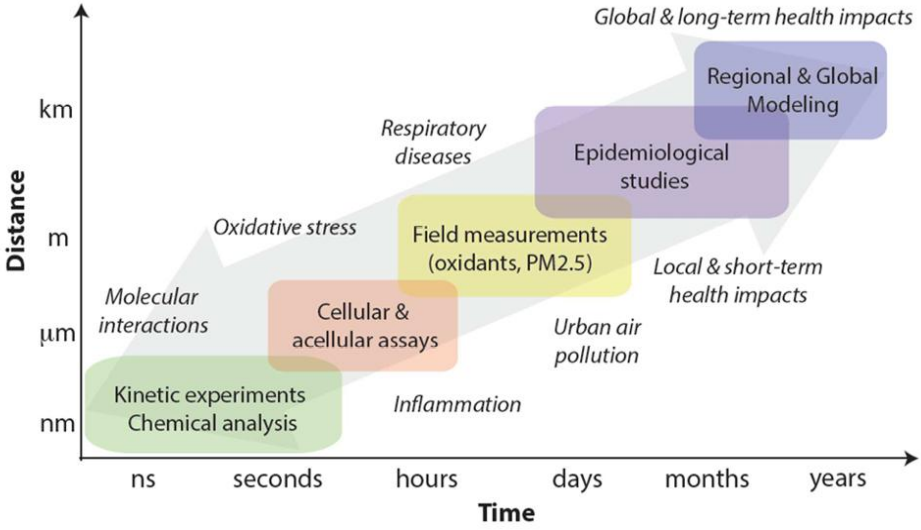

Figure 1.1. Aerosol health research spans diverse spatial and temporal scales, requiring an integration of physico-chemical and biomedical approaches (colored boxes) to understand the complex and multifaceted health impacts of aerosols (italicized terms highlight key aspects). Adapted from Shiraiwa et al. 2017

1.2.2 Biogeochemistry

In addition to the effects on climate and health, aerosols can also alter the biogeochemical cycling through deposition onto terrestrial and oceanic surfaces. These deposition processes can supply essential nutrients to sensitive ecosystems, where natural nutrient availability is low. For example, marine phytoplankton, which fix nearly half of global CO_2, often depends on nutrient inputs from aerosol deposition in remote oceanic regions (Srinivas & Sarin, 2013). Aerosol-derived nutrients originate from a combination of both natural and anthropogenic sources. While natural sources include mineral dust, volcanic emissions, wildfires, and biogenic particles, anthropogenic inputs come from agricultural and industrial emissions, fossil fuel combustion etc (Tomasi & Lupi, 2017; Viana et al., 2014). Further, atmospheric processing can also convert insoluble minerals into soluble, bioavailable forms via acid dissolution, organic ligands, or photochemical reduction (Ellison et al., 1999; Ito, 2015). Since the start of the industrial era, rapid growth in fossil fuel use and agricultural activities owing to increasing food and energy demand, has significantly

altered aerosol composition and increased the flux of nutrient-rich particles to the Earth's surface, especially over ocean basins.

Atmospheric deposition supplies nutrients like nitrogen, phosphorus, iron, and silicon to both land and ocean ecosystems. These inputs can influence phytoplankton growth and the amount of carbon transferred from the surface ocean to deeper waters (carbon export). Atmospheric nitrogen depositions, as NH_x and NO_x have increased post-industrial era owing to rapid growth in population, combustions and agricultural activities. Global NO_x deposition to the oceans has increased from about 6-7 Tg N per year in the 1860s to more than 20 Tg N per year in the 2000s, with projections of 25-36 Tg N per year by mid-century. Similarly, NH_x inputs have also risen from roughly 8-12 Tg N per year during pre-industrial era to around 18-25 Tg N per year today. Studies have shown that these atmospheric nitrogen inputs support over 20-25% of export production in some coastal and downwind regions, and account for around 5% of global ocean export production (Galloway et al.,2004; Denter et al., 2006; Luo et al., 2007). Iron, another important nutrient for marine photosynthesis and nitrogen fixation, is also supplied by aerosols via dust storms, biomass burning, combustion emissions etc. Additionally atmospheric deposition also supplies phosphorus and silicon to the ocean surface, although their contribution is less as compared to riverine sources. Globally, input of phosphorous to the ocean from riverine system is around 18-30 Tg P per year, while atmospheric dust transport contributes about 1 Tg P per year, roughly 3-5% of the total phosphorus input (Mahowald et al., 2008; Seitzinger et al., 2005). Similarly in case of silicon atmospheric depositions contribute around 0.2% of marine biogenic silica export. Although minor in global budgets, these atmospheric inputs can be ecologically significant in regions where dust transport coincides with low nutrient availability, such as parts of the subtropical oceans and some phosphorus-limited tropical ecosystems (Krishnamurthy et al., 2010; Luo et al., 2008). Over land, increase in nitrogen deposition stimulates plant growth in nitrogen-limited ecosystems, contributing an additional 0.24-0.7 Pg C per year to global terrestrial carbon uptake which is roughly equivalent to 2-8% of the annual land carbon sink. When combined with aerosol-derived phosphorus and iron, atmospheric deposition is estimated to increase global carbon storage by 0.2-1.5 Pg C per year. Moreover, aerosols also enhance acidity through sulphate and nitrate deposition. This could lead to soil acidification and nutrient leaching, thus supressing productivity over time. These simultaneous fertilising and degrading effects highlight the complex and still uncertain

role of aerosols in shaping long-term nutrient cycles and carbon-climate feedbacks (Thomas et al., 2010; Zaehle et al., 2010; Mahowald et al., 2011; Seitzinger et al., 2005).

1.3 Reactive Nitrogen Species (Nr) in the Atmosphere

Reactive nitrogen species (Nr) species are important components of atmospheric chemistry, playing a pivotal role in the formation of $PM_{2.5}$, perturbation of nutrient cycles, air quality degradation, and climate feedbacks. Unlike inert N_2, which constitutes nearly 78% of the Earth's atmosphere but remains largely non-reactive due to the presence of triple bond, Nr include all N-containing compounds that are chemically, biologically, or radiatively active (Fowler et al., 2013; Galloway & Cowling, 2002). These reactive forms include species like ammonia (NH_3), nitrogen oxides (NO and NO_2, collectively NO_x), nitrous oxide (N_2O) as gases and various reduced and oxidized compounds like ammonium (NH_4^+), nitrate (NO_3^-), and organic nitrogen (ON) as particulates (Liu et al., 2013). While N_2 is inert and biologically inaccessible without conversion by specialized microbes or anthropogenic processes, Nr interact dynamically with the atmosphere, biosphere, and hydrosphere. Their environmental lifetimes, transport behaviours, and transformation pathways are determined by their specific chemical forms, ranging from reduced species (e.g., NH_3, NH_4^+) to oxidized species (e.g., NO_x, HNO_3, NO_3^-, N_2O). This chemical diversity highlights the multiple roles of Nr in atmospheric reactivity, secondary aerosol formation, and deposition processes.

Among the Nr, NH_3 and NO_x are of particular importance due to their role as major precursors to secondary inorganic aerosols (SIAs). The SIAs enhance aerosol hygroscopicity, affect CCN formation and alter cloud albedo, which has severe impacts on regional climates (Allen et al., 2019; Ansari & Pandis, 2000; Arub et al., 2020; Liu, 2023). Nr in particulate forms from through gas-particle partitioning and neutralization reactions involving NH_3 and acidic species like hydrochloric acid (HCl), sulfuric acid (H_2SO_4) and nitric acid (HNO_3), the latter being an oxidation product of NO_x. The resulting NH_4^+ and NO_3^- salts contribute significantly to $PM_{2.5}$ mass in polluted regions (Chen et al., 2022; Pan et al., 2018; Song et al., 2019). Numerous studies, including satellite-based assessments, have confirmed that NH_3-NO_x interactions dominate the

chemical composition of fine aerosols in many parts of Asia, particularly over agricultural and urban-industrial sectors (Van Damme et al., 2018). Nr aerosols not only elevate the particulate burden but also influence a suite of atmospheric processes. Furthermore, the presence of NO_3^- and NH_4^+ modulate aerosol pH, a critical parameter governing heterogeneous chemistry, gas-particle partitioning, and trace metal solubility (Guo et al., 2016; Nenes et al., 2020, 2021).

Overall, Nr plays a dual role: on one hand, it is an essential nutrient and a crucial component of biogeochemical cycles; on the other, its excess in the atmosphere contributes to a wide range of environmental problems. The atmospheric behaviour of Nr, including their emissions, transformation to particulate forms, transport over local to continental scales, and eventual deposition, has profound implications for air quality, ecosystem health, agricultural productivity, and climate forcing (Galloway, 1998; Galloway et al., 1998, 2025). Understanding the formation, cycling, and impacts of Nr is therefore central to designing effective strategies for pollution mitigation and environmental management

1.3.1 Effects of Reactive Nitrogen (Nr)

1.3.1.1 Ecological effects

Excess deposition of Nr significantly alters terrestrial and aquatic ecosystems by disrupting natural nutrient balances. In terrestrial ecosystems, NH_3 and NO_x once converted to NH_4^+ and NO_3^-, can lead to oversupply of nutrients, favouring fast-growing nitrophilous species at the expense of slow-growing, native plants. This shift alters biodiversity and changes plant community composition (Payne et al., 2017; Porter et al., 2013). In aquatic environments, Nr runoff, especially as NO_3^-, triggers eutrophication. Elevated Nr inputs promote algal blooms, which deplete dissolved oxygen during decomposition, leading to hypoxic conditions, biodiversity loss, and in extreme cases, fish kills (Erisman et al., 2013). NH_4^+ can also be directly toxic to aquatic organisms at high concentrations, particularly in warm, poorly buffered water bodies (Zhu et al., 2022).

1.3.1.2 Climate Effects

Nr affect climate through both direct and indirect ways. N_2O a long-lived greenhouse gas with global warming potential approximately 298 times higher than CO_2 (IPCC, 2023), is produced from microbial nitrification and denitrification in soils and water bodies. Further, emission of other Nr species like NO_x contribute to the tropospheric O_3 formation, a short-lived climate forcer and pollutant that enhances radiative forcing and damages vegetations (Kleinman, 1994; Michalski et al., 2014; Sahu et al., 2012). Additionally, NH_3 and NO_x are precursors to major SIAs like ammonium sulphate ($(NH_4)_2SO_4$), ammonium nitrate (NH_4NO_3), ammonium chloride (NH_4Cl) etc. These aerosols influence Earth's radiative balance by scattering solar radiation and serving as CCN, thereby modifying cloud albedo and lifetime (Nenes et al., 2020; Seinfeld, 2016). The resulting impacts on cloud formation and precipitation patterns have implications for regional hydrology and climate feedback mechanisms.

Deposition of Nr also alters carbon dynamics in soil and hydrological ecosystems. In some systems, Nr addition can enhance plant growth and carbon sequestration, but prolonged exposure leads to soil acidification, reduced microbial activity, and carbon loss through increased respiration and leaching (de Vries, 2021).

1.3.1.3 Human Health Effects

Nr contribute directly and indirectly to multiple health issues. NO_x emissions, through their role in O_3 and SIA formation, are linked to respiratory and cardiovascular diseases, particularly in urban populations. Long-term exposure to $PM_{2.5}$, of which NH_4^+ and NO_3^- are important components, is associated with increased mortality, reduced lung function, and aggravated asthma (Nieder & Benbi, 2022). NH_3 exposure, though often underestimated, can cause mucosal irritation, coughing, and reduced respiratory efficiency, especially in areas with high agricultural emissions. Elevated NO_3^- concentrations in drinking water are linked to various chronic health risks, including colorectal cancer, thyroid dysfunction, and adverse reproductive outcomes (Martin et al., 1997; Peel et al., 2013; Shiraiwa et al., 2012). Furthermore, deposition of NH_4^+ and NO_3^- onto surfaces can lead to the formation of harmful secondary pollutants indoors and outdoors, increasing exposure risks. The health burden from Nr

is particularly high in regions with dense population and mixed emission sources, such as South and East Asia.

1.3.2 Sources of Nr

Nr in the atmosphere arises from both natural and anthropogenic sources. Natural emissions include microbial activity in soils and wetlands, lightning-induced NO_x production, biological nitrification- denitrification in water bodies and land, and volcanic emissions. In contrast, anthropogenic sources consist of emissions from agriculture-related fertilizer usage, urban/human wastes, livestock wastes, fossil fuel combustions, biomass burning industrial processes etc. While natural sources have long played a role in the nitrogen cycle, anthropogenic activities have dramatically intensified the input of Nr into the environment. Over the past few decades, global anthropogenic Nr emissions have surpassed natural contributions by several times, driven especially by the exponential increase in synthetic fertilizer production and fossil fuel use since the mid-20th century (Galloway et al., 2025; Galloway & Cowling, 2002). This human-induced alteration of the nitrogen cycle has led to widespread ecological and atmospheric impacts, necessitating a deeper understanding of Nr sources and transformations

1.3.2.1 Sources of NH_3

NH_3 is primarily emitted into the atmosphere from anthropogenic sources, like agricultural activities, livestock and urban wastes, biomass burning, transportation, and industrial combustion. In livestock wastes urea and uric acid present in manure and urine decompose under microbial action resulting in the release of NH_3. These emissions occur during storage, handling, and land application of manure and slurry, with the rate of release influenced by temperature, humidity, and pH (Casey et al., 2006; Wyer et al., 2022). Emission from fertilizer usage in agricultural activities is related to the urea-based compounds, which hydrolyse in soils to form NH_4^+. This NH_4^+ can volatilize to NH_3, particularly under high pH, warm temperatures, and dry conditions (Behera et al., 2015; Sommer et al., 2019; Vira et al., 2020; C. Zhang et al., 2017). Emissions also occur from urban waste streams, including open garbage bins, drains, and wastewater treatment plants, where nitrogen-rich organic matter decomposes and volatilizes as NH_3 (Casey et al., 2006).

Biomass burning, which is typically linked to NO_x emissions, can also release NH3, especially during the smouldering phase of incomplete combustion when temperatures are lower and oxygen supply is limited (Andreae & Merlet, 2001; Whitburn et al., 2015). The global annual NH_3 emissions from biomass burning are estimated to be ~ 4.53 ± 0.51 Tg, accounting for ~ 9% of global totals (Bray et al., 2021). Factors such as fuel nitrogen content and combustion temperature influence the amount of NH_3 emitted (Crutzen, 1979). Vehicular emissions and coal-fired power plants (CFPPs) are an emerging source of NH_3. NH_3 is released particularly from light- and medium-duty vehicles equipped with three-way catalytic converters (TWCCs). These systems can form NH_3 as a by-product of NO reduction reactions involving hydrocarbons or hydrogen (Y. Liu et al., 2021; Woo Jeong et al., 2024). Additionally, vehicles as well as CFPPs fitted with selective catalytic reduction (SCR) systems to reduce NO_x emissions release NH_3 when excess urea is injected or catalyst efficiency declines, a phenomenon known as "NH_3 slip" (Chang et al., 2022; Thiruvengadam et al., 2016; Koebel et al., 2000).

1.3.2.2 Sources of NO_x

NO_x is mainly released from combustion processes and microbial activity in managed soils and waste systems. Vehicular emissions are also an important source in urban populated settings. Vehicles emit NO primarily through high-temperature oxidation of N_2 during fuel combustion, which subsequently oxidizes to NO_2 in the ambient atmosphere. Emission magnitudes vary with fuel type, engine technology, and traffic density (Johnson & Joshi, 2018; Lozhkina & Lozhkin, 2016). CFPPs are another important source of NO_x, emitting through both thermal and fuel-based mechanisms. The high combustion temperature during combustion oxidizes N present in both atmosphere and coal fuel itself. Although emission control technologies such as SCR have been implemented, they do not always eliminate NO_x completely (Forzatti, 2001; Goel et al., 2015).

Biomass burning, including both natural forest fires, and anthropogenic post-harvest crop residue burning, releases substantial amounts of NO and NO_2. The nitrogenous compounds in plant matter are oxidised and released as NO_x during the combustion, with emissions depending on fire intensity and fuel characteristics (Galanter et al., 2000). Microbial processes in fertilized soils, urban compost sites, and

animal waste storage areas also emit NO_x. Nitrification and denitrification by soil bacteria convert NH_4^+ and NO_3^- to intermediate forms such as nitric oxide (NO), especially in moist, N-rich environments. Although these emissions are diffuse, they can be significant in areas with high fertilizer input or concentrated waste management practices (Vinken et al., 2014).

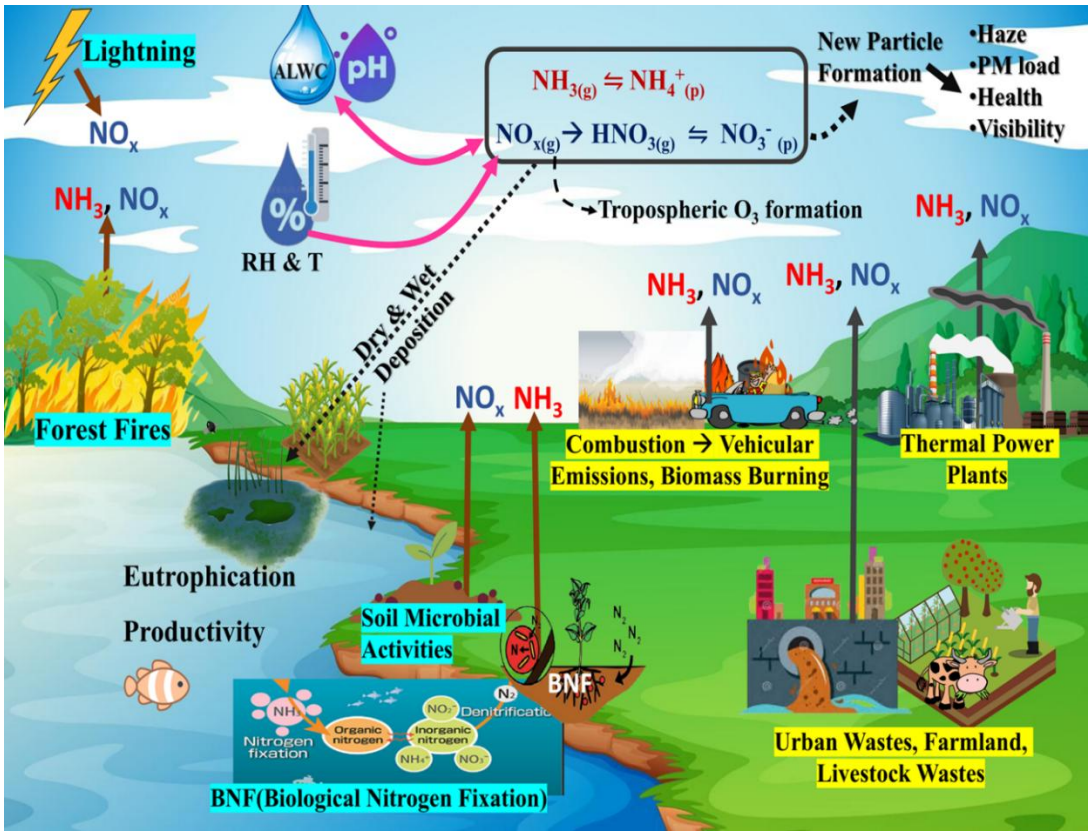

Figure 1.2. Schematic diagram Schematic showing sources, transformations, and atmospheric impacts of reactive nitrogen species

1.3.3 Formations of NH_4^+ and NO_3^-

NH_3 and NO_x are the dominant gaseous precursors of SIAs, contributing substantially to the fine particulate matter ($PM_{2.5}$) in the atmosphere. The conversion of these Nr gases into their particulate forms governs their atmospheric behaviour, including transport, residence time, and removal via deposition.

1.3.3.1 NH_4^+ formation

NH_3 is an alkaline, highly water-soluble gas that reacts readily with acidic species in the atmosphere, particularly H_2SO_4, HCl and HNO_3, resulting in the

formation of particulate-phase NH_4^+ salts such as $(NH_4)_2SO_4$ NH_4Cl and NH_4NO_3 (Walters et al., 2019). The conversion of NH_3 to NH_4^+, is governed by a reversible equilibrium involving its dissolution in water followed by protonation (R1). The formation of $(NH_4)_2SO_4$ is typically prioritized (R2), as it results in a non-volatile and chemically stable salt. Once the available SO_4^{2-} is neutralized, any remaining NH_4^+ (NH_4^+ excess) can react with other acidic species such as NO_3^- or/and Cl^- to form semi-volatile salts, like NH_4Cl and NH_4NO_3 (R3 and R4) (Behera et al., 2013; Renard et al., 2004; Scott & Cattell, 1978). The important reactions are as follow:

$$NH_3\ (g) + H_2O \leftrightharpoons NH_4^+\ (aq) + OH^- \quad \text{(R1)}$$

$$2NH_3(g) + H_2SO_4(g) \rightarrow (NH_4)_2SO_4\ (s) \text{ or } 2NH_4^+(aq) + SO_4^{2-}(aq) \quad \text{(R2)}$$

$$NH_3(g) + HNO_3(g) \leftrightarrow NH_4NO_3\ (s) \text{ or } NH_4^+(aq) + NO_3^-(aq) \quad \text{(R3)}$$

$$NH_3(g) + HCl(g) \leftrightarrow NH_4Cl\ (s) \text{ or } NH_4^+(aq) + Cl^-(aq) \quad \text{(R4)}$$

The atmospheric lifetime of NH_3 is relatively short, often a few hours, due to its rapid uptake and deposition (Asman, 1995). In contrast, particulate NH_4^+ can persist for several days, depending on meteorological conditions and aerosol properties. Its removal occurs through both wet and dry deposition: the former involves scavenging by raindrops or snowflakes, while the latter involves gravitational settling or impaction onto surfaces (Asman, 1995; Erisman et al., 2013).

1.3.3.2 NO_3^- formation and cycling

The conversion of NO_x to HNO_3 (g) and subsequently particulate NO_3^- starts with the rapid oxidation of NO to NO_2 and photolysis of NO_2 back to NO (R5-R7) (Figure 1.3). This cycle (known as Leighton cycle) exists in a photochemical steady state and results in the formation of tropospheric O_3 (Leighton, 1961).

$$NO + O3 \rightarrow NO_2 + O_2 \quad \text{(R5)}$$

$$NO_2 + hv \rightarrow NO + O\bullet \quad \text{(R6)}$$

$$O_2 + O\bullet + M \rightarrow O_3 + M \quad \text{(R7)}$$

Here, M represents a non-reactive species that can absorb the energy released to stabilize O. During daylight NO_2 reacts with hydroxyl (OH) radical and forms HNO_3 via Pathway 1 (P_1).

$NO_2(g) + OH + M \rightarrow HNO_3(g)$ (R8) *Pathway 1 (P_1)*

At night-time, when OH radicals are unavailable NO_2 reacts with O_3 and form higher oxides of N (N_2O_5) (R9 and R10) (Ahern et al., 2018; Aumont et al., 1999; Hu & Abbatt, 1996).

$NO_2 + O_3 \rightarrow NO_3 + O_2$ (R9)

$NO_2 + NO_3 \rightarrow N_2O_5$ (R10)

N_2O_5 forms HNO_3 either by hydrolysis on particle surface or by reaction with Cl^- via Pathway 2 (P_{2a}) and (P_{2b}) respectively.

$N_2O_5 + H_2O \rightarrow HNO_3$ (R11) *Pathway 2 (P2a)*

$N_2O_5 + Cl^- \rightarrow ClNO_2 + NO_3^-$ (R12) *(P2b)*

• NO_3+ VOCs $\rightarrow HNO_3$ (R13) *Pathway 3 (P3)*

$Cl + O_3 \rightarrow ClO + O_2$ (R14)

$NO_2 + ClO \rightarrow ClNO_3$ (R15)

$ClNO_3 + H_2O \rightarrow HOCl + HNO_3$ (R16) *Pathway 4(P4)*

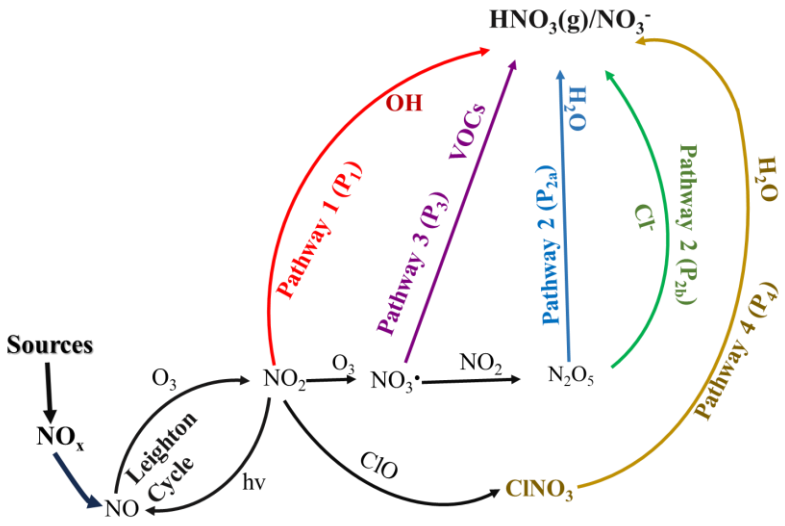

Figure 1.3. Major formation pathways of NO_3^- (via HNO_3) in the atmosphere

1.4 Stable Isotopes as Tools to Understand Sources and Formation pathways of Nr

The conversion of NH_3(g) to NH_4^+ involves phase change, during which isotopic fractionation occurs between the precursor (NH_3) and the product (NH_4^+). This gas-to-particle transformation is governed by exchange reactions involving equilibrium isotopic fractionation (R4) (Kirshenbaum et al., 1947; Savard et al., 2017; Thode & Urey, 1939; Urey et al., 1937). The formed NH_4^+ is isotopically enriched as compared to its gaseous precursor, with the degree of isotopic enrichment controlled by temperature dependent equilibrium fractionation factor. Additionally, factors such as meteorological conditions and the original source of NH_3 can influence the isotopic signature ($\delta^{15}N$) of the product (NH_4^+).

Different NH_3 sources are characterized by distinct $\delta^{15}N$ values, making it possible to trace their contributions using stable isotope analysis. For example, agricultural emissions typically have depleted $\delta^{15}N$ signatures (-25.1 ± 6‰), while combustion-related sources such as biomass burning (-12.3 ± 7‰) and coal-fired power plants (0.2 ± 7‰) tend to be more enriched (Chang et al., 2022; Li et al., 2023; Walters et al., 2020; Wu et al., 2021; H. Xiao et al., 2024). By accounting for the equilibrium isotope effects that occur during the gas-to-particle conversion, the $\delta^{15}N$ of particulate NH_4^+ can thus be used to infer the relative contributions of different NH_3 sources at a given location. Moreover, the additional fractionation that occurs during the NH_3 to NH_4^+ conversion offers insights into both the emission sources and the partitioning behaviour of NH_x in the atmosphere, making $\delta^{15}N$ a valuable tool for understanding reactive nitrogen dynamics.

Under typical atmospheric conditions, the isotopic signature of NO_3^- largely mirrors that of HNO_3(g) due to the rapid and reversible conversion that does not significantly alter the nitrate structure (Chang et al., 2018; Walters & Michalski, 2015; H. W. Xiao et al., 2020; Y. Zhu et al., 2021). The conversion of NO_x to HNO_3 involves isotopic fractionation of both nitrogen and oxygen, with the extent of oxygen isotopic fractionation ($\delta^{18}O$) providing key information on the dominant chemical pathways. NO_3^- formed via each pathway has a distinct isotopic signature due to variations in the incorporation of oxidant-derived oxygen, such as from OH and H_2O (e.g., in P_1 and P_2 pathways). Simultaneously, the nitrogen isotopic signature ($\delta^{15}N$) of NO_3^- is influenced

not only by the original $\delta^{15}N$ of NO_x emissions but also by the isotopic fractionation effects associated with the conversion processes (Luo et al., 2020; Michalski et al., 2012).

The $\delta^{15}N$ of NO_x varies significantly across sources, offering a means of distinguishing them. For example, emissions from CFPPs, biomass burning (BB), vehicular exhaust, and soil microbial activity exhibit average $\delta^{15}N$-NO_x values of 14.2 ± 4.4‰, 1.0 ± 4.1‰, -12.6 ± 3.9‰, and -35.4 ± 12.6‰, respectively (Felix et al., 2012; Felix & Elliott, 2014; Fibiger & Hastings, 2016; Walters, Goodwin, et al., 2015; Walters, Tharp, et al., 2015). When formation pathway contributions are considered, the associated nitrogen isotopic fractionation can be quantitatively accounted for. This allows for a more accurate estimation of the $\delta^{15}N$ of the NO_x, and, when combined with known source signatures, enables source apportionment of NO_x and thus NO_3^-. Beyond source attribution, isotopic composition also reflects chemical formation pathways. Thus, combining $\delta^{15}N$ and $\delta^{18}O$ in a dual-isotope framework allows to quantify the formation pathways and source contributions of NO_3^- (Alexander et al., 2020; Savarino et al., 2013).

1.4.1 Integrating Stable Isotopes and Bayesian Models for Tracing Sources of Nr

Major advancement in atmospheric nitrogen research lies in the incorporation of stable isotopic data with Bayesian mixing models like MixSIAR. While $\delta^{15}N$ and $\delta^{18}O$ offer source and pathway-specific signatures, Bayesian models enable quantitative source apportionment by incorporating these signatures along with observational uncertainties. This approach has been widely used for both NO_x and NH_3 by multiple existing studies across different locations to understand the sources and formations mechanisms of NH_4^+ and NO_3^- from their precursor (Bhattarai et al., 2021; Chang et al., 2018; Dong et al., 2022; Lin et al., 2021; Wu et al., 2021).

1.5 Advances, Current Understanding, and Research Gaps

Over the past few decades, considerable progress has been made in understanding the atmospheric chemistry of Nr especially over in North America and Europe. These studies have provided key insights into the sources, formation pathways, and isotopic signature of Nr (Elliott et al., 2007; Hastings et al., 2003; Morin et al., 2009). In recent years, research has increasingly shifted towards Asia, where emissions of NO_x and NH_3 are among the highest in the world. However, most of this research is concentrated in China. A growing number of studies in China have successfully combined isotopic data with atmospheric models to identify both emission sources and chemical formation mechanisms, offering a more complete picture of reactive nitrogen cycling in that region (Fan et al., 2023; Pan et al., 2018; Xi et al., 2023). In comparison to regions such as North America and Europe, South Asia (particularly India) remains significantly underrepresented in global studies on Nr, despite being a major hotspot for nitrogen emissions. In India, these emissions originate from a wide array of sources, including intensive fertilizer use, fossil fuel combustion, biomass burning, and urban waste. However, detailed investigations in this region are still scarce. A few limited studies over India have relied on bulk nitrogen isotope measurements (δ^{15}N-TN) to investigate the sources and atmospheric processing of Nr (Agnihotri et al., 2011; Bikkina et al., 2016; Rastogi et al., 2020; Sharma et al., 2015). This approach can introduce substantial uncertainties and potential biases, as δ^{15}N-TN reflects the combined isotopic signals of multiple nitrogen species, such as NH_4^+ and NO_3^-, and is influenced by their respective gas-particle partitioning and environmental factors associated with it. Additionally, many of these studies are often constrained to a single location, season, or bulk nitrogen form, which curb their ability to capture the full complexity of Nr cycling in the Indian atmosphere. This lack of comprehensive data is especially concerning given that India experiences some of the highest levels of air pollution globally and plays a significant role in the global nitrogen pollution burden.

Another critical limitation in current research is the inadequate consideration of gas-particle partitioning in both field observations and modelling approaches. The partitioning of Nr species, such as NH_3 and HNO_3, into their particulate forms (NH_4^+ and NO_3^-) is influenced by aerosol pH, temperature, and relative humidity (RH). These

factors also affect their formation pathways and even their isotopic signatures (Guo et al., 2017; Walters & Michalski, 2016). While thermodynamic models like ISORROPIA-II have improved our understanding of this partitioning process (Fountoukis & Nenes, 2007), most studies in South Asia still treat primary emissions and secondary aerosol formation as separately, overlooking the important interactions between them. This is a crucial issue in Indian settings, where high NH_3 levels and abundant aerosol water content makes partitioning processes dynamic. Furthermore, the uncertainty in emission inventories for Nr remains a major challenge, reducing the accuracy of chemical transport models and limiting the robustness of source apportionment efforts (Erisman et al., 2013). Altogether, there is a pressing need for more focused and detailed research on Nr in India. Given the region's diverse emission sources, complex meteorology, and severe air pollution, studies should aim to integrate isotopic measurements, gas-particle partitioning analysis, and improved regional emission inventories. Addressing these gaps is essential for developing an accurate understanding of nitrogen cycling and for designing effective air quality management strategies in one of the most affected parts of the world.

1.6 Rationale for the Present Study

The gaps outlined above clearly point to the requirements for region-specific and integrative studies on Nr in South Asia, particularly over India. While stable isotope techniques and atmospheric modelling have been widely applied in North America, Europe, and especially China, such combined approaches remain rare in the Indian context. This is concerning given India's high emissions, diverse sources, and complex seasonal dynamics.

This thesis is motivated to bridge the knowledge gap by providing a clearer picture of how Nr behaves in diverse Indian meteorological and atmospheric conditions. The study focuses on using stable nitrogen ($\delta^{15}N$) of $NH_4^+$and dual isotopes ($\delta^{15}N$ and $\delta^{18}O$) of NO_3^- to trace their emission sources and formation processes. By integrating these isotopic data with thermodynamic and mixing models like ISORROPIA-II) and MixSIAR, the study aims to link gas-phase precursors (NH_3 and NO_x) to the formation of particulate NH_4^+ and NO_3^- under diverse real-world conditions, across spatial and temporal scale.

The major objectives of this thesis are:

1. To examine how various meteorological and chemical factors influence the partitioning between NH_3 gas and NH_4^+ particulates spatially and temporally,
2. To determine the relative contributions of key NH_3 emission sources across diverse Indian regions using stable isotope analysis, and
3. To elucidate the major formation pathways of atmospheric NO_3^- and to identify the source contributions of its precursor NO_x across spatial and seasonal scales.

1.7 Thesis Outline

Chapter 1 introduces the background and significance of aerosols in the atmosphere, with a focus on Nr (NH_3, NH_4^+, NO_x, and NO_3^-). It discusses their environmental and climatic implications, reviews existing literature, identifies key knowledge gaps, and outlines the rationale, motivation, and objectives of the present study. **Chapter 2** details the methodology. It covers the measurement of major water-soluble ions and the isotopic analysis of $\delta^{15}N\text{-}NH_4^+$, $\delta^{15}N\text{-}NO_3^-$, and $\delta^{18}O\text{-}NO_3^-$. The chapter also describes estimation and modelling approaches, including the use of ISORROPIA-II for aerosol pH and partitioning calculations, validation of model outputs, and determination of critical pH. Subsequent sections include the estimation of $\delta^{15}N\text{-}NH_3$ from $\delta^{15}N\text{-}NH_4^+$, calculation of NO_3^- formation pathway contributions using $\delta^{18}O\text{-}NO_3^-$, and estimation of $\delta^{15}N\text{-}NO_X$ from measured $\delta^{15}N\text{-}NO_3^-$. Finally, Bayesian source apportionment is carried out using MixSIAR.

Chapter 3 presents the spatial and temporal patterns of gas-particle partitioning of Nr across five different regions in India. Using ISORROPIA-II outputs, it evaluates the influence of temperature, RH, aerosol pH, and liquid water content on $NH_3\text{-}NH_4^+$ and $HNO_3\text{-}NO_3^-$ partitioning. Sensitivity regimes are identified for each site, indicating the limiting precursors and key drivers of PM variability. **Chapter 4** focuses on the source apportionment of NH_3 and its conversion to $\delta^{15}N\text{-}NH_4^+$ across rural, urban, and semi-urban environments across different settings. Using $\delta^{15}N\text{-}NH_4^+$as a tracer and applying the MixSIAR model, it quantifies the contributions from agricultural wastes, traffic emission, biomass burning and CFPP, highlighting spatial differences in NH_3 emission profiles.

Chapter 5 investigates the formation pathways of NO_3^- and identifies the sources of its precursor NO_x using dual-isotope ($\delta^{15}N$ and $\delta^{18}O$) analysis. The study spans two sites and three seasons with day-night sampling. $\delta^{18}O\text{-}NO_3^-$ is used to assess

the relative contributions of various pathways, while $\delta^{15}N\text{-}NO_3^-$ and MixSIAR are employed to estimate NO_x contributions from traffic, soil, biomass burning, and CFPPs.

Chapter 6 summarizes the major findings of the thesis and discusses their broader implications for understanding nitrogen cycling and air quality in India. It also outlines directions for future research in the field of Nr and atmospheric aerosol chemistry.

Chapter 2

Methodology

2.1 Aerosol Sampling Sites

Aerosol sampling was carried out at multiple locations. Detailed information on the sampling period, geographic coordinates, sample types, number of samples, sampling frequency, and integration time are provided in Table 2.1. Description of sampling sites is provided below.

Table 2.1. List of sampling sites, site type sampled period, geographical location, sample type, number of samples (n), and frequency of sample collection

Sampling site	Site type	Sampling period	Geographical location and Altitude (m)	Sample type	Number of Samples (n)	Sampling frequency, Integration Time
Ahmedabad	Urban	Dec 2022-Jan 2023	23.04° N, 72.54° E; 50 AMSL	$PM_{2.5}$	46	Every alternate day (day/night), 12 Hrs
Ahmedabad	Urban	May 2023-June 2023	23.04° N, 72.54° E; 50 AMSL	$PM_{2.5}$	30	Every alternate day (day/night), 12 Hrs
Delhi	Urban	Oct 2023-Feb 2024	28.55° N, 77.19° E; 176 AMSL	$PM_{2.5}$	44	Every third day (day/night), 10 Hrs
Patiala	Semi-urban	Oct-Nov 2014	30.35° N, 76.44° E; 255 AMSL	$PM_{2.5}$	69	Daily (day/night), 10 Hrs
Dibrugarh	Semi-rural	Jan-May 2024	27.47° N, 94.93° E; 110 AMSL	$PM_{2.5}$	24	Every fourth day, 48 Hrs
Dibrugarh	Semi-rural	Jan-May 2024	27.47° N, 94.93° E; 110 AMSL	PM_{10}	24	Every fourth day, 48 Hrs
Umiam (Shillong)	Semi-rural	Jan-May 2024	25.67° N, 91.84° E; 980 AMSL	$PM_{2.5}$	24	Every fourth day, 24 Hrs

2.1.1 Patiala

Patiala is a semi-urban city located in the northwestern IGP, surrounded by expansive agricultural land. It lies between two significant geographic features, the Shivalik Hills to the east and the Thar Desert to the southwest, placing it in a region that routinely experiences intense agricultural activity and seasonal emissions. Sampling was conducted during the post-monsoon period, from 11th October to 16th November 2014, a time when open-field burning of crop residues is widespread across the IGP.

Each year, following the rice harvest, farmers across Punjab and neighbouring states such as Haryana and Uttar Pradesh burn leftover crop stubble to rapidly prepare their fields for the next sowing season, primarily wheat. This large-scale biomass burning is a dominant and recurring source of atmospheric pollution over the region, contributing significantly to elevated particulate matter levels and reactive nitrogen species during the post-monsoon months (Patel et al., 2021; Rastogi et al., 2016). Numerous studies have shown that this seasonal practice worsens air quality, leading to persistent haze and degraded visibility across northern India (Reisen et al., 2013; Yadav & Devi, 2019).

$PM_{2.5}$ samples were collected from the terrace of the Department of Physics, Punjabi University, Patiala. The sampling site was selected to avoid direct ground-level emissions while remaining representative of the surrounding urban-agricultural environment. The timing of the campaign coincided with the peak burning period, allowing for assessment of the direct and regional impact of crop residue combustion on aerosol composition.

2.1.2 Delhi

$PM_{2.5}$ sampling was done at Delhi University campus (28.55°N, 77.19°E; 176 m AMSL), located in the northern part of Delhi, one of the most polluted megacities in the world. According to a WHO survey of 1,600 world cities, Delhi ranks among the worst in terms of air quality. The city is under immense pressure due to rapid urbanization, industrial emissions, biomass burning, and one of the largest vehicular populations in the country, with nearly 10 million registered vehicles as of 2016-exceeding the combined total of Chennai, Mumbai, and Kolkata (http://www.delhi.gov.in/). Delhi is also the most populous city in India, with a current population of approximately 33 million (United Nations, https://population.un.org/wpp/), and ranks second globally after Tokyo. Diurnal sampling was conducted every third day, from 24th October 2023 to 12th February 2024. This period spans two distinct phases: the post-monsoon biomass burning season (October-November), followed by the winter season (December-February), when Delhi typically experiences the worst air quality levels due to persistent meteorological stagnation.

The sampling strategy was designed to capture both seasonal and diurnal variations in the sources and atmospheric processing of Nr. During October and November, extensive agricultural residue burning happens across the IGP, which significantly elevates aerosol loadings in Delhi through long-range transport of pollutants. In winter, local emissions from vehicles, coal and wood combustion, biofuel use, and industrial activities dominate. Additionally, low ambient temperatures, high RH, and shallow boundary layer heights during winter months enhance the accumulation and secondary formation of pollutants (Mishra et al., 2023; Puthussery et al., 2022; Rai et al., 2020)

This combination of seasonal emission sources and meteorological influences makes Delhi a critical location for understanding the formation and transformation of aerosol-phase reactive nitrogen. The diurnal sampling also enables assessment of differences driven by photochemistry and boundary layer dynamics, particularly in relation to gas-particle partitioning and secondary aerosol chemistry.

2.1.3 Ahmedabad

Ahmedabad (20.03°N, 72.54°E, 53 m AMSL), situated in the state of Gujarat, India, experiences a hot semi-arid climate with extremely hot summers and dry winters. The city has a population of around 8.5 million, making it the 7th most populous in the country (United Nations, https://population.un.org/wpp/). The Sabarmati River runs through the city and contributes to shaping its geographical features. $PM_{2.5}$ samples were collected from the rooftop of a multi-storey building (~50 m above ground level) at the Physical Research Laboratory (PRL), Ahmedabad, to reduce direct influence from nearby ground-level emissions. Sampling was carried out during two seasons: winter (1st December 2022 to 26th January 2023) and summer (9th May to 11th June 2023). In each season, samples were collected on alternate days, separately for day-time and night-time periods, with each sample representing a 12-hour duration.

The seasonal and diurnal resolution of sampling was critical for understanding how the sources and formation pathways of Nr species such NH_4^+ and NO_3^- vary with meteorological conditions. Changes in temperature, RH, and boundary layer height can strongly influence gas-particle partitioning, secondary aerosol formation, and chemical transformation processes. For example, winter conditions generally favour aerosol accumulation and gas-to-particle conversion due to lower temperatures and reduced

vertical mixing, while summer conditions promote dispersion and may enhance different chemical pathways. By capturing both seasonal and diurnal variability, the study aims to disentangle the roles of emission sources and atmospheric processes in shaping the reactive nitrogen budget over an urban environment.

2.1.4 Dibrugarh

Sampling of $PM_{2.5}$ and PM_{10} was conducted at Dibrugarh University (27.47°N, 94.93°E; 108 m AMSL), located in the city of Dibrugarh in Upper Assam, northeastern India. The region is characterized by a semi-urban to rural setting, with relatively low industrial activity but influenced by surrounding anthropogenic sources. The city itself has a modest population of approximately 138,000, while the surrounding district remains predominantly rural (Government of Assam, 2021).

Sampling was carried out from 25th January to 8th May 2024, encompassing the late winter to pre-monsoon season. A low-volume sampler was employed at this location, each sample was collected for 48 hrs, this extended duration was necessitated by the instrument's limited flow rate (~ 1 L min^{-1}). Though industrial activity is limited locally, the site is influenced by regional sources such as emissions from transportation of crude oil (primarily from fields in northeast Assam), seasonal biomass burning (including forest fires and crop residue burning), and vehicular traffic along national highways passing near the site. Its location, with the Himalayas to the north and hilly terrain in the east and south, allows for long-range transport of aerosols from the Indo-Gangetic Plain and the Bay of Bengal, while preventing intrusion of dry, cold air masses from central Asia (Gogoi et al., 2011; Pathak et al., 2012). Thus, Dibrugarh offers a unique perspective compared to more urbanized environments.

2.1.5 Shillong

$PM_{2.5}$ sampling for Shillong was conducted at the North Eastern Space Applications Centre (NESAC) situated in the Ri-Bhoi district of Umiam, Meghalaya (25.67°N, 91.84°E; ~980 m AMSL). The site lies in the central part of the state and represents a semi-rural, forested region influenced by both local biogenic activity and long-range transport. The site is situated within the NESAC campus, offering a relatively clean background setting, with limited direct anthropogenic sources in the immediate vicinity. Sampling was carried out from 25th January to 8th May 2024 using

a high-volume air sampler. This sampling window spans late winter to the pre-monsoon season, enabling assessment of seasonal variations in reactive nitrogen species in a less industrially impacted region of northeast India. The Shillong dataset serves as an important contrast to more urbanized locations, aiding in the understanding of atmospheric processing under low-pollution, high-humidity conditions typical of the northeast (Government of Meghalaya, 2019).

2.2 Instruments and analysis

2.2.1 Particulate matter sampling

The ambient PM samples with aerodynamic diameter smaller than 2.5 ($PM_{2.5}$) and 10 (PM_{10}) were used in this study. Most of the sampling was conducted using a high-volume air sampler (Thermo-Anderson, HVS) with a flow rate of ~1.13 m^3 min^{-1} at various sampling locations (Figure 2.3a). At Dibrugarh, the samples were collected using a low volume sampler (flow rate of ~1 L min^{-1}). Samples were collected on pre-combusted (at 300°C for 10 to 12 hours) tissue quartz filters (PALLFLEX®TM, 25×20 cm2). Soon after their collection, filters were wrapped in butter paper, sealed in plastic zip-lock bags and aluminium foil, and stored in the deep freezer (-19°C) until the time of analysis. The samplers were calibrated periodically for their flow rate, and a difference was found that was not higher than 10%. Routine maintenance and cleaning of the HVS were conducted to ensure the flow of air through the HVS. The PM mass concentrations were assessed gravimetrically from the mass of the filters before and after the particulate collection on an electronic balance (Saratorius, Model LA130S F) (Figure 2.3e). Before weighing, aerosol filters were equilibrated to ambient room 27 temperature (~23°C) under constant relative humidity (~35-40%). To ensure precision, we repeated weighing one sample after every five samples, and weights were found within 5%. The mass difference was divided by the volume of air filtered to get the ambient PM mass concentration.

2.2.2 Water soluble ionic species measurement

Water-soluble cations (Na^+, K^+, NH_4^+, Ca^{2+}, and Mg^{2+}) and anions (Cl^-, SO_4^{2-}, and NO_3^-) were measured aerosol samples using dual-channel Ion Chromatograph

(Dionex, ICS-5000, DC) coupled with an autosampler (DIONEX As-AP). To analyze the water-soluble inorganic species (WSIS, sum of cations and anions), ultrasonication of 6 cm^2 filter punches for 30 minutes (in three 10-minute cycles) in 30 ml of deionized water (Resistivity: 18.2 MΩ cm) was done. The resulting filtered water extract was then transferred to pre-cleaned 2 mL vials for analysis on the Ion Chromatograph. Before analysis, calibration of the instrument was done using laboratory-prepared and commercial standards. Cation and anion standards were created by dissolving various salts (e.g., NaCl, KNO_3, $(NH_4)_2SO_4$, Ca $(NO_3)_2$, $MgCl_2$) in deionized water. Additionally, commercial standards provided by Thermofisher Scientific were utilized for both anions (Dionex Combined Five Anion Standard, product no. 037157) and cations (Dionex Six Cation – II Standard, product no. 046070) to assess the quality of the laboratory-prepared standards. Charge balance ratio between total cations and total anions was also calculated to ensure it equalled close to one, thereby confirming the significant absence of any missing cation or anion.

2.2.3 $\delta^{15}N$ of NH_4^+

To determine the nitrogen isotopic composition ($\delta^{15}N$) of NH_4^+ an acid fumigation method was used. This approach is based on the method reported by Kawamura et al. (2004), and subsequently used by others (Kundu et al., 2010; Lim et al., 2020b). About 4-5 aliquots (each 1.5 cm^2) of the samples along with blank filters were exposed to the fumes of concentrated HCl (33%) overnight in a glass desiccator. Analysis of water-soluble inorganic nitrogen (WSIN, sum of NH_4^+-N and NO_3^--N), total nitrogen, and δ15N of total nitrogen (TN) for samples and blanks were performed before and after acid fumigation using IC and Isotope Ratio Mass Spectrometer (IRMS, Delta V Plus, Thermofisher Scientific, Germany) attached to an Elemental Analyser (EA, FLASH 2000), respectively. Here TN and TN after fumigation are referred as TN and TN_{pf}, respectively. Subsequently, a set of four conditions were defined to validate the usability of this method.

i) The first criterion required that NO_3^- concentrations in fumigated samples should match those in filter blanks to confirm quantitative removal of NO_3^-. After fumigation, the NO_3^- levels in samples and blanks were 0.006 ± 0.003 μmol/cm^2 and 0.005 ± 0.001 μmol/cm^2, respectively. Given that untreated samples had an average NO_3^-

concentration of 0.5 μmol/cm^2, more than 95% of the $NO_3^-$was removed, fulfilling the first condition.

ii) The 2nd criterion ensured that NH_4^+-N remained unchanged during fumigation. NH_4^+ concentrations before and after fumigation were highly correlated (R^2 = 0.99) with a slope close to one (Figure 2.1a), confirming that the process did not affect NH_4^+ levels.

iii) The 3rd criterion was that TN should be similar to WSIN in samples. This condition is important for the consideration of TN and δ^{15}N-TN_{pf} as NH_4^+-N and δ^{15}N-NH_4^+, respectively. A strong correlation between TN and WSIN was observed (Figure 2.1c), and TN_{pf} also correlated well with NH_4^+ concentrations (R^2 = 0.91) with a slope near unity (Figure 2.1b). This confirmed that post-fumigation TN consisted almost entirely of NH_4^+.

iv) The 4th criterion was that fumigation should had no effect on δ^{15}N-NH_4^+ or δ^{15}N-TN_{pf}. To verify that fumigation does not alter δ^{15}values of $NH4^+$, a control experiment was conducted using blank filters spiked with: (a) pure NO_3^- (KNO_3 solution), (b) a 1:1 mixture of NO_3^- and NH_4^+ (KNO_3 and $(NH_4)_2SO_4$ solution), and (c) Pure NH_4^+ ($(NH_4)_2SO_4$). The spiked filters were treated identically to the actual samples and analyzed for δ^{15}N using EA-IRMS. As shown in Table 2.2, δ^{15}N of fumigated (NO_3^- + NH_4^+ spiked) samples were similar to those of samples spiked with pure NH_4^+. This confirmed that fumigation had no significant effect on the δ^{15}N-NH_4^+.

Table 2.2. δ^{15}N of blank filters spiked with pure NO_3^-, (NO_3^- + NH_4^+), (NO_3^- + NH_4^+) fumigated and pure NH_4^+

Spiked samples	**δ^{15}N (‰)**
Pure NO_3^-	66 ± 0.09 (n=4)
1:1 mix of NO_3^- and NH_4^+	36.5 ± 0.5 (n=4)
Fumigated 1:1 mix of NO_3^- and NH_4^+	3.9 ± 0.7 (n=5)
Pure NH_4^+	3.6 ± 0.5 (n=5)

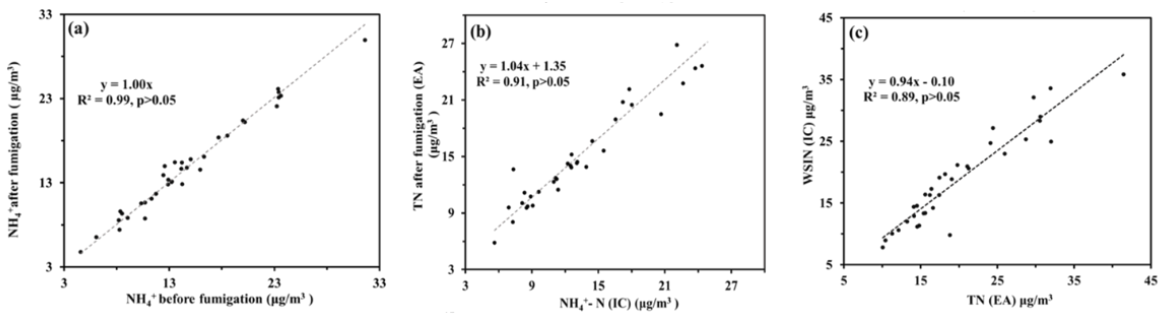

Figure 2.1. Conditions for the validation of acid fumigation method to remove NO_3^-. (a) Relationship between NH_4^+-N post- and pre-fumigation, (b) Relationship between TN left after fumigation and NH_4^+-N measured, and (c) Relationship between WSIN and TN. Here, WSIN was measured with IC and TN with EA (Shaw et al., 2024).

The successful fulfilment of all four validation conditions confirmed that NO_3^- was effectively removed from the samples without significantly altering the concentration or isotopic composition of NH_4^+. For nitrogen isotope analysis, filter aliquot areas were selected to ensure that the NH_4^+-N content exceeded 2 µmol of nitrogen. This threshold was maintained to achieve reliable analytical precision and to minimize the influence of blank filter contributions, which can become significant at low NH_4^+ concentrations. The NH_4^+-N levels over the selected filter areas were determined using ion chromatography on both untreated and fumigated filters. These aliquots were then tightly packed into tin capsules and analyzed using an elemental analyzer coupled with an isotope ratio mass spectrometer (EA-IRMS). The total nitrogen measured after fumigation (TN_{pf}), along with its $\delta^{15}N$ value ($\delta^{15}N$-TN_{pf}), was taken to represent the concentration and isotopic composition of NH_4^+ and $\delta^{15}N$-NH_4^+, respectively.

The stable isotopic ratios are reported in ‰ (per mil) relative to Air as follows:

$$\delta^{15}N(‰) = \left[\frac{\left(\frac{^{15}N}{^{14}N}\right)_{sample}}{\left(\frac{^{15}N}{^{14}N}\right)_{standard}} - 1\right] \times 1000 \qquad \text{eq. 2.1}$$

IAEA-N-2 ($(NH_4)_2SO_4$) was used as a standard for the isotopic measurements and analytical precision for repeat measurements of standards were better than 0.3 ‰.

2.2.4 $\delta^{15}N$ and $\delta^{18}O$ of NO_3^-

The dual isotope analysis of NO_3^- was performed at the Stable Isotope Laboratory of IISER Kolkata (SILIKA), using the Ti (III) chloride one-step reduction method to convert aqueous NO_3^- into N_2O gas in the vial headspace for $\delta^{15}N$ and $\delta^{18}O$

measurement, following the procedure described by Altabet et al. (2019). The standards used were USGS34, USGS35, and USGS32, with $\delta^{18}O$ values of -27.9‰, 57.5‰, and 25.4‰ (VSMOW), and $\delta^{15}N$ values of -1.8‰, 2.7‰, and 180‰ (AIR), respectively. In order to obtain an intermediate value for $\delta^{15}N$, USGS32 and IAEA-NO_3^- ($\delta^{15}N$ = 4.7‰) were mixed in the ratio of 1: 3 to obtain an in-house mix standard ($\delta^{15}N$ 48.7‰), which was used for the calibration (Altabet et al., 2019). Each standard of known weight was dissolved in deionised (MilliQ) water to achieve a final concentration of 5 ppm NO_3^-. For sample preparation, known filter areas were extracted in specific volumes of MilliQ water such that the final NO_3^- concentration in the extract was also 5 ppm. The volume of water used for each sample was adjusted based on its previously measured NO_3^-concentration via IC.

Before reduction, 30% Ti (III) chloride solution was pre-conditioned using zinc powder (1 g Zn per 10 ml $TiCl_3$) to eliminate any Ti (III) impurities. In a 20 ml glass vial, 50 µl of 10% HCl, 2.4 ml of deionised water, and 600 µl of either sample or standard were sequentially added. Then, pre-conditioned $TiCl_3$ was added at a reagent-to-sample ratio of 1:40. The vials were immediately sealed with crimp caps and gently swirled to ensure uniform mixing. The conversion reaction was allowed to proceed for 12–16 hours. Finally, the $\delta^{15}N$ and $\delta^{18}O$ values of the resulting N_2O in the vial headspace were measured using a Delta-V Isotope Ratio Mass Spectrometer (IRMS) operated in continuous flow mode with a Gas Bench II interface and a dual cryogenic trap.

The $\delta^{15}N$ and $\delta^{18}O$ defined by eq. (2.2) and (2.3), were reported relative to N_2 in air and Vienna Standard Mean Ocean Water (VSMOW), respectively.

$$\delta^{15}\mathrm{N}(‰) = \left[\frac{\left(\frac{^{15}\mathrm{N}}{^{14}\mathrm{N}}\right)_{\mathrm{sample}}}{\left(\frac{^{15}\mathrm{N}}{^{14}\mathrm{N}}\right)_{\mathrm{standard}}} - 1\right] \times 1000 \qquad \text{eq. 2.2}$$

$$\delta^{18}O(‰) = \left[\frac{\left(\frac{^{18}O}{^{16}O}\right)_{sample}}{\left(\frac{^{18}O}{^{16}O}\right)_{standard}} - 1\right] \times 1000 \qquad \text{eq. 2.3}$$

Calibration curves were constructed by plotting the known $\delta^{15}N$ and $\delta^{18}O$ values of standards against the IRMS output (Figure 2.2), which were then used to calculate the $\delta^{15}N$ and $\delta^{18}O$ values of NO_3^- in the samples. The standard deviations among repeated measurements were less than 1‰ for both $\delta^{15}N$ and $\delta^{18}O$. To assess any potential blank contribution, blank filters were extracted in the same manner as the

samples using deionised water, and subsequently treated with $TiCl_3$ following the same protocol as for the samples and standards. In addition, deionised water without filters was also subjected to identical treatment. The N_2O concentrations in both the deionised water and the filter-extracted blanks were consistently very low, with signal amplitudes close to the instrument's detection limit. It indicates that blank contributions were negligible and did not influence the isotopic measurements.

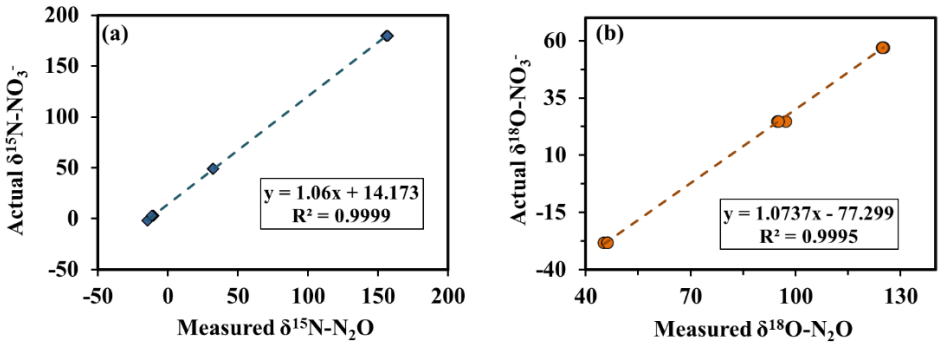

Figure 2.2. Measured vs Actual $\delta^{15}N$ (a) and $\delta^{18}O$ (b) in standards. $\delta^{15}N$ and $\delta^{18}O$ value of samples were calculated using the calibration equations in (a) and (b) respectively (Shaw et al., 2025).

2.3 Estimation and Modelling

2.3.1 Aerosol Thermodynamic Modelling using ISORROPIA-II

2.3.1.1 Model Configuration and Input Considerations

Determination of aerosol sensitivity regimes requires knowledge of aerosol pH and liquid water content (ALWC); to estimate ALWC and pH, the thermodynamic equilibrium model ISORROPIA II was used. This model simulates the phase state and chemical composition of an inorganic aerosol system comprising NH_4^+, SO_4^{2-}, NO_3^-, Cl^-, Na^+, Ca^{2+}, K^+, Mg^{2+}, and water, under equilibrium with their respective gas-phase precursors (Fountoukis & Nenes, 2007; Nenes & Pandis, 1998).

This modelling approach has been extensively used in global studies to predict ALWC and pH across varying atmospheric conditions (Guo et al., 2015, 2016; Nah et al., 2018; Shi et al., 2019). ISORROPIA-II was run in the forward (metastable) mode,

which assumes aerosols remain in a deliquesced state with no solid precipitates. In forward mode, the model predicts the gas-particle partitioning and ALWC based on total concentrations (gas + particle) of the relevant species. This mode is preferred because the reverse mode, which uses only the particle-phase inputs, is more sensitive to measurement uncertainties and often introduces significant biases in the predicted pH (Fang et al., 2024; S. Song et al., 2018). However, ISORROPIA-II results can become unreliable at low relative humidity (<40%) because the model assumes aerosols are always in a liquid (deliquesced) state, which is not valid under dry conditions. This leads to overestimation of ALWC and underestimation of acidity (i.e., higher pH). Additionally, the model does not account for solid-phase aerosols or kinetic limitations, which are common at low RH. These factors, along with high sensitivity to input uncertainties, can introduce significant biases in pH predictions (Guo et al., 2015; Weber et al., 2016). Similarly, data points corresponding to RH >95% were excluded from the analysis, since rapid increases in aerosol water at very high RH can introduce large uncertainties in pH estimation. Therefore, in this study, samples with RH <40% and >95% were excluded. Further, for these simulations, it was also assumed that particles were internally mixed, and that bulk pH represented the overall acidity of the aerosol population regardless of particle size. Previous study has shown that this assumption has minimal impact on predicted pH values, provided that sulphate is at least partially mixed with other aerosol components (Guo et al., 2017).

Input data for ISORROPIA-II included site-specific measurements of particle-phase species such as NH_4^+, SO_4^{2-}, NO_3^-, Cl^-, Mg^{2+}, Ca^{2+}, and Na^+, along with meteorological parameters (temperature and relative humidity), and gas-phase NH_3 from Central Pollution Control Board (CPCB). However, gas-phase HNO_3 concentrations were unavailable, which can introduce some uncertainty in model outputs.

To assess whether this missing input leads to major deviations, a cross-validation was performed at Delhi using high-resolution online gas and particle data. Model simulations using both complete online measurements and CPCB-ion chromatography combinations yielded comparable aerosol pH and ALWC values, indicating minimal sensitivity to the absence of gas-phase HNO_3. Furthermore, a sensitivity analysis was conducted over Ahmedabad during summer, wherein the nitrate partitioning factor (ε or fNO_3^-) varied between 0.2 and 1.0. This test also yielded similar model outputs, and is discussed in greater detail in the next chapter. Together, these

evaluations support the reliability of ISORROPIA-II outputs even under limited gas-phase data conditions. This agreement strengthens confidence in the overall consistency and robustness of ISORROPIA-II outputs across all sites, even under the forward-mode configuration.

2.3.1.2 Model Performance in the Present Study

To evaluate model performance, measured concentrations of NH_4^+ and NO_3^- were compared with those predicted by ISORROPIA-II. Statistical parameters like normalised mean bias (NMB) and regression coefficient were calculated and compared against standard thresholds to validate the reliability of the model outputs, as reported in literature (Liu et al., 2019). NMB was calculated using eq. 2.4.

$$NMB = \sum \frac{P_i - O_i}{\sum O_i} \times 100 \qquad \text{eq. 2.4}$$

Where, Pi and Oi represent the modelled and actual concentration of NH_4^+ (or NO_3^-), respectively. Calculated NMB for NH_4^+ and NO_3^- for the study sites are given in Figure 2.3 and 2.4. Across all locations and seasons, R^2 values ranged between 0.87 and 0.95 for NH_4^+, and between 0.91 and 0.98 for NO_3^-, indicating strong agreement. NMB values for NH_4^+ remained between 16% and 25%, while for NO_3^-, they ranged from 1% to 17%. Furthermore, a strong positive correlation (Figure 2.3 and 2.4) between actual and modelled concentration for both NH_4^+ and NO_3^- with regression coefficients far above the threshold further strengthen the reliability of the model outputs. These results demonstrate that the model reproduces both the trend and magnitude of observed particulate NH_4^+ and NO_3^- concentrations. The relatively low bias and high R^2 observed across the study sites confirm the reliability of the forward-mode simulations, even under conditions with limited gas-phase data.

2.3.1.3 Comparison with Existing Model Evaluation Studies

Existing studies have commonly evaluated ISORROPIA-II model performance using regression-based comparisons between measured and predicted concentrations of aerosol species. For instance, Guo et al. (2017) reported good agreement between modelled and observed NH_4^+ and NO_3^- during the CalNex campaign over Pasadena, with R^2 values ranging ~0.98–0.99. Guo et al. (2016) also

assessed model performance across the northeastern United States, reporting R^2 values between ~ 0.71 to ~ 0.97 and normalized mean biases ranging from approximately −15% to −2%, depending on relative humidity conditions. Similarly, Nah et al. (2018), in a southeastern U.S. setting, found an R^2 ~ 0.9 for NH_4^+ and ~ 0.65 for NO_3^-, indicating variable model performance across different species and conditions. Recommendations from model evaluation frameworks such as Emery et al. (2017) suggested that correlation coefficients (R^2) above 0.7 and normalized biases within ± 30% are acceptable for secondary aerosol simulations. The present study meets these criteria, supporting the applicability and robustness of ISORROPIA-II under the conditions examined.

2.3.1.4 Sources of Bias in Model Assumptions

Several factors may contribute to the minor discrepancies between measured and modelled values. ISORROPIA-II assumes that aerosol particles are internally mixed and reach thermodynamic equilibrium, which may not always hold in real ambient conditions where external mixing and kinetic limitations exist. Furthermore, the model does not account for organic acids, which may influence aerosol acidity and affect the ion balance, particularly in environments impacted by biogenic or combustion sources. Additionally, the absence of gas-phase HNO_3 input may lead to slight underestimations in total nitrate under specific conditions. Overall, the consistency of our bias and R^2 values with existing benchmarks, combined with known model limitations, supports the acceptability of the ISORROPIA-II outputs used in this work. Since the initial model run did not include gas-phase concentrations, this could result in potential biasing in the pH and f estimates. To assess whether there was any significant biasing, a second ISORROPIA II run was performed using both the calculated gas-phase (NH_3 and HNO_3) and measured particulate concentrations from IC again in forward metastable mode. The modelled NH_4^+ and NO_3^- concentration was then compared against the measured concentrations to evaluate the accuracy and acceptability of the estimates.

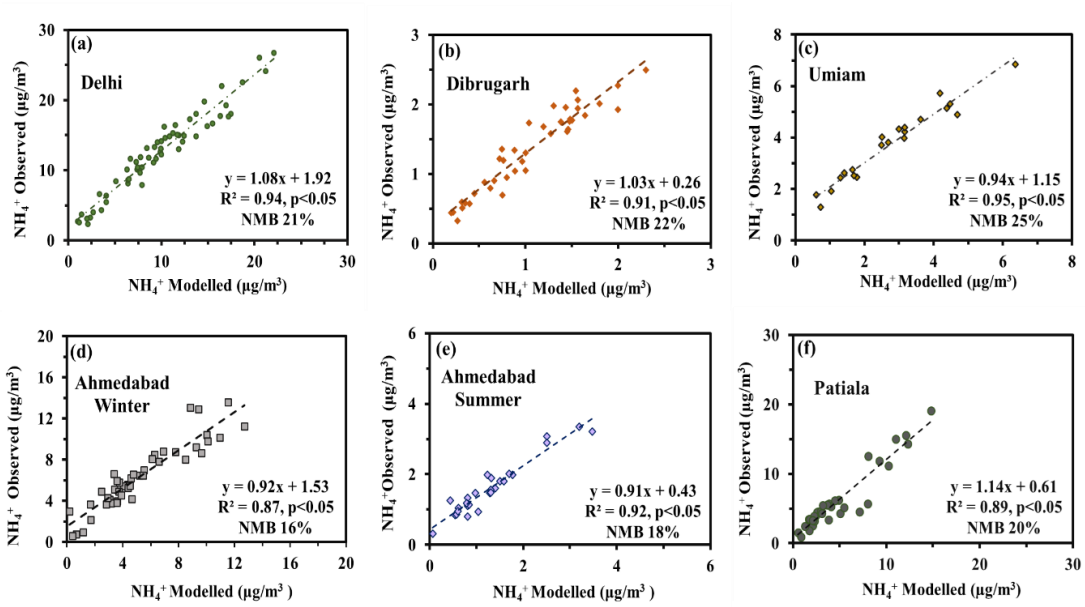

Figure 2.3. Observed (analysed by IC) vs modelled (ISSOROPIA II) NH_4^+ concentration over the sampling sites.

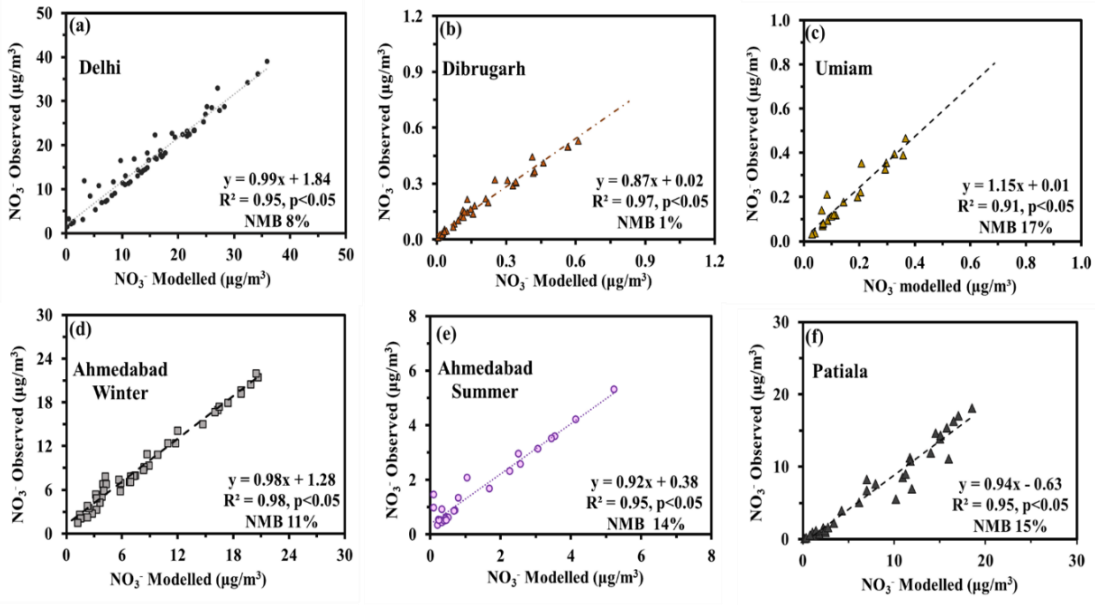

Figure 2.4. Observed (analysed by IC) vs modelled (ISSOROPIA II) NO_3^- concentration over the sampling sites.

2.3.2 Estimation of pH, Critical pH and Sensitivity Regimes

2.3.2.1 Aerosol pH

Aerosol pH is the acidity of the liquid water associated with the aerosol particulates, and is typically defined as the negative logarithm of hydronium ion (H_3O^+) activity on a molality basis. This can be expressed as:

$$pH = -log_{10}[a(H^+)] \quad \text{eq. 2.5}$$

$$\text{Or, pH} = -\log_{10}\left[\mathrm{m}(\mathrm{H}^+) \times \gamma_{\mathrm{m}}(\mathrm{H}^+)/\mathrm{m}^{\theta}\right] \quad \text{eq. 2.6}$$

$a(H^+)$ is the activity of hydronium ions in the aqueous phase, $m(H^+)$ is the molality of H_3O^+, $\gamma_m(H^+)$ is its activity coefficient, and m^θ is the reference molality (1 mol/kg). In practice, due to the limited availability of direct liquid-phase measurements in the atmosphere, thermodynamic model such as ISORROPIA II estimates aerosol composition in terms of concentrations per unit volume of air. To calculate aerosol pH from model outputs, the following approximation is commonly used:

$$pH = -log_{10}\frac{1000 \times \gamma_{H^+} \times H^+_{air}}{W_i} \quad \text{eq. 2.7}$$

Here, W_i is the ALWC from inorganic species in μg/m^3, γH^+ is the hydronium activity coefficient (assumed to be 1), 1000 is the conversion factor from grams per litre to micrograms per cubic meter and H^+ is the hydronium ion concentration per volume of air (μg/m^3). W_i and H^+_{air} are directly obtained from ISORROPIA II model output.

2.3.2.2 Critical pH

The mathematical expression for Critical pH for NH_3 and HNO_3 is denoted as pH″ and pH′, respectively, and expressed by eq. 2.8 and 2.9.

$$pH'' = log\left[\left(\frac{1-\beta}{\beta}\right)\right] \times \Phi \times W_i \quad \text{eq. 2.8}$$

$$pH' = -log\left[\left(\frac{1-\alpha}{\alpha}\right)\right] \times \Psi \times W_i \quad \text{eq. 2.9}$$

In the above equations, β and α are the threshold partitioning factors (ε) for NH_3 and HNO_3, respectively. They represent the level at which the PM concentrations are influenced by availability or emission of NH_3^T and HNO_3^T. NH_3^T refers to the sum of gaseous NH_3 and particulate NH_4^+, whereas HNO_3^T is the sum of HNO_3 gas and NO_3^- particulate. Here, β and α were considered to be 0.1, which means PM level responded to change in NH_3-NH_4^+ and HNO_3-NO_3^- when at least 10% of precursor have partitioned into particulate phase (Nenes et al., 2020). The W_i refers to ALWC in $\mu g/m^3$ and the term Φ and Ψ are parameters that depend on activity coefficient, Henry's law constant and dissociation constants of NH_3 and HNO_3 respectively. The Φ and Ψ can be expressed by the following equations:

$$\Phi = \frac{\gamma_{H+} \times H_{NH3} \times R \times T}{\gamma_{NH4+} \times K_a} \qquad \text{eq. 2.10}$$

$$\Psi = \frac{R \times T \times K_{n1} \times H_{HNO3}}{\gamma_{NO3-} \times \gamma_{H+}} \qquad \text{eq. 2.11}$$

In eqs. 2.10 and 2.11, H_{NH3} and H_{HNO3} represent the Henry's law constants for NH_3 and HNO_3, respectively, whereas, K_a and K_{n1} are their corresponding dissociation constants. The products of Henry's law constants and dissociation constants were estimated using formulations provided by Clegg et al. (1998) and Clegg & Brimblecombe (1990). Wi is the ALWC; R is the universal gas constant; T is the ambient temperature (K) and γ is the activity coefficient of species. The parameters β and α are ε thresholds, at which the PM concentrations is influenced by availability or emission of NH_3^T and HNO_3^T respectively, and can be calculated by the eqs. 2.12 and 2. 13 respectively. Based on the calculated critical pH values and where the existing pH lies relative to pH′ and pH″, sensitivity regimes were determined, the details on this is discussed in the subsequent chapter.

Furthermore, the relationship between aerosol pH and the partitioning factor (ε) under a given ALWC (W_i) follows a sigmoidal (S-shaped) curve. This reflects the non-linear response of NH_4^+ and NO_3^- formation to changes in pH, indicating threshold behaviour where changes in pH lead to significant shifts in gas-particle partitioning. Consequently, this reflects the response of PM load to change in NH_3^T and HNO_3^T, as a function of aerosol pH under specific liquid water conditions (Guo et al., 2015, 2016, 2017, 2018; Nenes et al., 2020). The analytical ε was calculated using the following equations:

$$\varepsilon(NH_4^+) = \frac{\frac{\gamma_{H+}}{\gamma_{NH4+}} \times [H^+] \times W_i \times R \times T \times \frac{H_{NH3}}{K_a}}{1 + \frac{\gamma_{H+}}{\gamma_{NH4+}} \times [H^+] \times W_i \times R \times T \times \frac{H_{NH3}}{K_a}} \quad \text{eq. 2.12}$$

$$\varepsilon(NO_3^-) = \frac{W_i \times R \times T \times K_{n1} \times H_{HNO3}}{\gamma_{H+} \times \gamma_{NO3-} \times [H^+] + (W_i \times R \times T \times K_{n1} \times H_{HNO3})} \quad \text{eq. 2.13}$$

Details on these parameters and the derivation of the equations can be found in (Guo et al., 2017; Nenes et al., 2020).

2.3.3 Calculation of δ^{15}N-NH_3 gas from δ^{15}N-NH_4^+

The estimation of $\delta^{15}N$ for atmospheric NH_3 gas was carried out using an isotopic mass-balance model based on a well-mixed closed system. This approach has been widely used in earlier studies (Pan et al., 2016, 2018; Wu et al., 2020; Wu et al., 2019; Zhang et al., 2019; Zhang et al., 2020). NH_3(g) forms NH_4^+ via equilibrium reversible reactions which involves isotopic fractionation (R4) (Kirshenbaum et al., 1947; Savard et al., 2017; Thode & Urey, 1939; Urey et al., 1937; Walters et al., 2019). Further, NH_3(g) also reacts with acidic species like H_2SO_4, HNO_3, and HCl, via R2-R4 to form stable $(NH_4)_2SO_4$ or/and semi-volatile NH_4NO_3 and NH_4Cl (Walters et al., 2019).

$$2NH_{3(g)} + H_2SO_{4(g)} \rightarrow (NH_4)_2SO_{4\,(s)} \text{ or } 2NH_4^+{}_{(aq)} + SO_4^{2-}{}_{(aq)} \quad \text{(R1)}$$

$$NH_{3(g)} + HNO_{3(g)} \leftrightarrow NH_4NO_{3\,(s)} \text{ or } NH_4^+{}_{(aq)} + NO_3^-{}_{(aq)} \quad \text{(R2)}$$

$$NH_{3(g)} + HCl_{(g)} \leftrightarrow NH_4Cl_{\,(s)} \text{ (or } NH_4^+{}_{(aq)} + Cl^-{}_{(aq)}) \quad \text{(R3)}$$

$$^{14}NH_4^+{}_{(aq)} + {}^{15}NH_{3(g)} \leftrightarrow {}^{15}NH_4^+{}_{(aq\,)} + {}^{14}NH_{3(g)} \quad \text{(R4)}$$

Under such conditions the isotopic relationship between the initial NH_3(g) (δ^{15}N-NH_3) and NH_4^+ formed (δ^{15}N-NH_4^+) is given by the following expression (Heaton, 1987; Pan et al., 2016).

$$\delta^{15}NH_{4^+} = \delta^{15}NH_3 + \varepsilon_{NH_4^+/NH_3} \times (1 - f) \quad \text{eq. 2.14}$$

In eq. 2.14, f refers to the fraction of the initial NH_3(g) converted to NH_4^+(p), (i.e., f = NH_4^+/ (NH_4^++ NH_3)). The isotope enrichment factor ($\varepsilon_{NH4+/NH3}$) is the degree of isotope enrichment during the conversion of NH_3(g) to NH_4^+(p). It depends on the air temperature following relationship between ε and temperature (T in K) given by Urey (1947):

$$\varepsilon_{NH_4+/NH_3} = 12.4678 \times \frac{1000}{T} - 7.6694 \quad \text{eq. 2.15}$$

2.3.4 Estimation of NO_3- Formation Pathways and $\delta^{15}N$-NO_x

Estimation of the formation pathways of NO_3^- from its precursor requires knowledge of the $\delta^{18}O$ value of NO_3^- formed via each pathway (P_1 to P_4). The $\delta^{18}O$-NO_3^- values formed via P_1 to P_4 were calculated following equations given by Walters & Michalski (2016, 2015) and Michalski et al. (2014).

2.3.4.1 Calculation of $\delta^{18}O$-NO_3^- for P_1 to P_4

The $\delta^{18}O$-NO_3^- formed via P_1 to P_4 were calculated as follow:

$$\delta^{18}O - NO_2\ (‰) = 1000 \times \left[\frac{\left(\frac{18\alpha\, NO_2}{NO} - 1\right) \times (1 - fNO_2)}{(1 - fNO_2) + \left(\frac{18\alpha\, NO_2}{NO} \times fNO_2\right)}\right] + \delta^{18}O - NO_x \quad \text{eq. 2.16}$$

$\delta^{18}O\text{-}NO_{3\ (P1)} = 2/3\ \delta^{18}O\text{-}NO_2 + 1/3\ \delta^{18}O\text{-}OH$ eq. 2.17

where, $\delta^{18}O\text{-}OH = \delta^{18}O\text{-}H_2O + 1000(^{18}\alpha_{X/Y} - 1)$ eq. 2.18

$\delta^{18}O\text{-}NO_{3\ (P2a)} = 5/6\ \delta^{18}O\text{-}N_2O_5 + 1/6\ \delta^{18}O\text{-}H_2O$ eq. 2.19

or, $5/6(\delta^{18}O\text{-}NO_2 + 1000\ (^{18}\alpha_{X/Y} - 1)) + 1/6\ \delta^{18}O\text{-}H_2O$ eq. 2.20

$\delta^{18}O\text{-}NO_{3\ (P2b)} = \delta^{18}O\text{-}N_2O_5$ eq. 2.21

$\delta^{18}O\text{-}NO_{3\ (P3)} = \delta^{18}O\text{-}NO_2 + 1000(^{18}\alpha_{X/Y} - 1)$ eq. 2.22

$\delta^{18}O\text{-}HNO_{3\ (P4)} = \delta^{18}O\text{-}ClONO_2$ eq. 2.23

or, $\delta^{18}O\text{-}NO_2 + 1000\ (^{18}\alpha_{X/Y} - 1)$ eq. 2.24

The $\delta^{18}O$-NO_2 (‰) was calculated using eq. (2.16), where f_{NO2} is the fraction of NO_2 to N, $\delta^{18}O$-NO_x values between 62‰ and 117‰ were assumed for the calculation (Michalski et al., 2014; Z. Zhang et al., 2021; Zhu et al., 2021), Here, $^{18}\alpha_{X/Y}$ is the isotopic fractionation factor in all the equations, and is calculated based on eq. (2.25) given by Walters & Michalski (2016).

$$1000\ (^{18}\alpha_{X/Y} - 1) = \frac{A}{T^4} \times 10^{10} + \frac{B}{T^3} \times 10^8 + \frac{C}{T^2} \times 10^6 + \frac{D}{T} \times 10^4 \quad \text{eq. 2.25}$$

Here, X and Y are different species between whom fractionation factor was calculated; H_2O, OH and N_2O_5, NO_2 in case of eq. (2.18) and eq. (2.20) respectively. X and Y in case of eq. (2.22) and eq. (2.24) are NO_2, NO_3 and $ClONO_2$, NO_2 respectively. T is the ambient temperature, A, B, C and D are constants depending upon the species (Walters & Michalski, 2016). The $\delta^{18}O$-H_2O was considered around -11 ± 4 ‰ (Deshpande et al., 2010).

2.3.4.2 Estimation of formation pathway contributions

$\delta^{18}O$-NO_3^- values associated with all the pathways were estimated using the eq. (2.17) to (2.24). Isotopic mass balance eq. (2.26) was used to calculate the overall fractional contributions (f_{P1}, f_{P2a}, f_{P2b}, f_{P3} and f_{P4}) of different pathways. P_2 represented the combined contribution involving heterogenous reaction and N_2O_5 hydrolysis, via H_2O (P_{2a}) and Cl^-(P_{2b}). Similar mass balance equation, considering multiple reaction pathways was used to estimate the pathway contributions by several previous studies (Chang et al., 2018; H. W. Xiao, Wu, et al., 2020; Zhu et al., 2021).

$$\delta^{18}O - NO_{3\ Samples}^- = \sum_{i=1}^{4} \left(\delta^{18}O - NO_{3\ P_i}^- \times f_{P_i}\right) \qquad \text{eq. 2.26}$$

The value of $\delta^{18}O$-NO_3^- $_{samples}$ represented the average $\delta^{18}O$ value of NO_3^- measured using IRMS, while the $\delta^{18}O$-NO_3^- values for pathways P_1 to P_4 were calculated using the respective equations described earlier. To estimate the fractional contribution (f) of each pathway, Monte Carlo simulations were performed in R. Standard deviations for both measured and calculated $\delta^{18}O$-NO_3^- were incorporated while estimating f. The errors associated with the feasible solutions that satisfied eq. (2.26) varied from 0.04 to 0.1%. Previous study by Chang et al. 2018 used similar method, considering solutions with an error of less than 0.5% between the calculated and measured $\delta^{18}O$-NO_3^-. In this study, all feasible solutions had errors below 0.5%, and no statistically significant differences ($p > 0.05$, t-test) were found among the f values of these solutions. Therefore, the solution with the lowest error was chosen for interpretation.

2.3.4.3 Estimation of $\delta^{15}N\text{-}NO_x$ and source contributions

$\delta^{15}N\text{-}NO_x$ was calculated using eq. (2.27) where Δ is the isotopic fractionation effect associated with each pathway, and $\delta^{15}N\text{-}NO_3^-$ represents the measured values of samples from IRMS.

$$\delta^{15}N\text{-}NO_x = \delta^{15}N\text{-}NO_3^- \text{(measured)} - \Delta \quad \text{eq. 2.27}$$

In both the locations (Patiala and Ahmedabad) 2 major pathways (P_1 and P_{2a}) were considered for source apportionment of NO_x, the reason for this is given in Chapter 5. Therefore, the Δ value in eq. (2.27) was calculated as follow:

$$\Delta = f_{OH} \times \varepsilon_{OH} + f_{N2O5} \times \varepsilon_{N2O5} \quad \text{eq. 2.28}$$

Here, f_{OH} and f_{N2O5} are the fractional contribution from P_1 and P_2 while ε_{OH} and ε_{N2O5} are the fractionation factor associated with P_1 and P_2, respectively. Further, ε_{OH} and ε_{N2O5} were calculated using the mass-balance eq. (2.29) and (2.30) given by Walters & Michalski, (2016).

$$\varepsilon_{OH} = 1000 \times \left[\frac{(^{15}\alpha_{NO2/NO} - 1)(1 - fNO_2)}{(1 - fNO_2) + (^{15}\alpha_{NO2/NO} \cdot fNO_2)}\right] \quad \text{eq. 2.29}$$

$$\varepsilon_{N2O5} = 1000 \times (^{15}\alpha_{N2O5/NO2} - 1) \quad \text{eq. 2.30}$$

α was calculated by eq. (2.15); values of A, B, C and D were taken from Walters & Michalski (2016). The f_{OH} and f_{N2O5} values were estimated using eqs. (2.19) and (2.20), where $f_{OH} + f_{N2O5} = 1$ and $[\delta^{18}O\text{-}NO_3^-]_{OH}$ and $[\delta^{18}O\text{-}NO_3^-]_{N2O5}$ were calculated by eqs. (2.17) and (2.19) respectively.

2.3.5 Source Apportionment of NH_3 and NO_x using MixSIAR

The contributions of various emission sources to NH_3 and NO_x were estimated using the Bayesian mixing model MixSIAR (B. C. Stock et al., 2018; B. Stock & Semmens, 2017). This model applies Bayesian inference to determine the most probable source contributions to a mixture based on tracer compositions, such as stable isotope ratios, assuming conservative mixing with minimal alteration during atmospheric transport. This approach has been used extensively for source apportionment of NH_3 and NO_x in atmosphere by several existing studies (Bhattarai et

al., 2021; Chen et al., 2022; Dong et al., 2022; Y. Li et al., 2023; Shaw et al., 2024, 2025; W. Song et al., 2019; L. Wu et al., 2021; H. Xiao et al., 2024; Xin et al., 2023).

For NH_3, four major sources were considered, this included agricultural wastes (livestock breeding, fertilizer application and urban wastes), biomass burning (BB), coal fired power plant (CFPP) and traffic exhaust with $\delta^{15}N\text{-}NH_3$ values of -25.1 ± 6‰, -12.3 ± 7 ‰, -0.2±7 ‰ and -1.5 ± 5 ‰ respectively (Li et al., 2023). These values are consistent with those reported in other recent studies (Walters et al., 2020; Wu et al., 2021; Xiao et al., 2024). Since, $\delta^{15}N\text{-}NH_3$ for agricultural emission (-24.8 ± 5%), livestock (-26.8± 5%) and urban wastes (-23.6 ± 7.2%) are very similar and/or overlapping (Y. Li et al., 2023; Xiao et al., 2024), their contributions were considered together, and named as agriculture and urban wastes emission. Source apportionment of NO_x was done similarly, using $\delta^{15}N\text{-}NO_x$ as the isotopic tracer. The four main sources included coal-fired power plants (CFPPs), biomass burning, vehicular emissions, and a grouped category representing soil-related emissions, which encompassed contributions from fertilized soils, urban waste, and livestock waste. This grouping was done due to the overlapping $\delta^{15}N$ signatures among these sub-sources, making them indistinguishable within the model framework. The corresponding $\delta^{15}N\text{-}NO_x$ values used in the model were 14.2 ± 4.4‰ for CFPPs, 1.0 ± 4.1‰ for biomass burning, -12.6 ± 3.9‰ for traffic, and -35.4 ± 12.6‰ for soil+ emissions (Felix et al., 2012; Felix & Elliott, 2014; Fibiger & Hastings, 2016; Walters., 2015; Zhu et al., 2021). These isotopic endmembers, along with the observed $\delta^{15}N\text{-}NO_x$ values from field samples, were input into the MixSIAR framework.

In both cases, when only a single isotope is used, the model relies on the basic linear mixing equation:

$$Y = \sum p_k \mu_k \qquad \text{eq. 2.31}$$

where Y is the stable isotope value of mixture, which has k possible sources; μ_k is the mean stable isotope value for source k (after considering the isotope fractionation), and p_k is the proportional contribution of source (Stock et al., 2018; Wu et al., 2021). The Gelman diagnostic was applied to assess model convergence, confirming that the posterior distributions were stable and well-resolved. Overall, this approach provided a quantitative and uncertainty-aware assessment of the contributions from major NH_3 and NO_x emission sources in the atmosphere.

2.4 Auxiliary Data

2.4.1 Meteorological parameters

Meteorological parameters including temperature (T), relative humidity (RH), boundary layer height (BLH), wind speed, and precipitation were obtained from the ERA5 reanalysis dataset provided by the European Centre for Medium-Range Weather Forecasts (ECMWF) (Hersbach et al., 2020). ERA5 offers hourly global data at a spatial resolution of 0.25° × 0.25° (~25 km), making it highly suitable for regional atmospheric studies. For each sampling location, hourly meteorological data were extracted and subsequently averaged over the respective sample collection periods to ensure temporal alignment with field observations. ERA5 generates precipitation and other meteorological fields by assimilating observations from ground stations, satellites, and other sources into advanced numerical weather prediction models, resulting in consistent and high-resolution gridded datasets widely used in atmospheric and climate research.

2.4.2 Gas Concentration

Gaseous concentration data for ammonia (NH_3), nitrogen oxide (NO), and nitrogen dioxide (NO_2) were obtained from the Central Pollution Control Board (CPCB), which operates a network of air quality monitoring stations across India. These measurements are available at an hourly resolution and were averaged over the specific sampling durations to match the time-integrated filter-based measurements used in this study. CPCB data have been widely used in previous studies investigating reactive nitrogen species and air quality trends in India (Sahu et al., 2021; Sharma et al., 2020). The NH_3 data from CPCB were further validated using thermodynamic modelling with ISORROPIA-II, as described in the previous section, to assess the consistency of the gas-phase NH_3 concentrations with measured particulate NH_4^+ and aerosol equilibrium conditions.

Chapter 3
Factors affecting gas-particle partitioning in NH_x

3.1 Understanding the NH_x System and Its Atmospheric Significance

NH_3 gas and its particulate counterpart NH_4^+(collectively termed NHx) plays important role tropospheric chemistry, air quality, and nitrogen deposition (Pan et al., 2016, 2018; Walters et al., 2019). In the atmosphere, NH_4^+ is formed via reversible gas-particle phase reaction from its precursor NH_3(g). Further, NH_4^+ can react with acidic species and form compounds like $(NH_4)_2SO_4$, NH_4NO_3 and NH_4Cl. It may also react with volatile organic compounds (VOCs) to form nitrogenous organics but, it is much less abundant than inorganic counterparts. While $(NH_4)_2SO_4$ is a stable compound, both NH_4NO_3 and NH_4Cl are volatile and are prone to volatilization under high temperature, further these compounds contribute significantly to fine particulate matter, influencing visibility, cloud condensation nuclei (CCN) properties, and human health. (Walters et al., 2019). The conversion of NH_3 (g) to NH_4^+ is associated with equilibrium isotopic fractionation, in which the particulate phase gets isotopically enriched. This gas-particle partitioning of NH_3 (g) - NH_4^+ is governed by multiple factors like meteorology which includes temperature and relative humidity along with atmospheric chemistry which includes existing pH condition and aerosol liquid water content, with complex interplay between them. Understanding the gas-particle partitioning is crucial to accurately predict the fate, transport, and environmental impacts of NHx.

NH_3(g) is highly water soluble with a high Henry' law constant (62 M/ atm at 298 K, Walter et al., 2019), and conversion of NH_3(g) to NH_4^+ is governed by the equilibrium reversible reaction (R1). Formation of $(NH_4)_2SO_4$ from NH_4^+ is preferred first, being stable and non-volatile (R2 and R3). The remaining NH_4^+ after the formation of $(NH_4)_2SO_4$ can reacts with other anions like NO_3^- and Cl^- to form volatile compounds

like NH_4NO_3 and NH_4Cl respectively (R4 and R5) (Behera et al., 2013; Renard et al., 2004; Scott & Cattell, 1978).

$NH_3\ (g) + H_2O\ (aq) \leftrightharpoons NH_4^+\ (aq) + OH^-$ R1

$2NH_4^+\ (aq) + SO_4^{2-} \rightarrow (NH_4)_2SO_4\ (aq) + H^+$ R2

or $NH_3(g) + H_2SO_4\ (g) \rightarrow (NH_4)_2SO_4(s)$ or $(2NH_4^+\ SO_4^{2-})\ (aq)$ R3

$NH_4^+ + NO_3^- \leftrightharpoons NH_4NO_3\ (aq)$ R4

$NH_4^+ + Cl^- \leftrightharpoons NH_4Cl\ (aq)$ R5

3.2 Environmental Factors Regulating NH_x Partitioning

The partitioning between NH_3 and NH_4^+ is strongly influenced by several meteorological and chemical parameters. Chief among them is temperature, RH, aerosol acidity or pH, and ALWC. These parameters affect both the extent of NH_3 conversion to NH_4^+ and the isotopic signature of the particulate phase.

3.2.1 Effect of Meteorology

NH_3 being a highly water-soluble gas gets readily dissolved in aqueous phase. Under higher RH and lower temperature, the reaction in R1 is favoured towards right, promoting the conversion of $NH_3(g)$ to NH_4^+. This promotes isotopic enrichment of the particulate phase, as heavier nitrogen isotopes preferentially accumulate in NH_4^+ during equilibrium partitioning.

Higher temperature, lower RH shifts the equilibrium towards left, since Henry's Law constant (H) for $NH_3(g)$ decreases with increasing temperature (Walters et al., 2019). This effects of temperature and RH can however, differ depending on the type of compound that NH_4^+ forms in the atmosphere**.**

3.2.2 Aerosol pH and ALWC

Aerosol pH and ALWC together govern whether the equilibrium partitioning of $NH_3(g)$ and $HNO_3(g)$ to particulate NH_4^+ and NO_3^- influence the PM mass concentrations. While pH and ALWC influence the partitioning of these gases into their

particulate counterparts, this partitioning in turn affects the aerosol pH, creating a two-way interaction between chemical composition and aerosol thermodynamics (Guo et al., 2017; Nah et al., 2018; Nenes et al., 2020, 2021). This coupled relationship was formalized in a mathematical framework by Nenes et al. (2020), which describes how the gas-particle partitioning of NH_3-NH_4^+ and HNO_3-NO_3^- responds to changes in pH and ALWC, and thus affecting PM mass concentration. Since both $NH_3(g)$ and $HNO_3(g)$ are key precursors that can significantly affect aerosol pH, the framework includes both species to evaluate their role in determining PM mass concentration. As this chapter focuses specifically on the NHx system, the following section will detail the influence of pH and ALWC on NH_3-NH_4^+ and ultimately PM load. Although the emphasis is on NHx, it is important to note that similar formulations for HNO_3-NO_3^- system are also provided in the study by Nenes et al. (2020)

The response of aerosol mass change to the changes in NH_3 (g) - NH_4^+ partitioning can be expressed by the following equations (Guo et al., 2017; Nenes et al., 2020).

$$\frac{\partial \mathrm{PM}}{\partial \mathrm{NH}_3^T} = \lambda \times \frac{\partial NH_4^+}{\partial \mathrm{NH}_3^T} \qquad \text{eq. 3.1}$$

$$\text{Here,} \quad \lambda \times \frac{\partial NH_4^+}{\partial \mathrm{NH}_3^T} = \lambda \times \varepsilon(NH_4^+) \qquad \text{eq. 3.2}$$

$NH_3{}^T$ is the total ammonia (NH_3 (g) + NH_4^+) whereas the term ∂PM and $\partial NH_3{}^T$ represent the change in aerosol mass concentration and total ammonia respectively. The $\varepsilon(NH_4^+)$ is equilibrium partitioning factor which denotes fraction $NH_3{}^T$ which has partitioned to particulate phase (NH_4^+) and $\boldsymbol{\lambda}$ denotes the amount of particulate mass gained or lost for each mole of NH_4^+ formed or lost. The $\varepsilon(NH_4^+)$ can be described by eq.3.3

$$NH_4^+ = \varepsilon(NH_4^+) \times \mathrm{NH}_3^T \qquad \text{eq. 3.3}$$

Further, in order understand how aerosol pH and ALWC affect ability of equilibrium partitioning factor $\varepsilon(NH_4^+)$ to influence the aerosol mass concentration, the concept of Critical pH and "Sensitivity regime" was proposed by Nenes et al. 2020. Critical pH is the threshold acidity level that determines whether the gas-to-particle partitioning of compounds like NH_3 and HNO_3 significantly influences the aerosol mass concentration. The mathematical expression for Critical pH for NH_3 and HNO_3 denoted as pH″ and pH′ respectively can be expressed by eq. 3.4 and 3.5.

$$pH'' = \log\left[\left(\frac{1-\beta}{\beta}\right)\right] \times \Phi \times W_i \qquad \text{eq. 3.4}$$

$$pH' = -\log\left[\left(\frac{1-\alpha}{\alpha}\right)\right] \times \Psi \times W_i \qquad \text{eq. 3.5}$$

Here β and α are the threshold partitioning factors for NH_3 and HNO_3 respectively that defines the levels at which PM load is responsive to change in NH_3^T and HNO_3^T availability or emission. W_i is the aerosol liquid water content and the term Φ and Ψ are parameters that depend on activity coefficient, Henry's law constant and dissociation constants of NH_3 and HNO_3 respectively. Details on these parameters are in Chapter 2 and the derivation of the equations can be found in (H. Guo et al., 2017; Nenes et al., 2020).

Based on the critical pH values and where the existing pH lies relative to pH′ and pH″, the aerosol system is divided into four regimes. If the pH>pH″ and pH< pH′, then the system is buffered and is insensitive to change in NH_3 and HNO_3, when pH< pH″ and pH< pH′, change in PM load is dependent mainly on NH_3^T emission or availability, thus the regime is "NH_3 Sensitive", whereas when pH>pH″ and pH>pH′, the system is "HNO_3 Sensitive". The change in PM mass depends on both of NH_3^T and HNO_3^T availability or emissions when the pH<pH″ and pH>pH′, These zones aid in understanding which precursor is more important under specific atmospheric conditions over a geographical location.

The critical pH values are not constant; they change depending on the aerosol liquid water content (ALWC) and temperature. The effects of ALWC and temperature on pH′ and pH″ are illustrated in Figure 3.1.

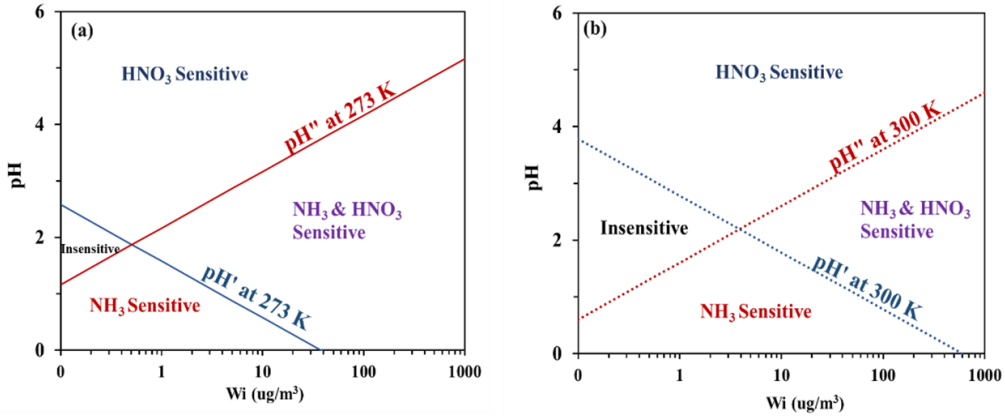

Figure 3.1. pH′ and pH″ at (a) 273K (b) 300K

In Figure 3.1 the slopes of Wi vs pH′ and pH″ decreases and increases with increase in ALWC, respectively. $NH_3(g)$ partitions to NH_4^+ via equilibrium reaction (R1). When ALWC increases, the formed NH_4^+ becomes diluted, so to have similar impact on PM load, more $NH_3(g)$ needed to be partitioned, to cross the threshold value. Although the equilibrium reaction (R1) is thermodynamically favoured at lower pH, the increase in ALWC lowers the effective H^+ concentration, and this dilution leads to a higher pH for the increase in ALWC, therefore the system becomes NH_3 Sensitive at a higher pH. On the other hand, HNO_3 is a strong acid that dissolves and dissociates completely into H^+ and NO_3^- in the presence of water, thus its partition depends primarily on its solubility. Therefore, increase in ALWC enhances the dissolution of HNO_3 into the particulate phase. This means that at a higher ALWC, HNO_3 can still partition effectively even under relatively lower pH.

Temperature also influences how easily NH_3 and HNO_3 partition into the particle phase. The effects of temperature on critical pH are illustrated Figure 3.1, where pH′ and pH″ decreases and increases with the rise in temperature from 273K to 300K. Increase in temperature shifts the gas-particle partitioning for both NH_3 and HNO_3 toward the gas phase. For NH_3, a rise in temperature inhibits the partitioning towards NH_4^+, so a lower pH is needed to drive the reaction forward. As a result, the critical pH for NH_3 (pH″) shifts downward with temperature. For HNO_3, the similar effect in reduction of partitioning to particulate phase is observed with increase in temperature. To compensate, a higher pH is needed to favour the partitioning towards particulate phase, and that makes the critical pH′ to shift upward.

Together, ALWC and temperature define the boundaries between sensitivity zones by shifting the values of pH′ and pH″. Since this chapter focuses on the NH_x system, the gas-particle partitioning of $NH_3(g)$ and NH_4^+ across different locations and conditions is discussed in details in the upcoming sections. Temperature and RH also influence this partitioning by affecting the equilibrium between $NH_3(g)$ and NH_4^+, creating a complex interaction among these factors. Understanding how these parameters influence the NH_x system under different meteorological conditions is crucial, especially for the understanding the impact of precursor emissions on secondary inorganic aerosol formation. Given the multifaceted importance of the NH_x system, this chapter aims to provide a deeper insight into the gas-particle partitioning of the NH_x system, focusing on the role of temperature, RH, pH, and ALWC under

different regions over India. By doing so, this chapter contributes to a detailed understanding of NH_x partitioning system.

3.3 Patiala

Sampling over Patiala was conducted in two seasons, (1) Post-monsoon (October-November) (2) Winter (December-January), to investigate the factors influencing gas-particle partitioning of the NH_X system and associated isotopic fractionation. Details regarding the samplings and study area are mentioned in the experimental section.

3.3.1 Meteorological effect on NH_x partitioning over Patiala

Sampling in post monsoon season was carried out during October-November, which coincided with the paddy residue burning time over the IGP. Average $\delta^{15}N\text{-}NH_4^+$ was 9.8 ± 2‰ with no significant diurnal differences($p>0.05$), day-time and night-time values were 10.2 ± 2‰ and 9.4 ± 2‰ respectively. Meteorological parameters like average RH, temperature and wind speed during day-time were 48 ±10%, 29 ± 2 ºC and 2.1 ± 1 m/s respectively; while at night the same were 62 ± 14%, 22 ± 2 ºC and 2.2 ± 1 m/s respectively. Overall, the average RH, temperature and wind speed during the study period were 55 ± 14 %, 25 ± 4 ºC and 2.1 ± 1 m/s, respectively. The NH_4^+/SO_4^{2-} ratio during this period was found to be nearly equivalent, indicating that most of the available NH_4^+ had been used up in neutralizing SO_4^{2-} with little or no excess NH_4^+ remaining (Figure 3.2a.). Moreover, NO_3^- was mostly associated with other cations like K^+, Mg^{2+} and $Ca^{2+,}$ as shown by a strong positive correlation and a near-unity slope in Figure 3.4. This suggested that the formation of $(NH_4)_2SO_4$ was the dominant process over the formation of more volatile salts such as NH_4NO_3 or NH_4Cl.

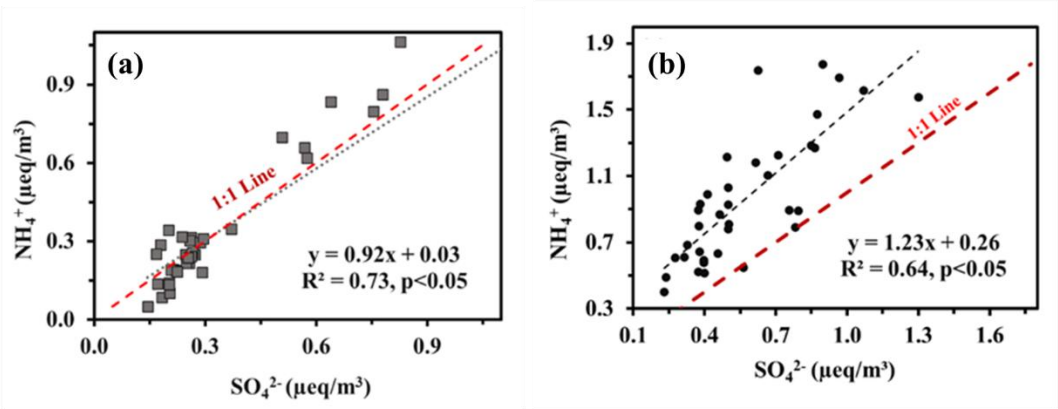

Figure 3.2. NH_4^+/ SO_4^{2-} equivalent ratio over Patiala during (a) post-monsoon (b) winter

In order to understand the role of RH and temperature on gas-particle partitioning over Patiala during post-monsoon, RH values were grouped into five distinct classes: (1) <46%, (2) 46–56%, (3) 56–66%, (4) 66–76%, and (5) >76%. The average $\delta^{15}N\text{-}NH_4^+$, RH, and T for each group are depicted in Table 3.1.

Table 3.1. Average $\delta^{15}N\text{-}NH_4^+$ (‰), relative humidity (RH), f and temperature (°C) for each RH group

Group	RH range (%)	Average $\delta^{15}N\text{-}NH_4^+$ (‰)	Average RH (%)	f (NH_4^+/NHx)	Average T (°C)
Group 1	<46	8.90	41.2	0.08	27.1
Group 2	46-56	9.50	49.9	0.17	25.8
Group 3	56-66	9.92	60.6	0.14	24.0
Group 4	66-76	10.35	73.9	0.29	23.7
Group 5	>76	10.92	85.0	0.30	21.6

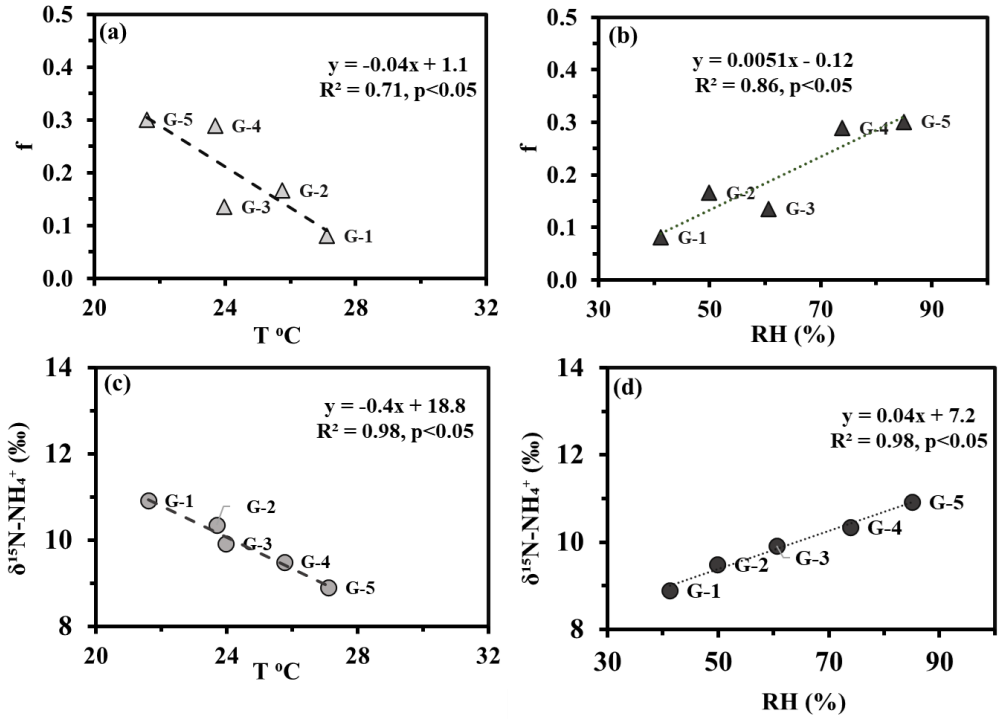

Figure 3.3. Relationship between (a) f and T (b) f and RH (c) $\delta^{15}N\text{-}NH_4^+$ and T (d) $\delta^{15}N\text{-}NH_4^+$ and RH

The partitioning factor (f) of NH_4^+ showed a clear negative correlation with temperature and a positive correlation with RH (Figure 3.3a and b). This indicated that lower temperature and higher RH favoured the partitioning of NH_3 (g) to NH_4^+. This was related to the equilibrium reversible equilibrium between NH_3 and NH_4^+, and the subsequent formation of NH_4^+ salts (s/aq) with other available anions during the study period. Conversation of NH_3 to NH_4^+ is controlled by the equilibrium reversible reaction (R1). The formation of $(NH_4)_2SO_4$ is thermodynamically favoured first, being non-volatile thus stable, there was no excess NH_4+ after the formation of $(NH_4)_2SO_4$. Any remaining NH_4^+ after $(NH_4)_2SO_4$ formation (NH_4^+ excess) subsequently can react with anions such as NO_3^- and Cl^- to form volatile salts like NH_4NO_3 and NH_4Cl, respectively (Behera et al., 2013; Renard et al., 2004; Scott & Cattell, 1978; Walters et al., 2019).

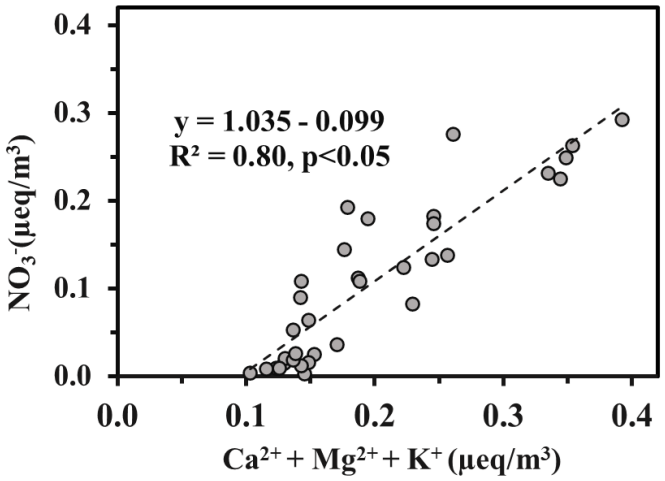

Figure 3.4. Relationship between (NO_3^- and sum of NVCs (Ca^{2+}, Mg^{2+}, K^+) over Patiala during post-monsoon. Concentrations are expressed in in equivalent unit.

Since $(NH_4)_2SO_4$ is thermally stable and less prone to volatilization, changes in temperature had limited impact on its stability. However, an increase in temperature likely shifted the NH_3-NH_4^+ equilibrium (R1) toward the gaseous NH_3(g), which explained the observed negative correlation between the partitioning factor (f) and temperature, and the positive correlation with RH (Figure 3.3a and b). If NH_4^+ had been present as more volatile forms like NH_4NO_3 or NH_4Cl, which have low deliquescence relative humidity (DRH), then a decrease in RH could have driven their dissociation (R6 or R7), enriching the remaining NH_4^+, similar to what was observed during winter. But, NH_4^+ existed mainly as $(NH_4)_2SO_4$ and due to its stability, a drop in RH would not significantly influence its partitioning unless the efflorescence RH was crossed. The positive relationship between δ^{15}N-NH_4^+ and RH, along with the negative relationship with temperature, further supports the interpretation that low temperature and high RH conditions favoured gas-to-particle conversion of NH_3 to NH_4^+ and hence higher δ^{15}N enrichment. These findings are consistent with earlier studies that also reported the influence of RH and temperature on NH_3-NH_4^+ partitioning (Walters et al., 2019; Zhang et al., 2020; Zhao et al., 2020).

During the winter, overall average temperature and RH were 14.2 ± 5 °C and 75 ± 17%, while day-time and night-time temperature and RH averaged around 18 ± 4 °C, 61 ± 10% and 10 ± 4 °C, 91 ± 5% respectively. Overall wind speed during winter was 2.3 ± 0.3 m/s, with no significant diurnal differences, day-time (2.3 ± 0.4 m/s), night (2.3 ± 0.2 m/s). Wind speed was fairly consistent throughout this time period. δ^{15}N-NH_4^+ averaged around 11.6 ± 1‰, exhibiting significant diurnal variability. Day-

time and night-time $\delta^{15}N\text{-}NH_4^+$ values were 12.1 ± 1‰ and 10.9 ± 1‰, respectively, although the concentrations of NH_4^+ remained largely unchanged.

Diurnal variations in $\delta^{15}N\text{-}NH_4^+$ observed during winter couldn't be attributed to shifts in emission sources, as the sources remained similar across the diurnal cycle, as discussed in details in the next chapter. Other factors like meteorology can play a significant role in the formation of secondary aerosols, and they can also influence the isotopic signature of NH_4^+(Wang et al., 2015). To better understand the role of meteorology on the partitioning, thus $\delta^{15}N\text{-}NH_4^+$, RH were grouped into 7 classes: 40-50%, 50-60%, 60-70%, 70-80%, 80-90%, 90-95%, and greater than 95%. Subsequently, the average $\delta^{15}N\text{-}NH_4^+$ associated with the RH range were calculated. A significant negative correlation was observed between the group-averaged RH and $\delta^{15}N\text{-}NH_4^+$ (R^2= 0.85, Figure 3.5b). This observation indicated that the volatilization of NH_4NO_3 under low RH condition, caused isotopic enrichment of the remaining NH_4^+. Further, the presence of a significant positive correlation between NH_4^+ and (SO_4^{2-} + NO_3^-) with a near unity slope, indicated towards the existence of NH_4NO_3 (Figure 3.5a). At night, the combination of lower temperatures and higher relative humidity likely suppressed volatilisation processes. This was supported by the absence of a strong negative correlation between $\delta^{15}N\text{-}NH_4^+$ and NO_3^- in night-time samples (Figure 3.5c). Similar negative correlation between $\delta^{15}N\text{-}NH_4^+$ and RH had been reported by previous study (Wu et al., 2021).

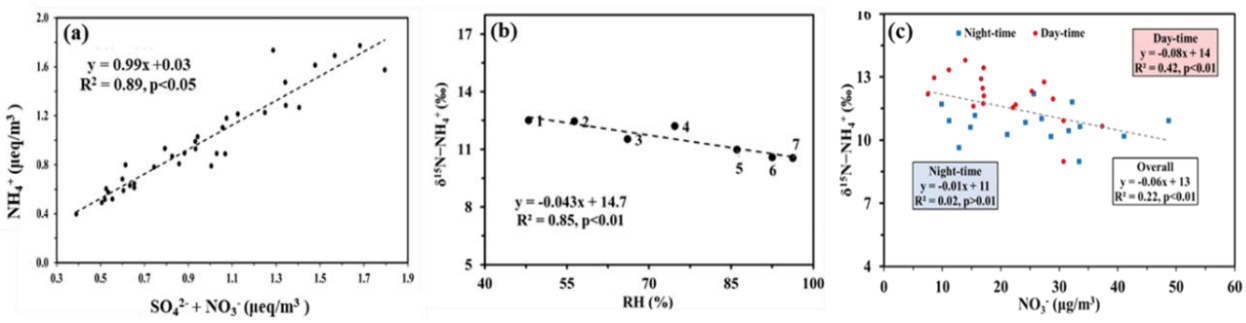

Figure 3.5. Relationship between (a) NH_4^+ and sum of NO_3^- and SO_4^{2-} (b) $\delta^{15}N\text{-}NH_4^+$ and RH groups. (c) $\delta^{15}N\text{-}NH_4^+$ and NO_3^- over Patiala during Winter. For details on the RH grouping see the text.

3.3.2 Effect of pH and ALWC over Patiala during post-monsoon

Aerosol pH and ALWC not only influences the NH_3-NH_4^+ gas-particle partitioning but also the extent to which PM mass concentration depends on this partitioning. Figure 3.6a depicted the overall pH and ALWC conditions with respect to the existing critical pH during the study period. Most samples fell within the HNO_3-sensitive region, indicating that the availability/emission of HNO_3 and its partitioning to NO_3^- influenced the PM mass concentrations during the study period. A smaller subset of samples lied in the dual-sensitive region, suggesting that on those days, fluctuations in both NO_3^- and NH_4^+ were important in affecting PM levels. A significant positive correlation between NO_3^- and $PM_{2.5}$ concentrations (Figure 3.6b) further supported that changes in HNO_3-NO_3^- partitioning had a consistent effect on PM levels. In the case of NH_4^+, two distinct patterns were observed. One group of samples had a significant positive correlation between NH_4^+ and $PM_{2.5}$ (Figure 3.7a), accompanied by higher ALWC and lower pH values. These samples further showed an elevated ALWC and lower pH and corresponded to the dual-sensitive zone. Conversely, the group of samples which were located in the HNO_3-sensitive region did not show any significant relationship between NH_4^+ and $PM_{2.5}$ concentrations.

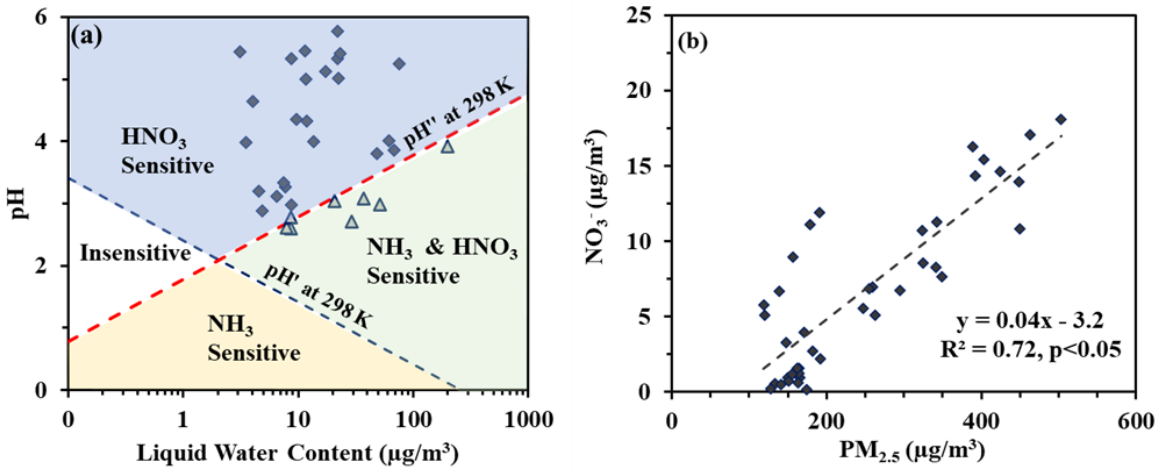

Figure 3.6. (a) Sensitivity of samples based on pH and ALWC, (b) Relationship between $PM_{2.5}$ and NO_3^- mass concentration during post-monsoon over Patiala

Additionally, samples in the dual-sensitive region exhibited a negative correlation between temperature and RH, where higher RH and lower temperatures were associated with increased ALWC and greater NH_4^+ partitioning (as indicated by higher f values; Figure 3.6b). This clearly indicated the presence of two partitioning regimes: one where PM mass concentration was sensitive to NH_4^+ partitioning, and another and another where it was not. These regimes were influenced by prevailing pH levels, ALWC, temperature, and RH. All of these factors critically influenced the extent to which gas-particle partitioning, which was either driven by HNO_3 alone or by both HNO_3 and NH_3, affected the overall PM load. Average $\delta^{15}N\text{-}NH_4^+$ and f exhibited higher values (11.8 ± 2‰ and 0.4 ± 0.1) in the former group as compared to that of the later (9.1 ± 2‰ and 0.1 ± 0.1). However, it should be noted that while f reflected only the gas-particle between NH_3 gas and NH_4^+ and the factors affecting the same, $\delta^{15}N\text{-}NH_4^+$ was affected by both the partitioning process and isotopic signature of the NH_3 source. Distinguishing the effect of source and partitioning is complicated and requires simultaneous isotopic measurement of both NH_3 (g) and NH_4^+.

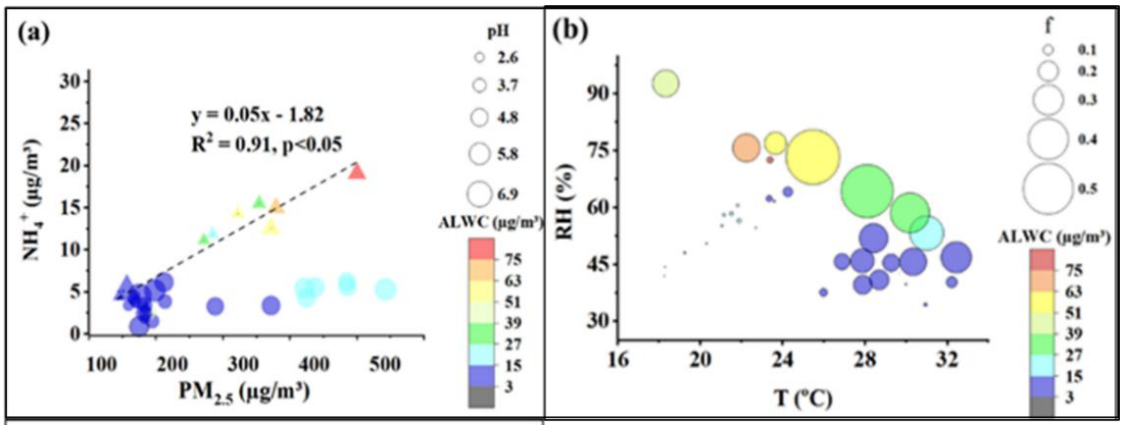

Figure 3.7. (a) Relationship between NH_4+ and $PM_{2.5}$ concertation and the influence of pH and ALWC on the same; triangle represents samples falling in the dual sensitive zone and circle represents samples in the HNO3-sensitive zone(b) Relationship between T and RH, and their effect on f (bubble size) and ALWC (colour).

3.4 Delhi

The average $\delta^{15}N\text{-}NH_4^+$ over Delhi was around 11.3 ± 2‰, with f value varying from 0.1 to 0.5 (average 0.4 ± 0.1). Meteorological conditions were characterised by average temperature of 17.3 ± 6°C, RH around 47.2 ± 17 % and wind speed of 2.5 ± 1m/s. During the study period, NH_4^+ was completely neutralised by SO_4^{2-} and NO_3^- and

present as both $(NH_4)_2SO_4$ and NH_4NO_3 as evident from the significant positive correlation and near unity slope in Figure 3.8.

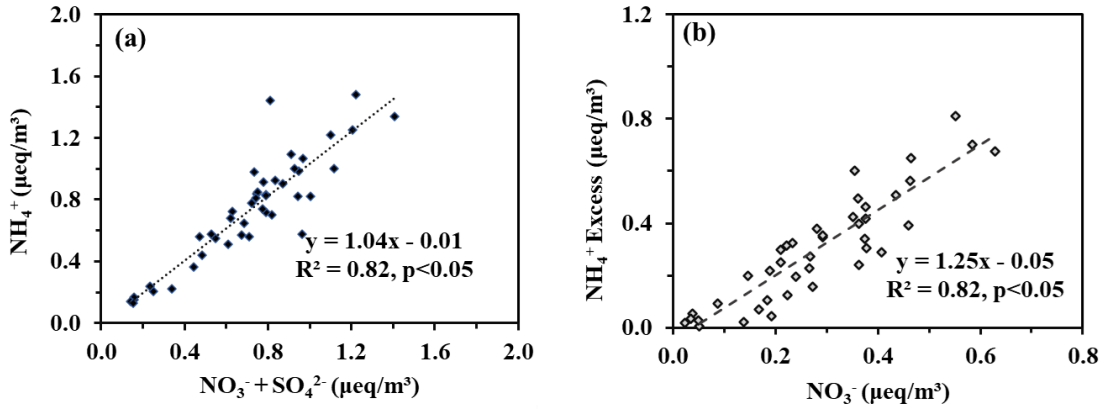

Figure 3.8. Relationship between (a) NH_4^+ and sum of SO_4^{2-} and NO_3^- (b) Excess NH_4^+ after the formation of $(NH_4)_2SO_4$ and NO_3^-

3.4.1 Effect of Meteorology

To examine how meteorological conditions influenced the NH_3-NH_4^+ partitioning and the resulting $\delta^{15}N$–NH_4^+ values, relative humidity (RH) was categorized into six groups based on the overall sample count and their distribution across RH ranges. These groups, labelled G1 through G6, corresponded to RH intervals of <30%, 30–40%, 40–50%, 50–60%, 60–70%, and >70%, respectively. A significant negative correlation was observed between the group-averaged RH and $\delta^{15}N$-NH_4^+ (R^2= 0.75, Figure 3.9), whereas no meaningful correlation was found between temperature and $\delta^{15}N$-NH_4^+. Further, a significant positive correlation between excess NH_4^+ with NO_3^- with a greater than unity slope suggested the complete neutralization of NO_3^- by NH_4^+ and thus formation of NH_4NO_3 (Figure 3.8b).

NH_3 is highly water-soluble due to its large Henry's law constant (~62 M/atm; Walters et al., 2019), which favours its dissolution into the aqueous phase under high RH conditions, thereby promoting the formation of particulate NH_4^+ through equilibrium reactions (e.g., R4). As RH decreases, NH_3(g) may escape to maintain thermodynamic equilibrium, which can lead to isotopic fractionation, where the escaping NH_3(g) was depleted in $\delta^{15}N$ leaving behind NH_4^+ enriched in ^{15}N in the particulate phase (Dong et al., 2022; Wang et al., 2013). Although theoretical models often emphasize temperature dependence in isotopic fractionation (Urey et al., 1947),

RH and temperature are typically inversely related in ambient conditions, making it difficult to isolate RH as an independent factor. However, observations from this study suggest that under conditions of both high temperature and high RH, the isotopic fractionation may be influenced by RH also, in addition to temperature. Therefore, future studies involving online, high time-resolution measurements of $NH_3(g)$, $NH_4^+$and their values, along with simultaneous monitoring of RH and temperature, are essential to better constrain the role of RH in isotopic fractionation processes.

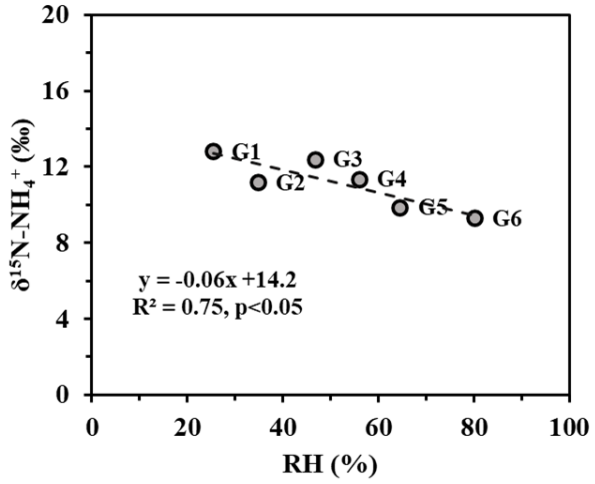

Figure 3.9. Relationship between $\delta^{15}N\text{-}NH_4^+$ and RH over Delhi. G1 to G6 refers to RH group, for detail see text

3.4.2 Role of pH and ALWC

In Delhi, alongside $PM_{2.5}$ offline sampling, online measurements of gas and particulate phase concentration of major ions and their precursor gases were conducted using the MARGA system. This high-resolution monitoring was done from 18th August 2023 to 14th December 2023, with data recorded at an hourly interval. Meanwhile, offline $PM_{2.5}$ samples were collected every alternate day between 24th October 2023 and 12th February 2024. Further details about the samplings are provided in Chapter 2. Since the two sampling periods partially overlapped, parameters such as pH, ALWC, and sensitivity regime derived from the online MARGA data were compared with those obtained from offline ion chromatographic analysis and CPCB gas-phase data associated with the $PM_{2.5}$ samples. This comparison was aimed to evaluate whether the pH and sensitivity regime results derived from offline $PM_{2.5}$ ion data and CPCB gas data aligned with those obtained from high-resolution online gas and particulate

measurements (Figure 3.10). Since online MARGA data were expected to offer greater accuracy due to their finer temporal resolution and simultaneous gas phase, a good agreement between the two would help to corroborate the use of $PM_{2.5}$ and CPCB-based estimations. This, in turn, would support the application of the same approach at other sites where only offline $PM_{2.5}$ and CPCB gas data were available, thereby enhancing confidence in the interpretation of aerosol pH and sensitivity regime assessments across different regions.

The average pH from online gas and particulate phase measurements using MARGA, after averaging the high-resolution data to match the $PM_{2.5}$ sampling durations, was 4.1 ± 0.4. For the same period, the average pH estimated from $PM_{2.5}$ ion data combined with CPCB gas concentrations was 3.8 ± 0.7, with no significant difference observed between the two approaches. As evident figure 3.4 in both the data, samples fell mostly in the HNO_3-sensitive zone. This suggests that pH and sensitivity regime assessments based only on $PM_{2.5}$ data and CPCB gas measurements aligned well with those based on detailed online gas and particulate data. Therefore, for other sites where only $PM_{2.5}$ and CPCB data were available, the estimated pH and sensitivity zones can be considered reliable. While some bias was introduced by using CPCB gas data, this was evaluated using the Normalised Mean Bias (NMB) as per literature (Emery et al., 2017; Henneman et al., 2017; Liu et al., 2019) and the results were within acceptable limits. Overall, the interpretations regarding Critical pH and sensitivity regimes remained valid and consistent.

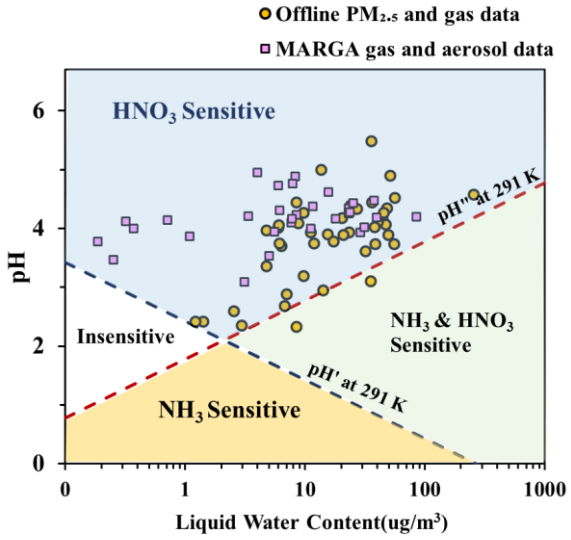

Figure 3.10. Comparison of pH and Sensitivity Regimes Derived from Offline $PM_{2.5}$-Based Measurements and Online High-Resolution Data

As evident from Figure 3.10, most of the samples in both offline and online measurement fell on the HNO_3 sensitive zone. This meant that HNO_3-NO_3^- partitioning affected $PM_{2.5}$ concentration during the study period. This was likely because of the presence of sufficient NH_4^+, as evident from Figure 3.8, making HNO_3-NO_3^- partitioning the limitation factor in influencing PM concentration. Additionally, an existence of a moderately high pH conditions (>2) likely driven the system into HNO_3 sensitivity. The influence of NO_3^- on PM level, is further supported by a moderately significant positive correlation between $PM_{2.5}$ and NO_3^- concentration in Figure 3.11. Regardless of the locations, transition from sensitivity (HNO_3 or NH_3 or both) to insensitivity, where PM load became unresponsive to either precursor, occurred at pH ~ 2. This meant even at low pH, a low ALWC could make the domain NH_3 insensitive, aligning with the transitional pH reported in previous studies (H. Guo et al., 2015, 2016, 2018; Nenes et al., 2020; Shi et al., 2019). Once sensitive, further regime transitions (e.g., from HNO_3-sensitive to NH_3-sensitive or dual-sensitive) were primarily driven by changes in pH and ALWC both.

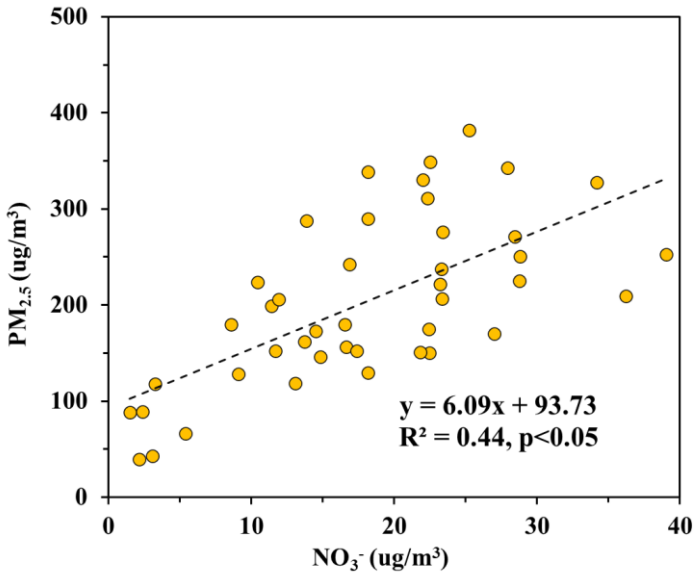

Figure 3.11. Relationship between $PM_{2.5}$ and NO_3^- concentration in offline samples over Delhi.

To better evaluate the relationship between aerosol pH and gas-particle partitioning, theoretical ε values were calculated using a mathematical framework that relates partitioning efficiency to aerosol pH, temperature, and ALWC, as outlined in previous studies (H. Guo et al., 2016, 2018; Nenes et al., 2020). This approach involved calculating ε and pH under specified thermodynamic conditions and plotting them to

generate idealized S-shaped curves for both the HNO_3-NO_3^- and NH_3-NH_4^+ systems. These curves illustrate how partitioning varies with pH at a given temperature and ALWC, helping to visualise sensitivity zones and transitions. Following this, measured $\varepsilon(NH_4^+)$ or f values and pH estimates derived from ISORROPIA-II model outputs were overlaid on the theoretical curves to assess the partitioning behaviour with change in pH.

Overall ALWC during the study period ranged from 1.2 µg/ m^3 to 55.6 µg/ m^3, with an average of 23.6 ± 17 µg/ m^3, indicating substantial variability in water content. To understand how it affected partitioning behaviour, theoretical ε values were calculated using the average ALWC and an ambient temperature of 291 K, representing mean sampling conditions. When the observed $\varepsilon(NH_4^+)$ values and the corresponding aerosol pH were plotted on this theoretical ε-pH curve, the majority of the samples fell within the HNO_3-sensitive zone, with a very few numbers lying in the dual-sensitive regime. This matched well with the sensitivity zones determined through critical pH analysis, as shown in Figure 3.12a. The curve generated using average ALWC, however, did not capture the pH-insensitive zone. Since no samples were observed in that region, a second theoretical ε-pH curve was generated using the minimum observed ALWC value of 1.2 µg/ m^3 to explore partitioning under low-water conditions. When samples with ALWC less than 5 µg/m^3 were plotted on this low-ALWC curve, a narrow pH-insensitive zone appeared between the two curves. Yet, even these low-ALWC samples continued to lie within the HNO_3-sensitive regime, consistent with the classification from the pH-ALWC framework (Figure 3.12b).

Although the ε-pH curve based on average ALWC represented a wide span of liquid water content, it accurately reflected the observed sensitivity pattern during the study. Both the pH-ALWC and ε-pH representations showed a similar distribution of sensitivity zones, with most samples being HNO_3-sensitive and a few classified as dual-sensitive. This consistent pattern suggested that over this sampling location, changes in aerosol pH, rather than ALWC, primarily influenced the shift from HNO_3 to dual sensitivity. If variation in ALWC had been the key driver, then the ε-pH plot generated at fixed ALWC would have shown a different distribution. Instead, the similarity in patterns across both representations confirms the dominant role of pH in controlling the transition. However, this may vary spatially and temporally depending upon several factors like temperature, existing aerosol pH and ALWC, RH etc. In general, when existing pH and ALWC conditions are close to the crossover point between regimes,

even minor changes in either variable could shift the system's sensitivity. The transition to the pH-insensitive regime appear to depend on both moderately low pH and reduced ALWC, under which $PM_{2.5}$ levels became less responsive to changes in NH_3 or HNO_3 concentrations.

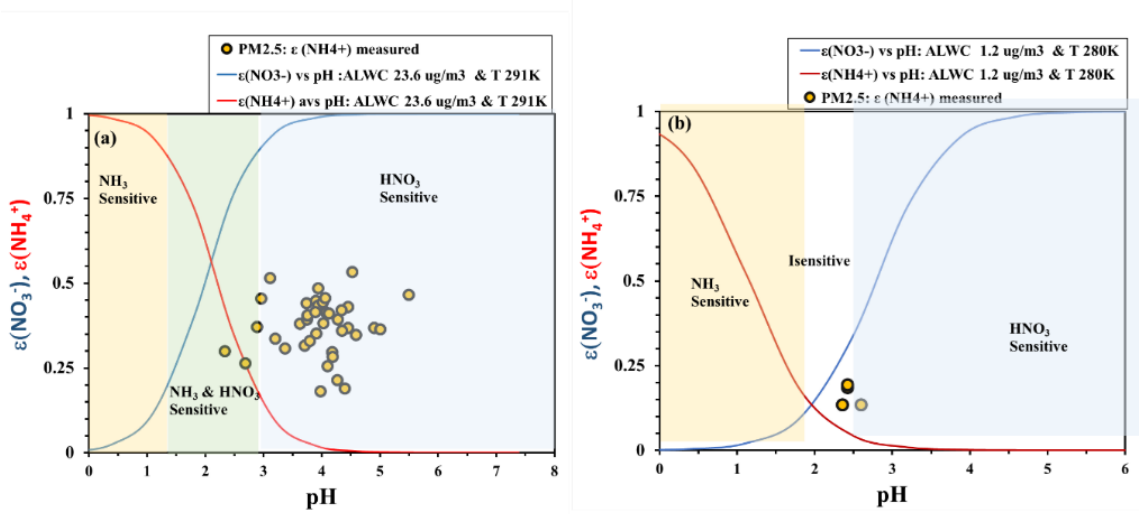

Figure 3.12. Theoretical gas-particle partitioning curves for NO_3^- ($\varepsilon(NO_3^-)$, blue) and NH_4^+ ($\varepsilon(NH_4^+)$) as a function of aerosol pH, overlaid with observed $\varepsilon(NH_4^+)$ and pH values for Delhi samples. (a) Curves based on average ALWC (23.6 µg/m³) and T = 291 K. (b) Curves based on actual low ALWC (2 µg/m³) and T = 280 K for the four samples shown.

Further, when the observed $\varepsilon(NH_4^+)$ values and their corresponding pH measurements closely matched the theoretically derived ε-pH relationship, and this alignment was further reflected in the classification of aerosol samples within sensitivity zones based on the pH-ALWC framework using critical thresholds, it indicated that the aerosol system was predominantly influenced by thermodynamic equilibrium. This consistency across both representations indicated that the gas-particle partitioning of NH_3 and HNO_3 happened under equilibrium conditions, with minimal deviation due to kinetic limitations. The ISORROPIA-II model have captured the thermodynamic state of the aerosol well, as the partitioning behaviour of NH_4^+ was effectively constrained by pH and ALWC. Notably, although the ε-pH analysis used a fixed average ALWC value, the high degree of agreement with the variable-ALWC pH-ALWC framework implied that ALWC played a secondary role in controlling sensitivity regimes at this location. Instead, aerosol pH remained the dominant factor in determining whether the system was HNO_3-sensitive or in transition toward a dual-sensitivity. These findings agree well with existing works (Nenes et al., 2020; Guo et al., 2018) which emphasized the critical role of aerosol pH in controlling gas-particle

equilibrium in NH_3-rich environments. The overall similarity in sensitivity classification across both plots also pointed to the key role of HNO_3-NO_3^- partitioning in modulating PM levels, with NH_3 being present in sufficient quantities to buffer changes in pH and maintain the stability of the partitioning regime.

3.5 Ahmedabad

Sampling over Ahmedabad was conducted during winter (Dec-Jan) and summer (May-June). The average temperature, RH and wind speed during winter and summer were 22 ± 5°C, 57 ±11%, 2.8 ± 1 m/s and 34 ± 4 °C, 46 ± 17, 4 ± 1 m/s respectively. Average boundary layer height during winter and summer was 456 ± 351m and 1035 ± 495m, respectively. The average $\delta^{15}N$-NH_4^+ during winter and summer were 12.4 ± 2‰ and 11.3 ± 3‰ respectively. During winter, most of the samples showed a complete neutralization of SO_4^{2-} and partial neutralization of NO_3^- by NH_4^+ was indicated by near unity and less than unity ratio (Figure 3.13a and c), coupled with a significant positive correlation in both cases. This observation indicates the formation of NH_4NO_3 by the excess NH_4^+ after forming $(NH_4)_2SO_4$. During summer, a moderate but statistically significant correlation ($p < 0.05$) was observed between SO_4^{2-} and NH_4^+, with their equivalent ratio falling below 1 (Figure 3.13c). This indicates that SO_4^{2-} was present in excess and that complete neutralization by NH_4^+ was not achieved. Excess SO_4^{2-} over NH_4^+ could be related to the fact that SO_4^{2-} in atmosphere was mainly formed via oxidation of SO_2 by hydroxyl radical (•OH), which was in turn favoured by high summer time temperatures and solar radiations. Additionally, elevated temperature and lower RH during this season favoured gas-phase NH_3, thereby shifting the NH_3-NH_4^+ equilibrium away from particulate-phase NH_4^+. These conditions explain the higher relative abundance of SO_4^{2-} compared to NH_4^+ in summer. In contrast, winter is characterized by lower temperatures and higher RH, conditions that favour the partitioning of gaseous NH_3 into NH_4^+. As a result, NH_4^+concentrations tend to be higher enough to neutralise the acidic species. The gas-particle partitioning behaviour of NH_3 and NH_4^+, along with the influence of aerosol pH and presence of alkaline species (such as calcium and/or potassium). Seasonal meteorological effects on NH_x partitioning

$\delta^{15}N$-NH_4^+ during summer, showed a significant negative correlation with temperature and positive correlation with RH (Figure 3.14). This implicated a higher

temperature and lower RH favoured the equilibrium partitioning in R1 towards the particulate phase and thus, higher $\delta^{15}N\text{-}NH_4^+$. However, in winter, despite the presence of sufficient NH_4^+, no significant correlation between $\delta^{15}N\text{-}NH_4^+$ and meteorological parameters. was observed.

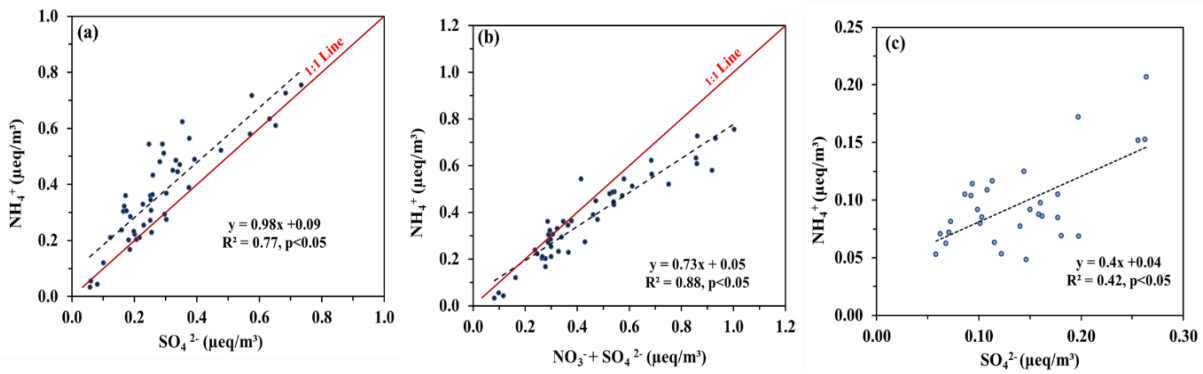

Figure 3.13. (a) NH_4^+ vs. SO_4^{2-} over Ahmedabad during winter (b) NH_4^+ vs. NO_3^- + SO_4^{2-} over Ahmedabad during winter (c) NH_4^+ vs. SO_4^{2-} over Ahmedabad during summer

A lack of correlation between $\delta^{15}N\text{-}NH_4^+$ and meteorological parameters during winter could be due to mixed influence of emission sources as discussed in details in the next chapter. $\delta^{15}N\text{-}NH_4^+$ is influenced by both the isotopic signature of its precursors as well as gas-particle partitioning, and also the factors influencing them. The lack of observable effects of meteorology in winter was likely due to the greater variability of emission. Thus, the effect of multiple sources on $\delta^{15}N\text{-}NH_4^+$ masked the effect of meteorology-driven changes in gas-particle partitioning, detail discussion on sources is in the next chapter.

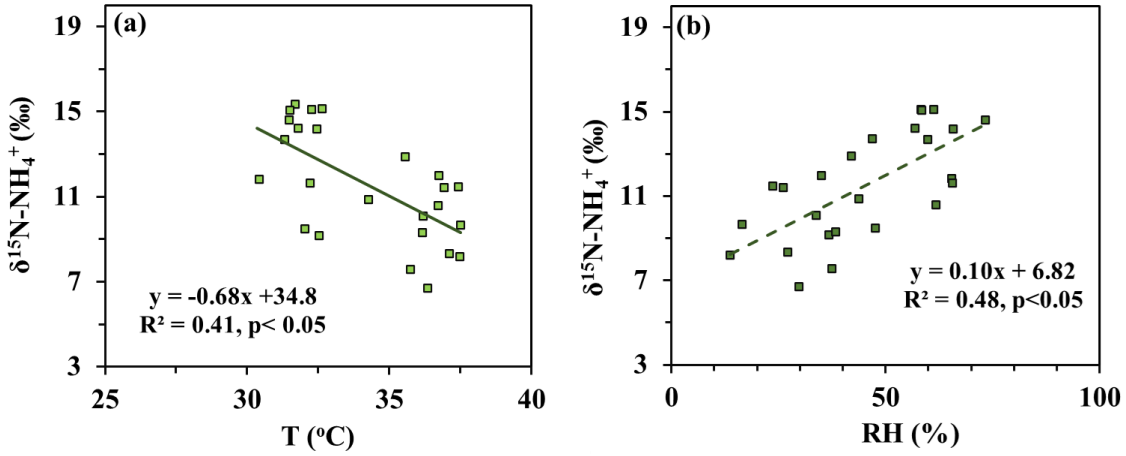

Figure 3.14. Relationship between $\delta^{15}N\text{-}NH_4^+$ and (a) Temperature (b) RH in Ahmedabad during summer

3.5.1 Role of pH and ALWC on seasonal NH_x partitioning over Ahmedabad

In order to assess the role of pH and ALWC on the gas-particle partitioning and thus on PM load, critical pH was calculated for winter and summer samples. Average ALWC and pH were 16.3 ± 15 µg/m³, 3.6 ± 1 and 5.2 ± 4 µg/m³, 3.6 ± 2 during winter and summer respectively. A shift in the critical pH values for HNO_3 and NH_3 was observed from winter to summer, along with a broader sensitivity zone during winter (Figure 3.15a and 3.17a). This broader range is attributed to the lower overall temperatures in winter compared to summer. In winter over Ahmedabad, almost all data points fell within the HNO_3-sensitive region (Figure 3.15a). This observation suggested that HNO_3(g) and NO_3^- were limiting species influencing both aerosol pH and $PM_{2.5}$ concentration. This observation aligned with the near unity equivalent ratio of NH_4^+/SO_4^{2-}, reflecting complete neutralization of SO_4^{2-}. In such a scenario, formation of additional particulate by NH_4^+ would be dependent upon availability of HNO_3 or HCl; however, Cl^- concentration was very low with no significant correlation with NH_4^+. This indicated that the change in PM concentration relied on the availability of HNO_3 and its partitioning to NO_3^-. Hence, under these conditions, the aerosol system becomes sensitive to HNO_3, and variations in its ambient levels played a more dominant role in governing PM load and acidity. A significant positive correlation between $PM_{2.5}$ and NO_3^- (Figure 3.15b) further attested the dominance of HNO_3-NO_3^- partitioning in influencing PM mass concentration.

It is important to note that during winter, the majority of HNO_3 is partitioned into the particulate phase. Several studies have reported that f_{NO3}-(NO_3^-/NO_3^{-T}) tends to be high in winter, often approaching complete partitioning. In contrast, during summer, this fraction shows more variability, with values ranging from partial to nearly complete conversion (Gupta et al., 2003; Nojiri et al., 2022; Shi et al., 2019). Since gas-phase HNO_3 data was not available for this site, and such measurements are generally limited across most locations in India, a sensitivity test was conducted for Ahmedabad during the summer season. In winter, NO_3^- mainly exists in the particulate phase (f_{NO3} near unity), making its distribution more predictable. In contrast, summer conditions can lead to greater variability in how NO_3^- is partitioned between gas and particulate phases. This test was carried out to understand how changes in assumed HNO_3 levels

could influence aerosol pH during the summer period. From existing studies, f_{NO3-} values during warmer seasons were assumed to be vary as low as 0.2 and as high as 1, thus encompassing all possibilities, although such extreme variations aren't reported for a particular season for a given area as far as our knowledge. The pH was calculated on all the instances, and together with ALWC, samples were categorised on the Sensitivity Regime plot.

The sensitivity analysis showed that NO_3^- partitioning (f_{NO3-}) influenced PM concentration in a consistent manner across all tested scenarios, with the system remaining within the HNO_3-sensitive regime throughout (Figure 3.16). Despite variations in assumed partitioning ratios, the overall thermodynamic state of the aerosol remained stable. This stability could be attributed to several factors: high ambient concentrations of NH_3 and presence of NVCs such as Ca^{2+} and Mg^{2+}, K^+, resulted in a pH higher than the critical threshold for NH_3 partitioning. Additionally, the NO_3^- concentration was relatively low during the summer, limiting the potential impact of changes in HNO_3 on aerosol composition.

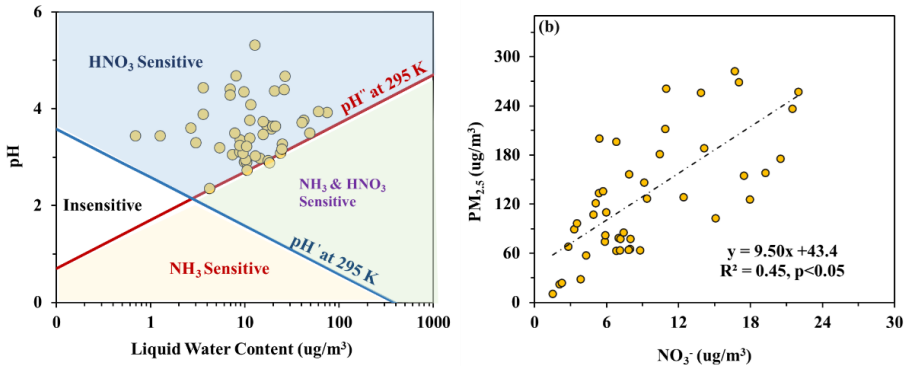

Figure 3.15. Sensitivity regime (a) and (b) relationship between PM concentration and NO_3^- concentration during winter over Ahmedabad

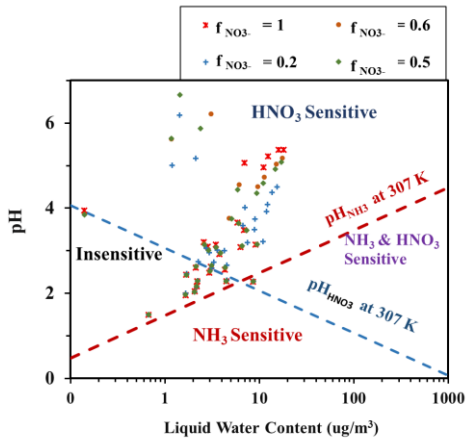

Figure 3.16. pH and ALWC at different f_{HNO3} during summer

Consistent with this, most samples during summer were found in the HNO_3-sensitive zone, while a few were located in the insensitive region (Figure 3.17a). Unlike winter, the NH_4^+/SO_4^{2-} equivalent ratio remained below 1, indicating that complete neutralization of SO_4^{2-} by NH_4^+ did not occur, and excess NH_4^+ was absent. Thus, the presence of samples in the HNO_3-sensitive region was not driven by NH_4^+ excess. Instead, the elevated presence of $Ca^{2+}$and Mg^{2+} and K^+, likely from fine dust, appeared to play a key role in raising aerosol pH, thus shifting the system away from NH_3 sensitivity. This was supported by a significant positive correlation between the sum of Ca^{2+} Mg^{2+} K^+ and pH (Figure 3.17c). Moreover, a clear relationship between particulate NO_3^- and $PM_{2.5}$ further indicated the role of HNO_3 partitioning in influencing PM levels. The few samples that appeared in the insensitive regime were characterized by moderate pH and low ALWC, conditions that were unfavourable for efficient partitioning of either NH_3 or HNO_3 In these cases, no strong correlation between non-volatile cations and pH was observed, suggesting that other thermodynamic constraints or limited precursor availability may have governed the observed insensitivity.

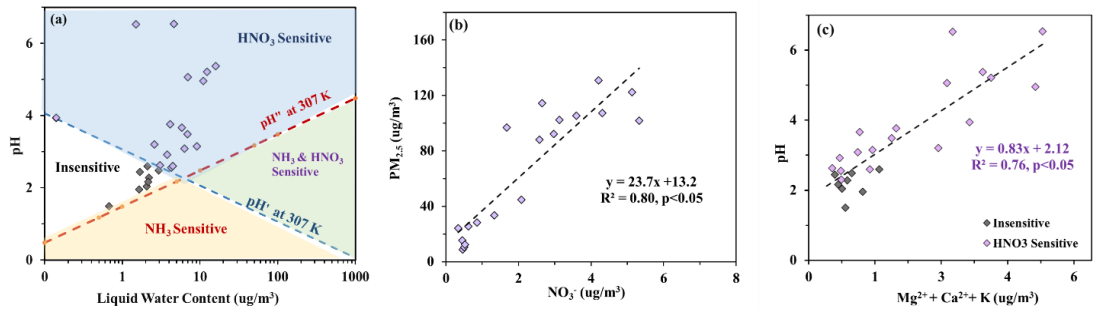

Figure 3.17. Sensitivity regime (a) and (b) relationship between PM concentration and NO_3^- concentration (b) pH and NVCs (c) during summer over Ahmedabad

3.6 North East (Dibrugarh and Shillong)

During the sampling period, average RH, temperature and wind speed over Dibrugarh were $81 \pm 6\%$, 16 ± 2 °C, and 1.7 ± 0.4 m/s respectively, whereas over Shillong they were $64 \pm 11\%$, 18 ± 4 °C and 2.2 ± 1 m/s. Dibrugarh showed an average $\delta^{15}N\text{-}NH_4^+$ of 13 ± 2‰, with no significant difference between $PM_{2.5}$ (12.8 ± 2‰) and PM_{10} (13.3 ± 2‰) samples. A comparable $\delta^{15}N\text{-}NH_4^+$ value was also observed at Shillong, with an average of 11.8 ± 3‰. Similar $\delta^{15}N\text{-}NH_4^+$ was reported in Southeast Asia (W. Guo et al., 2021; Lim et al., 2020; Pan et al., 2018; Park et al., 2018).

At Shillong, NH_4^+ was mostly neutralised by SO_4^{2-}, as indicated by the linear regression parameters (slope = 0.85, R^2 = 0.95, Figure 3.18b) Although NH_4^+ was excess at Dibrugarh as evident by greater than unity slope in figure 3.7, no significant correlation between NH_4^+ and NO_3^- was obtained. A similar lack of correlation was also found at Shillong, suggesting that a considerable formation of NH_4NO_3 was not there at either site.

3.6.1 Meteorology

At Dibrugarh, no significant relationship was observed between $\delta^{15}N\text{-}NH_4^+$ and RH, despite the high RH levels ($81 \pm 6\%$) and relatively low temperatures (16 ± 2 °C). However, a moderate but statistically significant negative correlation was observed between temperature and $\delta^{15}N\text{-}NH_4^+$(Figure 3.19), indicating that a lower temperature favoured NH_3 to NH_4^+ partitioning, thus resulting in an elevated $\delta^{15}N\text{-}NH_4^+$. In contrast, Shillong, which experienced a broader range of both RH ($64 \pm 11\%$) and temperature (18 ± 4 °C), did not exhibit any significant correlation between $\delta^{15}N\text{-}NH_4^+$ and meteorological variables.

Although RH and ALWC typically promote NH_3 to NH_4^+ conversion under cool and moist conditions, this trend was not clearly reflected in $\delta^{15}N\text{-}NH_4^+$ patterns at either site. This observation further suggests that $\delta^{15}N\text{-}NH_4^+$ variability did not solely depend on meteorological influences. Instead, it can also be governed by other factors such as equilibrium fractionation during gas-particle exchange and the isotopic signatures of precursor NH_3. The lack of consistent $\delta^{15}N\text{-}NH_4^+$- meteorology relationships across both locations could also be due to the relatively narrow

meteorological variation during the study period, as well as the complex interplay of atmospheric transport and processing that could have influenced isotopic signatures.

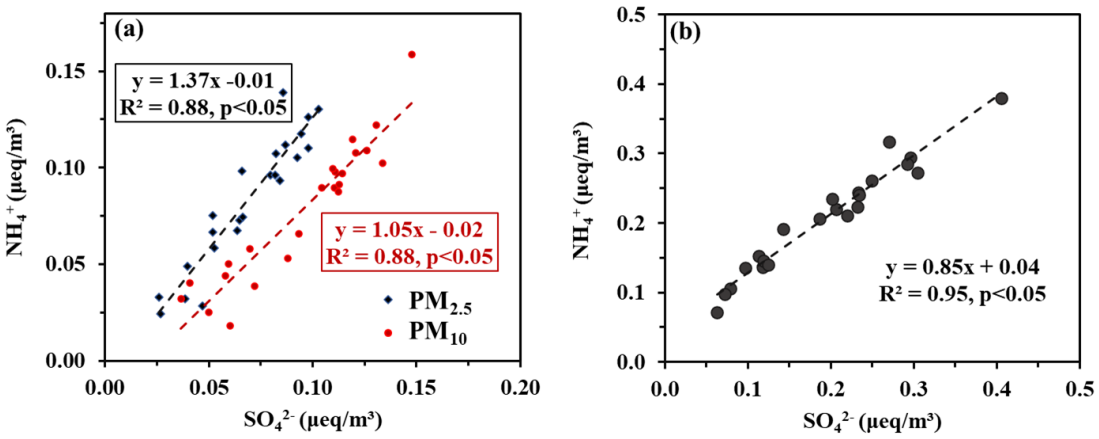

Figure 3.18. Correlation between NH_4^+ and SO_4^{2-} in (a) Dibrugarh ($PM_{2.5}$ and PM_{10}) (b) Shillong

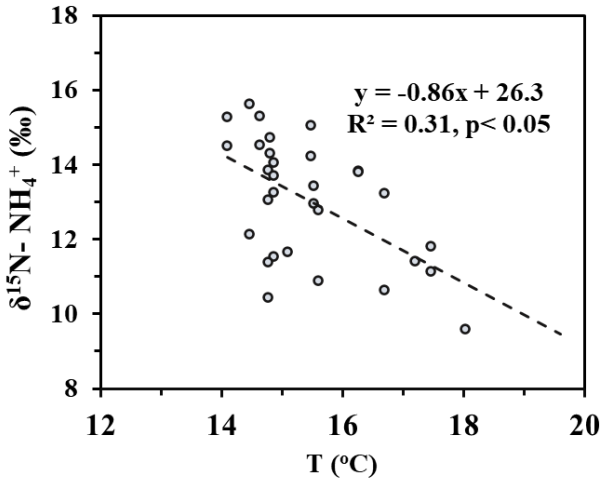

Figure 3.19. Relationship between temperature and $\delta^{15}N$-NH_4^+ over Dibrugarh

3.6.2 Sensitivity regimes over Dibrugarh and Shillong

Aerosol pH and ALWC were similar between the two sites, with values of 3.3 ± 0.3 and 10.6 ± 6 µg/m^3 at Dibrugarh, and 2.9 ± 0.4 and 10.5 ± 7 µg/m^3 at Shillong, respectively. Critical pH analysis indicated that both locations predominantly fell within the HNO_3-sensitive regime. However, a small number of samples from Shillong

extended into the dual-sensitive zone, due to its slightly more acidic conditions. Overall, most samples at both locations showed HNO_3 sensitivity, consistent with moderate ALWC and higher pH. Further, NO_3^- showed a significant positive correlation with PM concentration, supporting the influence of HNO_3 partitioning or availability at both the locations (Figure 3.20). When observational data from both sites were plotted over theoretical $\varepsilon(NH_4^+)$-pH curves, a strong match was observed with the HNO_3-sensitive regime (Figure 3.21), as identified by critical pH thresholds and ALWC. This agreement indicated reliable model predictions and suggested that partitioning at both sites occurred under thermodynamic equilibrium.

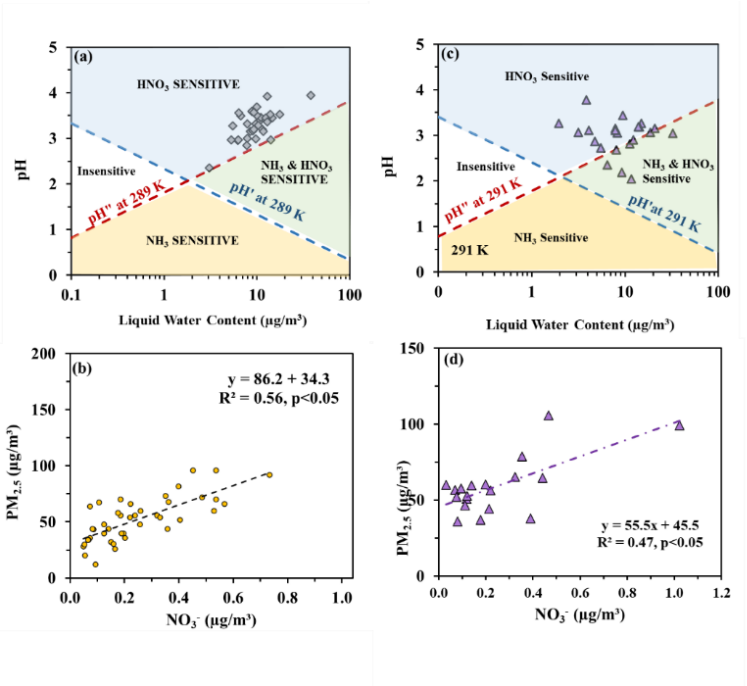

Figure 3.20. Aerosol sensitivity regimes (a, c) and PM concentration-NO_3^- correlations (b, d) at Dibrugarh and Shillong.

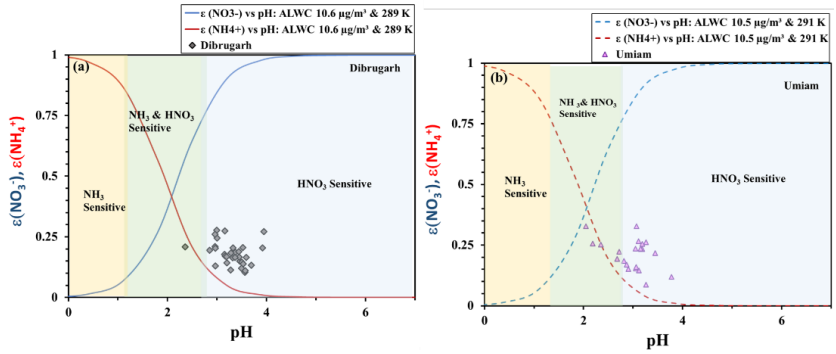

Figure 3.21. Theoretical gas-particle partitioning curves for NO_3^- ($\varepsilon(NO_3^-)$) and NH_4^+ ($\varepsilon(NH_4^+)$) as a function of aerosol pH, overlaid with observed $\varepsilon(NH_4^+)$ and pH values for (a) Dibrugarh (b) Shillong.

Chapter 4
Sources of NH_x over different region in Indian Subcontinent

4.1 Introduction

NH_3 and its particulate form, NH_4^+, are important contributors to the formation of fine particulate matter ($PM_{2.5}$), and play a significant role in the deterioration of regional air quality, health and biodiversity (Ojha et al., 2020; Saraswati et al., 2018; Sudheer & Rengarajan, 2015). Globally, NH_3 emissions have increased annually by, approximately 621.6 Gg NH_3-N (Behera et al., 2013). Despite this increase, existing emission inventories, both at the global and regional scales, remain insufficient in capturing the spatial and temporal variability of NH_3 emissions over the Indian subcontinent (Beale et al., 2022; Yamaji et al., 2004). This creates a major challenge in effectively addressing air quality concerns across the region. These concerns are relevant for India, where multiple sources contribute to NH_3 emissions, and their relative importance changes with location and season. The major sources of NH_3 include agriculture and urban wastes emissions, biomass burning, thermal power generation, and road transport. Together, these different sources highlight the importance to study regional NH_3 emissions.

India has been recognised as a global hotspot for atmospheric NH_3 emissions, driven by its large agricultural sector, dense livestock population, rising urbanisation, and growing transport and industrial activities (Kuttippurath et al., 2020; Ma et al., 2025). The country's wide range of climates, landscapes, and land use patterns causes NH_3 sources to differ significantly across regions. For instance, emissions from agriculture may dominate in rural zones, while traffic and urban waste play a larger role in cities. Further, meteorological factors affect the distribution of NH_3 concentrations on local and regional scale. This complexity makes it essential to identify and quantify regional NH_3 sources accurately. Stable isotope of NH_x is an excellent tool for quantifying the contribution of different sources to NH_3 emissions. Stable isotope of NH_x ($\delta^{15}N$ of NH_3 and NH_4^+) is an excellent tool for quantifying the contribution of

different sources to NH_3 emissions. Different NH_3 sources have distinct $\delta^{15}N$ signatures, NH_3 from combustion related emissions like BB and CFPPs have a more enriched isotopic signature as compared to that of agricultural emissions (Wu et al., 2021; Xiao et al., 2024; Li et al., 2023). The details on the isotopic signatures of individuals sources are given in Chapter 2.

In this context, the present chapter aims to carry out source apportionment of NH_3 over different regions of India, a semi-urban site located within the Indo-Gangetic Plain (Patiala), an urban mega city within IGP (Delhi), a major northwestern urban city (Ahmedabad), rural northeastern region (Dibrugarh and Shillong). These locations with diverse settings will help to our understanding of spatial variability of NH_3 sources. This will further contribute to develop a more accurate emission inventories and targeted mitigation strategies.

4.2 Sources of NH_3 and NH_4^+ over Patiala

Average NH_4^+ concentration was 6.2 ± 4.5 μg/m³ and 17.3 ±7.0 μg/m³ and contributing around 76% and 72% and to WSIN over Patiala during post-monsoon and winter, respectively. Near unity equivalent ratio of NH_4^+/SO_4^{2-} indicates complete neutralization of the acidic species by $NH_3(g)$, and formation of $(NH_4)_2SO_4$ major NH_4^+ species during both the seasons (Figure 3.2). During winter, significant diurnal differences in $\delta^{15}N\text{-}NH_4^+$ was observed as mentioned in details in Chapter 3.

Post-monsoon over Patiala was marked by 2 windspeed conditions, a period characterised by calmer condition (wind speed less than the average wind speed) till 29th October, while rest of the samples characterised by windy conditions with wind speed higher than the average (Figure 4.1). The implication and importance of this observation will be discussed in the later sections. During winter f value was consistent around 0.3, however during post-monsoon f varied from 0.1 to 0.3, owing to meteorological conditions. The post-monsoon sampling period (October-November) also coincides with large scale paddy residue burning, during which farmers burn paddy straw during October-November. Emissions from this burning include both aerosols and gases, which significantly degrade ambient air quality, leading to reduced visibility, adverse health effects, and impacts on regional radiative forcing (Patel et al., 2021; Sahu et al., 2021). Although efforts have been made in recent years to reduce emissions from paddy residue burning (PRB), the emission load has continued to grow, increasing

from around 30 million tonnes in 1960 to nearly 50 million tonnes by 2016 (Kumar et al., 2019). Due to this, the post-monsoon season is notably influenced by PRB activity. The sampling period is therefore divided into three phases: pre-burning, burning, and post-burning.

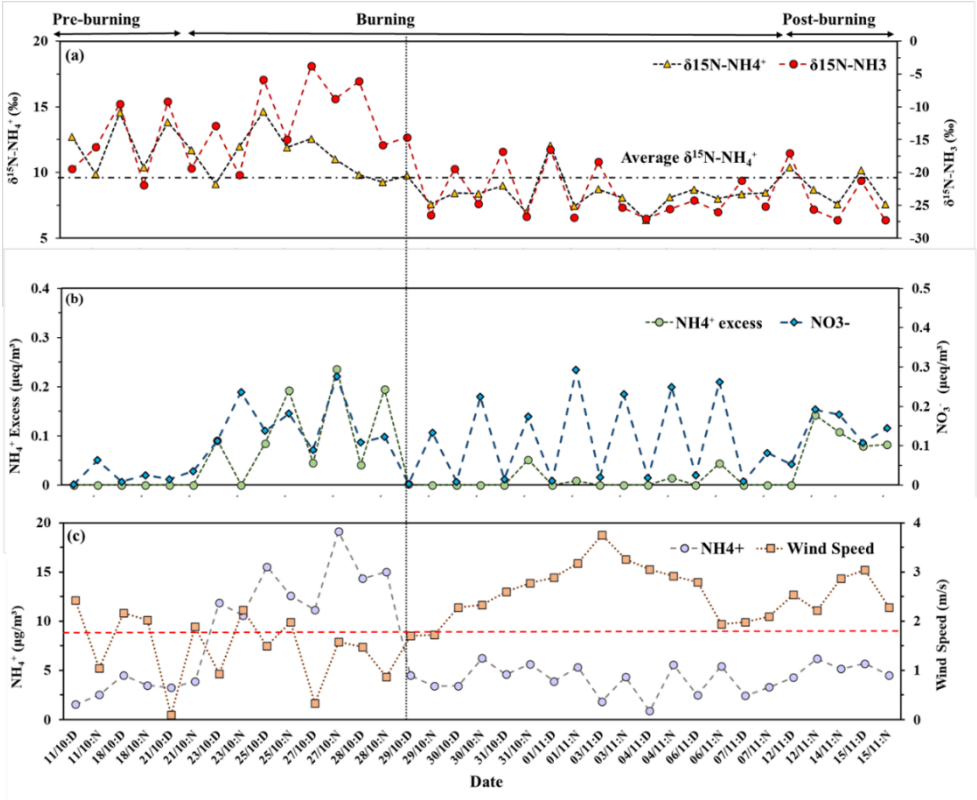

Figure 4.1. Time series of (a) $\delta^{15}N\text{-}NH_4^+$ and $\delta^{15}N\text{-}NH_3$ (b) NH_4^+ excess and NO_3^- concentration (c) NH_4^+ concentration and wind speed. D and N refer to day-time and night-time respectively

During post-monsoon, agriculture, urban wastes (33 ± 10%) and biomass burning (36 ± 18%) were the dominant contributors. These were followed by CFPPs (21 ± 10%) and traffic exhaust (10 ± 5%) (Figure 4.2). During this sampling period, it was observed that days with calmer condition, characterised by low wind speed, (below than the overall average wind speed of ~2 m/s) showed an elevated $\delta^{15}N\text{-}NH_4^+$ and thus, $\delta^{15}N\text{-}NH_3$. In contrast, windy days (wind speed higher than average value) exhibited quite the opposite trend. (Figure 4.1). To better understand these variations, the data was categorized into two subsets based on wind speed. The first group included samples from calm periods (wind speed below the overall average), while the second group represented windier conditions (above average wind speed). Source apportionment was conducted separately for each group, which revealed that during calm conditions (representing the dominance of local emissions), biomass burning (44 ± 20%) and

CFPPs (27 ± 12%) were the primary contributors, while the influence from agriculture was lower (20 ± 12%). Conversely, under windier conditions (representing the influence of regional emissions), agriculture and urban wastes emerged as the major source (46 ± 8%), followed by biomass burning (30 ± 13%) and CFPPs (14 ± 8%) (Figure 4.2). Traffic emissions remained consistent across both wind regimes.

Wind speed emerged as an important factor in controlling the spatial influence of NH_3, where with low wind speeds, atmospheric mixing was limited, which allowed local emission sources to dominate. Under these calm conditions, local contributors such as biomass burning and CFPPs played a major role in NH_3 levels. This is particularly relevant during October and November, the study period when post-harvest residue burning was widespread across the region. Such burning activities have been shown to significantly elevate PM concentration over the area (Rastogi et al., 2016; Satish et al., 2020; Singh et al., 2016). Contribution of biomass burning to NH_3 emissions across India had been reported by previous studies (Behera et al., 2013; Tripathi et al., 2024). Moreover, the study site is located close to several major CFPPs, including Rajpura, Guru Gobind Singh, and Guru Hargobind thermal power plants. Emission of NH_3 from CFPPs are well documented in several existing studies. (Huang et al., 2018b; Shaw et al., 2024; Sun et al., 2017b; K. Zhang et al., 2022; Y. Zhang et al., 2020). In contrast, during the windier days vertical and horizontal mixing was enhanced thus diluting local emissions and increasing the influence of more dispersed, regional sources. During this time of year, which coincided with Rabi crop sowing and associated farming activities, agriculture becomes a more dominant source of NH_3 across the Indo-Gangetic Plain (T. Singh et al., 2021; Yadav et al., 2023). Unlike industrial or urban emissions, agricultural NH_3 emissions are spread across rural landscapes, making them more significant under conditions of strong atmospheric transport.

A significant negative correlation was observed between wind speed and δ^{15}N-NH_3 (Figure 4.3), suggesting that isotopically enriched sources contributed more significantly under calmer atmospheric conditions and vice versa. Emissions from combustion-related sources such as biomass burning (BB) and coal-fired power plants (CFPPs) tend to exhibit higher δ^{15}-NH_3 values, while agricultural sources are typically associated with relatively depleted δ^{15} signatures (T. Li et al., 2023; Pan et al., 2016, 2018; Xiao et al., 2024).

Therefore, the observed shift toward lower δ^{15}N-NH_3 values with increasing wind speed indicated a transition from local, combustion-dominated sources to a more widespread agricultural emission. This change in isotopic signature reflected the influence of regional NH_3sources under elevated atmospheric mixing conditions.

A relatively weaker negative correlation was observed between wind speed and δ^{15}N-NH_4^+ (Figure 4.3). This was due to the fact that δ^{15}N-NH_4^+ reflected not only the isotopic signature of its precursor gas NH_3 but also the fractionation that occur during the gas-particle partitioning. This partitioning is governed by a range of factors, including local meteorological conditions and complex atmospheric chemical interactions. A more detailed discussion on these influencing factors is presented in the later chapters

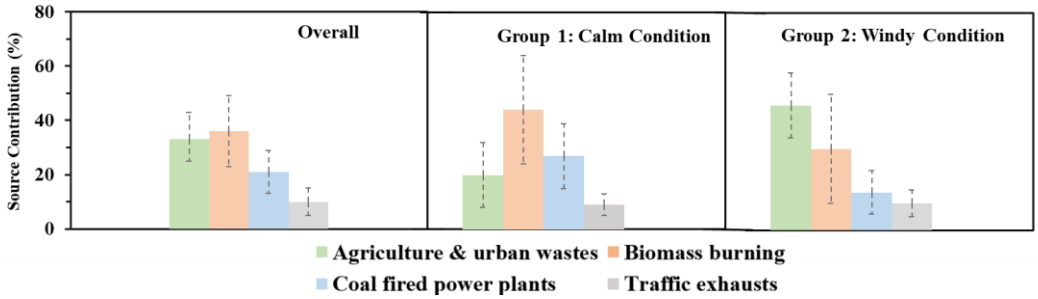

Figure 4.2. Source contribution during post-monsoon over Patiala

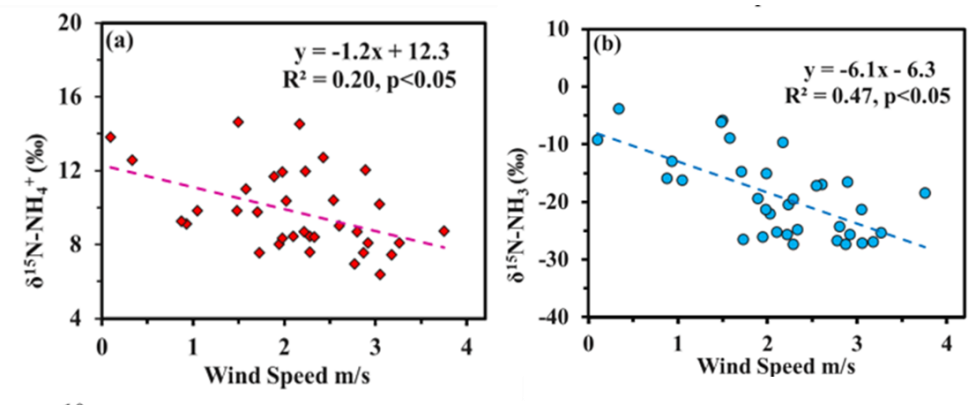

Figure 4.3. Correlation between windspeed and (a) δ^{15}N-NH_4^+ (b) δ^{15}N-NH_3 over Patiala during post-monsoon

Source apportionment results suggested that during winter NH_3 slip was the dominant source contributing around 47 ± 24% of the total NH_3 in Patiala. This is followed by agriculture and urban wastes emissions, which accounts for nearly 24 ± 11% of NH_3 emissions. Emission from traffic exhausts and biomass burning accounted

for 19 ± 14 %, and 10 ± 8 % respectively. Contributions of different sources were similar for day and night-time samples with no statistically significant difference (Shaw et al., 2024).

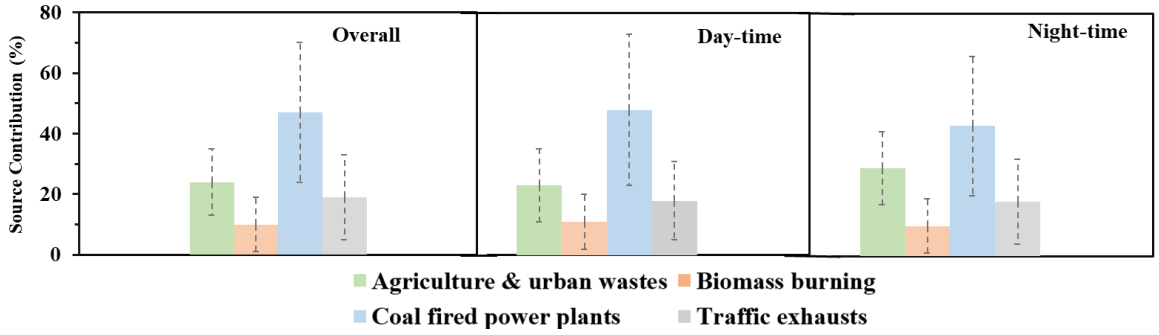

Figure 4.4. Source Contribution during winter over Patiala

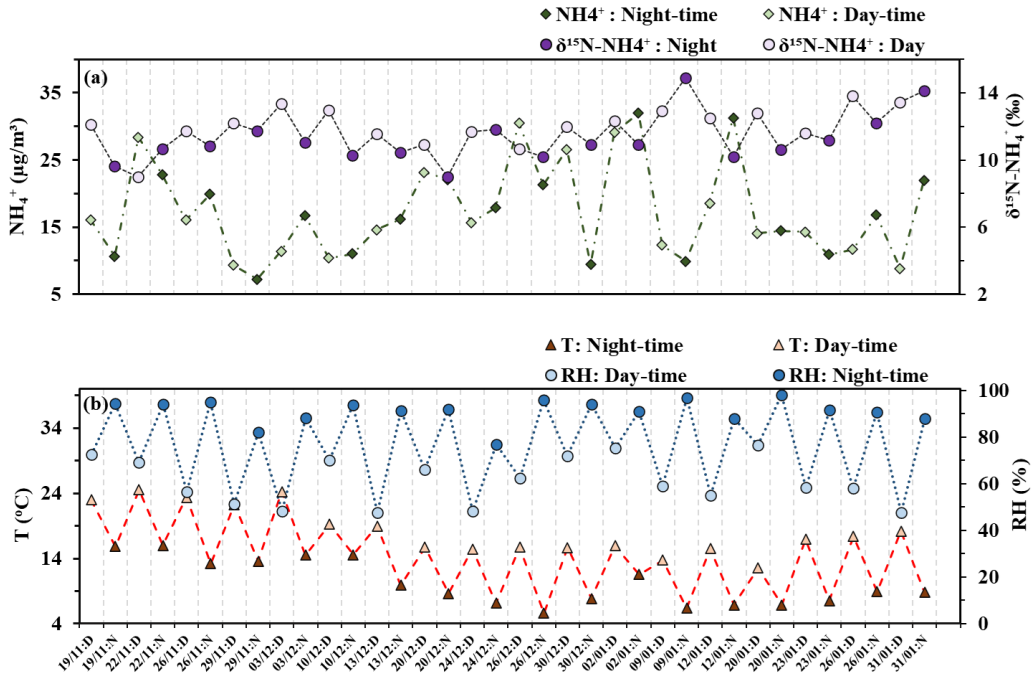

Figure 4.5. Time series of (a) $\delta^{15}N\text{-}NH_4^+$ and NH_4^+concentration (b) RH and T over Patiala during winter

The high contribution from NH_3 slip can be attributed to the presence of several large CFPPs in and around Patiala. These include the Rajpura Thermal Power Plant (1400 MW), Guru Gobind Singh Super Thermal Plant in Ropar (1260 MW), Guru Hargobind Thermal Plant (920 MW), and Guru Nanak Dev Thermal Plant in Bathinda (460 MW). In addition to these, vehicles equipped with Selective Catalytic Reduction

(SCR) systems can also contribute to NH_3 emissions. As mandated under the Bharat Stage emission norms in India, SCR technology is now standard in many vehicles to reduce NO_x emissions, which can inadvertently release NH_3 as a by-product (Dey & Mehta, 2020). Studies have highlighted that although SCR systems are effective at lowering NOx levels, they can simultaneously increase atmospheric NH_3 concentrations (Liu et al., 2021). Recent studies also suggest the importance of non-agricultural emissions like SCR-equipped CFPPs are important sources for urban NH_3 in atmosphere (Huang et al., 2018; Sun et al., 2017; Zhang et al., 2020; Zhang et al., 2022). Agricultural NH_3 emissions were relatively lower during the winter, aligning with earlier studies that associate reduced NH_3 levels in this season with increased wet deposition during the monsoon, lower ambient temperatures, and limited soil moisture during the rabi cropping period (Kulshrestha et al., 2005; Kuttippurath et al., 2020; Warner et al., 2016). Contributions from biomass burning were minimal and highly variable, consistent with its episodic nature in the region. These events are typically concentrated in pre-monsoon and post-monsoon months (September–November and May) rather than winter (Rastogi et al., 2016).

4.3 Sources of NH_3 and NH_4^+ over an urban megacity (Delhi)

The average NH_4^+ concentration over Delhi was 13.2 ± 6.3 μg/m³ and contributed around 72% to WSIN. While the overall calculated δ^{15}N-NH_3 was around -11 ± 4‰, a significant lower value of -19 ± 2 ‰ of NH_3 and 8 ± 1‰ of NH_4^+ was observed in a few (6 samples) coinciding around the last week of October. Since variations in δ^{15}N-NH_3 is attributed to sources, source apportionment was done separately for the 2 groups. Group 1 with average δ^{15}N-NH_3 and δ^{15}N-NH_4^+ around -19 ± 2‰ and 8 ± 1‰; group 2 with the average δ^{15}N of NH_3 and NH_4^+ around -11± 3‰ and 12 ± 3‰ respectively.

Source apportionment over Delhi showed that overall contribution from biomass burning was highest (33 ± 19%), followed by traffic emissions (28 ± 13%), agriculture and urban wastes (24 ± 10%), and CFPPs (15 ± 12%) (Figure 4.5). This distribution reflects the typical urban atmospheric mix during the post-monsoon and

winter seasons, influenced by both regional biomass burning and persistent urban combustion sources.

To better understand temporal variation in source signatures, the dataset was divided into two groups based on $\delta^{15}N\text{-}NH_3$ values. Group 1, comprising samples from the last week of October, with a significantly lower $\delta^{15}N\text{-}NH_3$ and $\delta^{15}N\text{-}NH_4^+$, whereas Group 2 included the rest of the samples with a comparatively higher value for $\delta^{15}N\text{-}NH_3$ and $\delta^{15}N\text{-}NH_4^+$. Group 1 showed significantly higher contributions from agriculture and urban wastes (55 ± 9%), which was followed by lower input from biomass burning (20 ± 9%), traffic (16± 6%), and CFPPs (9± 6%) (Figure 4.6). The higher contribution from agricultural emission during October could be related to emission during Kharif crop harvesting activities which happens extensively in surrounding upwind regions like Punjab, Haryana. Significant agricultural emission of NH_3 was also observed over Patiala around similar time as mentioned in the previous section. Emission of NH_3 from agricultural activities during post monsoon over IGP have been well documented in previous studies (Kuttippurath et al., 2020b; T. Singh et al., 2021). However, it should be noted that agricultural emissions here included not only emission from fertilizer but also from livestock and urban wastes. Delineating these sources are difficult based on $\delta^{15}N\text{-}NH_3$ due to values being overlapping. In contrast, Group 2, which includes samples from November through February, was marked by a clear shift in source contributions. Here, biomass burning (34 ± 20%) and traffic exhaust (29 ± 18%) dominated followed by agricultural and urban waste sources (21 ± 10%) and CFPPs (16 ± 15%). This shift is consistent with the onset of winter, when lower temperatures, increased heating needs across northern India contribute to enhanced NH_3 and $PM_{2.5}$ from combustion (Awasthi et al., 2024; Goel et al., 2021; S. Mishra et al., 2023; Sharma et al., 2019). Further, Delhi, as a major urban centre, has witnessed a steep rise in vehicular population over the years. In March 2001, the city recorded around 3.2 million vehicles for a population of 13.4 million, which is more than doubled to nearly 7 million vehicles by March 2013. Compared to other Indian megacities like Mumbai, Chennai, and Kolkata, Delhi has a notably higher number of privately owned cars (D. Mishra & Goyal, 2014). This rapid growth in traffic volume has made vehicular emissions a significant contributor to both PM levels NH_3 emissions, a trend similarly observed in other large metropolitan areas across the globe (Chang et al., 2016; Kotnala et al., 2020; V. Singh et al., 2020; Sun et al., 2017). Overall,

the temporal evolution from agriculture-dominated to combustion-dominated NH_3 sources in Delhi are result of changing regional emission dynamics and seasonal atmospheric processes, rather than local shifts in source intensity.

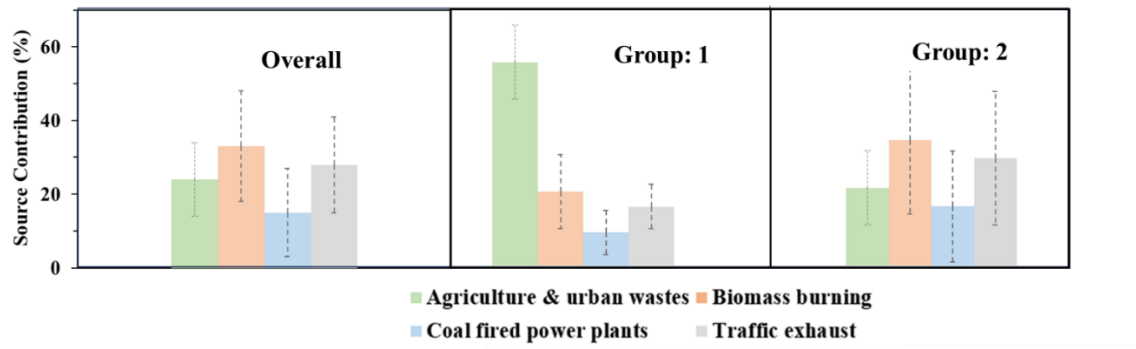

Figure 4.6. Source contributions over Delhi

4.4 Sources of NH_3 and NH_4^+ over Western India (Ahmedabad) during winter and summer

The average NH_4^+ concentration over Ahmedabad during winter and summer were 7.1 ± 3 µg/m³ and 1.7 ± 1 µg/m³, respectively. The water-soluble inorganic ion profile during summer and winter is given in Figure 4.7. The calculated δ^{15}N-NH_3 was -12.9 ± 4‰ in winter and -16.3 ± 2‰ in summer. Source apportionment by MixSIAR revealed that during winter, agriculture and urban wastes, biomass burning, CFPPs, and vehicular exhaust contributed approximately 30 ± 11%, 33 ± 14%, 15 ± 10%, and 22 ± 9%, respectively. In contrast, summer exhibited a dominant contribution from agriculture and urban wastes at 60 ± 10%, with biomass burning, CFPPs, and traffic emissions contributing 12 ± 8%, 10 ± 7%, and 18 ± 9%, respectively (Figure 4.7). The enhanced contribution of NH_3 from agriculture, livestock, and urban sources during summer can be primarily attributed to high ambient temperatures (average: 34 ± 4 °C), which increased the volatilization of NH_3 from N-based fertilizers, animal waste, and decomposing urban organic material.

Further, Ahmedabad, being among the leading milk-producing districts in India (Department of Animal Husbandry & Dairying, 2022), has a high density of livestock

activity, particularly in peri-urban areas, which intensifies NH_3 emissions from cattle sheds and manure storage. Direct effects of temperature in increasing volatilization of NH_3 from urban wastes, manures and farmland is well documented in existing studies (Sommer et al., 2019; Vira et al., 2020; C. Zhang et al., 2017). In contrast, during winter (average temperature: 22 ± 5 °C), volatilization from such sources is reduced, shifting more relative contribution towards combustion-related sources.

Biomass burning contributed around $15 \pm 10\%$ in winter, which might had arisen not only from local crop residue burning but also from regional transport of emissions from the surrounding semi-rural and suburban areas. Ahmedabad is located downwind of agricultural belts in Gujarat and Rajasthan, and the predominant northeast wind direction during winter facilitates the transport of biomass burning plumes into the city. Significant contributions from biomass burning to PM load and other gaseous pollutants over Ahmedabad have been reported in previous works (Bano et al., 2024; Chandra et al., 2016) Moreover, winter meteorology, characterized by shallow boundary layers and low dispersion, enhanced the accumulation of such pollutants. Traffic emissions remained a consistent source across both seasons, contributing $22 \pm 9\%$ and $18 \pm 9\%$ in winter and summer respectively. As a densely populated megacity with substantial traffic volume, Ahmedabad experiences continuous NH_3 and NO_x emissions from transportation, particularly from two-wheelers and heavy diesel vehicles. Previous studies have highlighted the contribution of traffic emissions to PM levels in Ahmedabad (Bano et al., 2024; Bhargava et al., 2016).

Overall, these patterns reflect a seasonal transition in NH_3 source dominance, governed by both temperature-driven volatilization processes and atmospheric transport dynamics. The winter season highlights the role of regional transport and persistent combustion sources, while summer is marked by intensified emissions from urban, livestock, and agricultural origins.

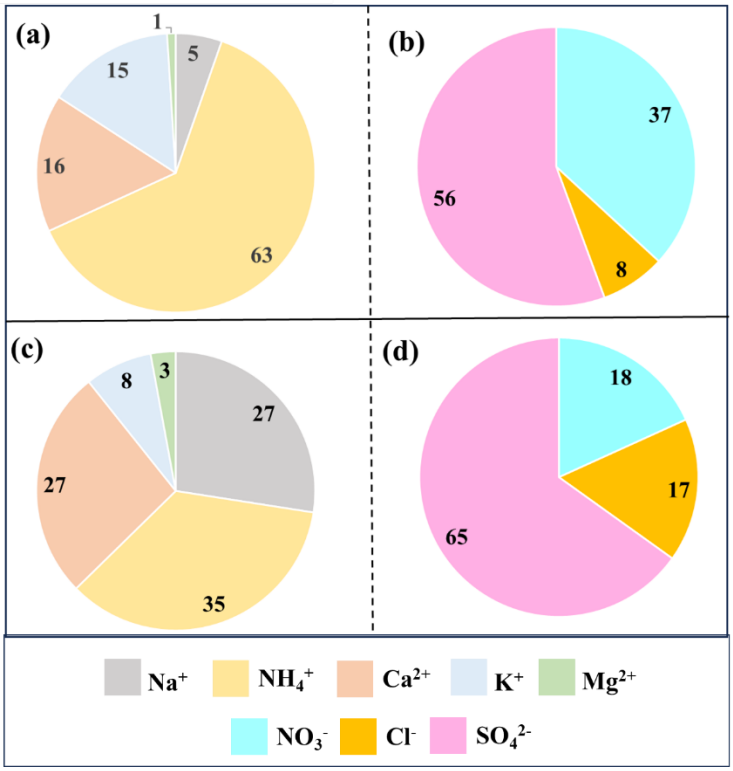

Figure 4.7. Water soluble inorganic ions during Winter (a) and (b) and Summer (c) and (d) over Ahmedabad. The numbers in the figure in in percentage.

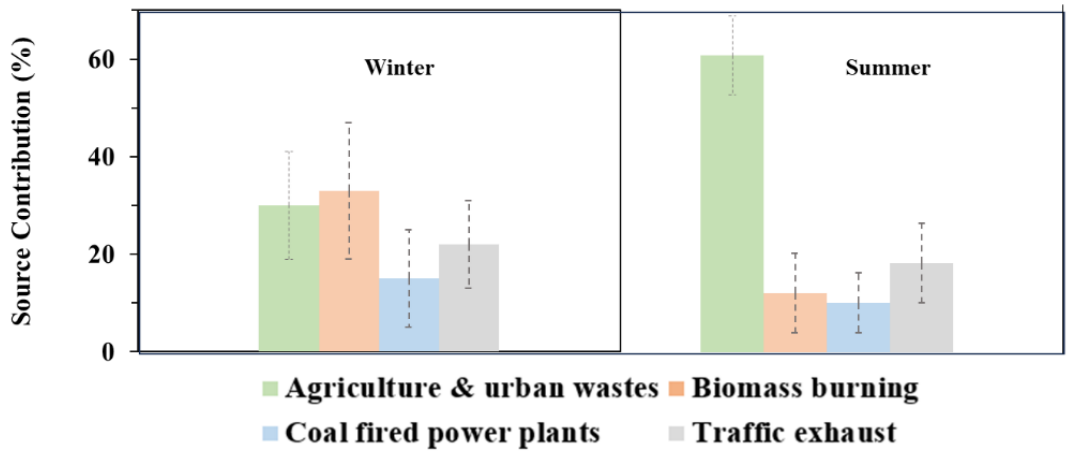

Figure 4.8. Source contributions over Ahmedabad during (a) Winter (b) Summer

4.5 Sources of NH_3 and NH_4^+ over North-eastern India (Dibrugarh and Shillong)

The average NH_4^+ concentrations over Dibrugarh were 1.5 ± 0.6 µg/m³ and 1.4 ± 0.6 µg/m³ for $PM_{2.5}$ and PM_{10} samples respectively, with no significant difference between them. At Shillong, average NH_4^+ concentration was around 3.7 ± 1.4 µg/m³, which was completely neutralised by SO_4^{2-}. NH_4^+ was the major contributor to water-soluble inorganic nitrogen (WSIN) at both the sites, accounting for approximately 95% and 98% of WSIN in Dibrugarh and Shillong (Figure 4.9).

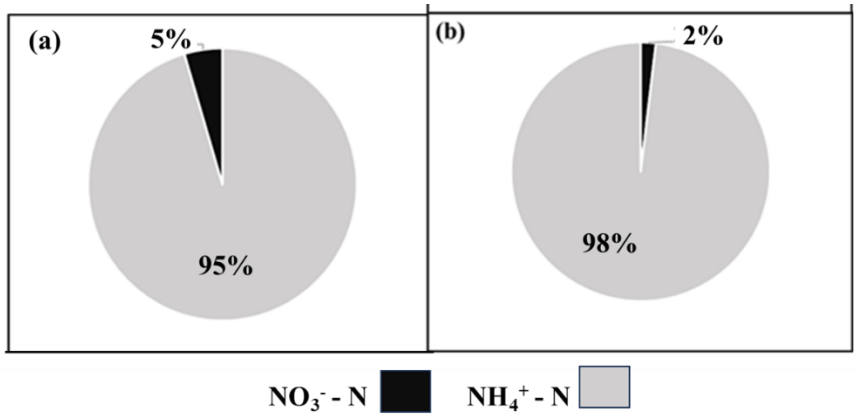

Figure 4.9. Contribution of between NH_4^+ and NO_3^- to WSIN in (a) Dibrugarh (b) Shillong

Calculated δ^{15}N-NH_3 over Dibrugarh were -17.5 ± 2.3‰ and -16.8 ± 2.5‰ for $PM_{2.5}$ and PM_{10}, corresponding to f values of 0.15 ± 0.1 and 0.16 ± 0.1, respectively. At Shillong the corresponding f and δ^{15}N-NH_3 were 0.21 ± 0.1 and -16.02 ± 3.5‰ respectively. Since there were no significant differences in f values, δ^{15}N-NH_3, or δ^{15}N-NH_4^+ between $PM_{2.5}$ and PM_{10} samples, source apportionment for Dibrugarh was performed collectively for $PM_{2.5}$ and PM_{10}. Results from MixSIAR showed that overall agriculture and urban wastes emissions accounted for 56 ± 8%. This was followed by biomass burning (21 ± 14%), traffic exhausts (13 ± 7%), and CFPPs (10 ± 7%) over Dibrugarh. A similar pattern in source contribution was observed over Shillong, where

agriculture and urban wastes emissions accounted for 50 ± 9 %, followed by biomass burning at 24 ± 11 %, traffic exhaust at 14 ± 7 %, and CFPPs at 12 ± 6 % (Figure 4.10).

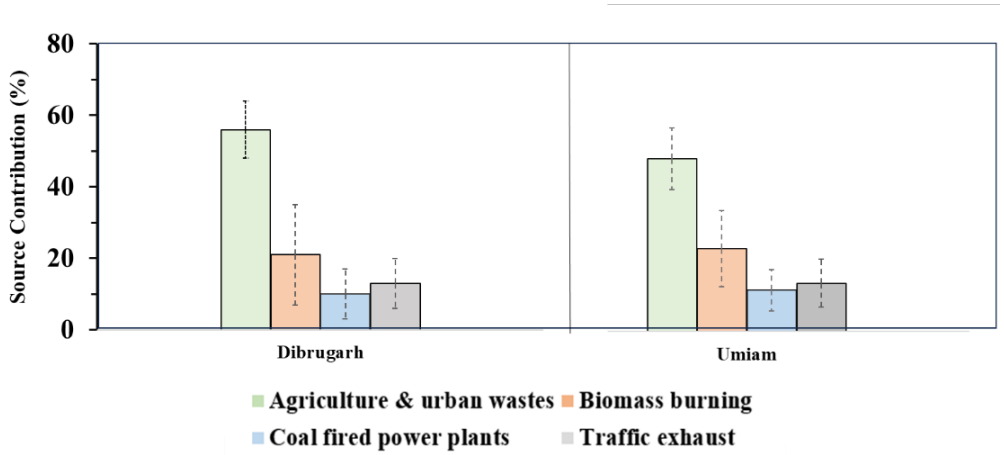

Figure 4.10. Source contribution over Dibrugarh and Shillong

During the sampling period (January to May), emission from agriculture and urban wastes were found to be the major contributors to atmospheric NH_3 concentrations over both Dibrugarh and Shillong. Dibrugarh, located in Assam's Upper Brahmaputra Valley, is predominantly rural, with 85 % of its land classified as rural area (Halder et al., 2023). More than 50 % of the district's geographical area is under cultivation, where agriculture and livestock rearing dominate the landscape. Further extensive use of nitrogen-rich fertilizers has been reported on this area, which are known for their high NH_3 volatilization, and thus contributing to NH3 emission. (Webb, 2001; Wyer et al., 2022). Furthermore, livestock rearing is common, and unmanaged manure stored near homesteads contributes continuously to NH3 emissions (Statistical Handbook Assam., 2024). Over Shillong, situated in the East Khasi Hills of Meghalaya, the terrain is hillier and more fragmented, but agriculture still plays a vital role, occupying approximately majority of the surrounding rural land (Government of Meghalaya, 2020). Here, traditional farming practices and the use of organic composts and livestock waste during early planting stages further enhance NH_3 (Choudhury et al., 2016; Handbook of Government of Meghalaya 2019).

In both regions, biomass burning also contributed significantly to NH_3 emissions, as indicated by source contributions. However, rather than large-scale open field burning, this contribution is more likely associated with household-level biomass burning, especially in rural and peri-urban areas where wood-fires, ire-wood crop

residues, and cow-dung cakes are widely used as fuel for cooking and heating. These types of indoor combustions could significantly contribute to particulate matter as well as NH3 emissions (Carter et al., 2024; Q. Li et al., 2016; Pikmann et al., 2024; Venkataraman et al., 2006). Further, NH_3 contribution from CFPPs and traffic emissions were comparatively less over both the locations during the sampling period. Coal-fired power plants are relatively scarce in Northeast India, neither Dibrugarh nor Shillong is located near any major operational thermal power station with significant NH_3 slip emissions. Similarly, being rural and semi-urban areas, Dibrugarh and Shillong faced relatively sparse contribution from vehicular emission. Despite geographical and agricultural intensity differences, both Dibrugarh and Shillong showed similar NH_3 source profiles, with agriculture, livestock, and indoor biomass burning being the dominant contributors, as supported by $\delta^{15}N\text{-}NH_4^+$ signatures and Bayesian mixing model outputs.

Chapter 5
Insights into the formation pathways and sources of particulate nitrate through dual isotopes

5.1 Introduction

NO_x serves as a major precursor to tropospheric ozone, a greenhouse gas and photochemical pollutant (Crutzen, 1970, 1979) and is ultimately oxidized to HNO_3, which partitions into the aerosol NO_3^-, contributing significantly to $PM_{2.5}$ loading (Seinfeld & Pandis, 2012; Driscoll et al., 2024). The formation of HNO_3 proceeds through multiple oxidation pathways involving OH radicals, N_2O_5 hydrolysis, and reactions with VOCs or halogens each modulated by atmospheric chemistry and meteorology, including temperature, RH, and boundary layer dynamics (Savarino et al., 2013; Walters & Michalski, 2016). Despite India being a major global hotspot for NO_x emissions, driven by vehicular emission, agriculture, and widespread biomass burning, large uncertainties persist in regional emission inventories due to the lack of observational constraints (Galloway et al., 2004; Ghude et al., 2012; Liu et al., 2024; Sahu et al., 2012). Dual isotopes ($\delta^{15}N$ and $\delta^{18}O$) of NO_3^- analysis offers a promising framework for simultaneously identifying NO_x sources and formation mechanisms (Michalski et al., 2012; Walters & Michalski, 2015).

This study applies the dual-isotope framework to two different regions of India. The first site, Patiala, is a semi-urban location in the northwestern Indo-Gangetic Plain, where sampling was conducted during the post-monsoon season dominated by large-scale agricultural residue burning. The second site, Ahmedabad, is a western Indian megacity where sampling was done in winter and summer. These contrasting locations, differing in source profiles, seasonality, and meteorological dynamics, offer a unique opportunity to assess how different factors like meteorology and sources factors shape the atmospheric processing of NO_x and the formation of NO_3^-.

The objectives of this chapter are to assesses formations pathways of NO_3^- and to quantify the major sources of NO_x (NO_3^- precursor) under different meteorological conditions, using dual isotope of NO_3^-. By integrating dual-isotope observations with chemical measurements and statistical modelling, this study seeks to reduce uncertainties in NO_x emission inventories and improve understanding of reactive nitrogen processing in diverse Indian environments.

5.2 Patiala

5.2.1 Variation in concentration and isotopic signature of NO_3^- over Patiala during post-monsoon

The average diurnal concentrations of NO_3^- over Patiala were 2.3 ± 2.2 μg/m^3 and 10.7 ± 5.1 μg/m^3, during day-time and night-time respectively, which were significantly different ($p<0.05$) (Table 5.1). A strong positive correlation ($p<0.05$) with a near unity slope was observed, between NO_3^- and sum of NVCs (K^+, Ca^{2+} and Mg^{2+}) (figure 5.1). Additionally, the NO_3^- was also present as NH_4NO_3 in samples with excess NH_4^+ (remaining after $(NH_4)_2SO_4$ formation), predominantly in night-time samples. The implications of this observation are discussed later. Further, NO_x and NO_2 concentration followed a similar trend to NO_3^- with a significantly higher concentration at night-time (NO_x: 66.9 ± 23 μg/m^3, and NO_2: 61.1 ± 15μg/m^3) than during day-time (NO_x: 46.7 ± 13 μg/m^3 and NO_2: 43.5 ± 11 μg/m^3). On average, NO_2 made up about 90% of total NO_x, with an average NO_2/ NO_x ratio (fNO_2) of 0.91 ± 0.1. This ratio did not differ significantly between day and night ($p > 0.05$). A significant positive correlation was observed between NO_2 and NO_3^- concentrations, while NO_3^- showed a significant negative correlation with temperature (figure 5.2).

Furthermore, Nitrate Oxidation Ratio (NOR), which indicates the fraction of NO_2 gas converted to NO_3^- calculated using eq.5.1. Overall, NOR was 0.09 ± 0.06, with the lower and higher values observed during day-time (0.03 ± 0.02) and night-time (0.12 ± 0.05), respectively. This suggested that a greater fraction of NO_2 gas was converted to NO_3^- during night-time, likely driven by a cooler temperature (Jiang et al.,

2019; Zang et al., 2022). This observation indicated that NO_3^- formation not only depends upon the availability of precursors but also by ambient conditions.

$$NOR = \frac{pNO_3^-}{pNO_3^- + NO_2} \qquad \text{eq. 5.1}$$

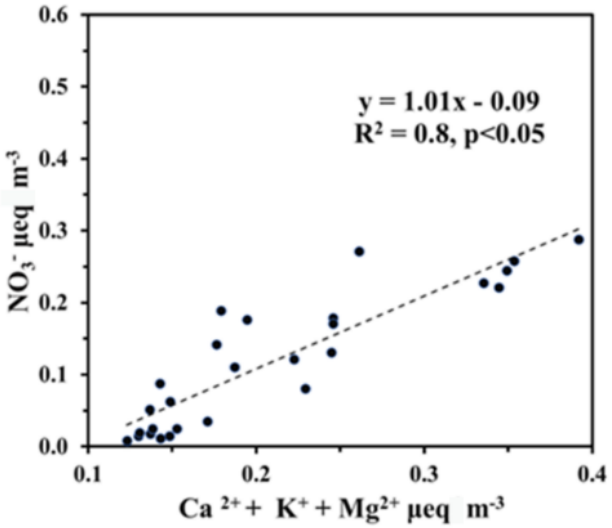

Figure 5.1.Correlation between NO_3^- with NVCs (sum of Ca^{2+}, K^+, Mg^{2+}) over Patiala during post-monsoon (concentrations in equivalent unit)

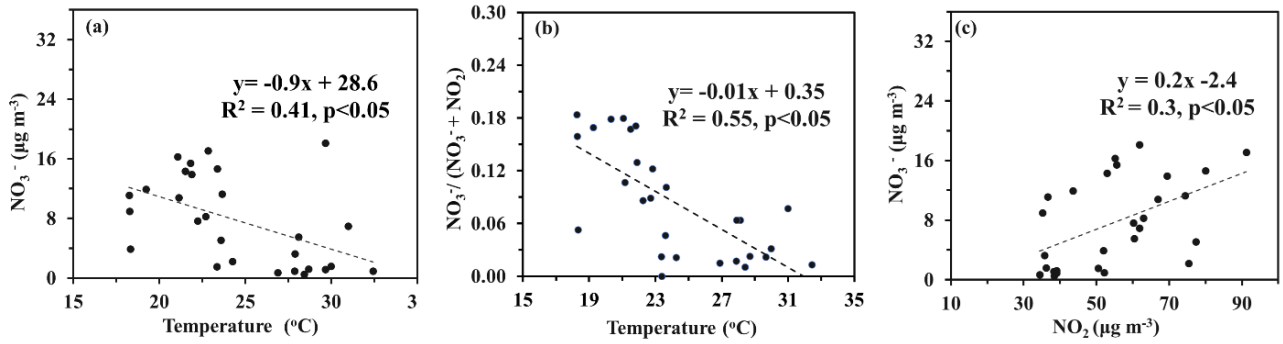

Figure 5.2. Relationship of temperature with (a) NO_3^-, (b) NOR, and (c) between NO_3^- and NO_2

Table 5.1. Comparison of present study with existing studies from literature

Site	Duration	Season	NO_3^-(ug m^{-3})	NO_2 (ug m^{-3})	NO (ug m^{-3})	$\delta^{15}N\text{-}NO_3^-$ (‰)	$\delta^{18}O\text{-}NO_3^-$ (‰)	Refferences
			Species					
Patiala	Day-time	Autumn (Oct-Nov)	2.3 ± 2.2	43.5 ± 10.5	3.2 ± 2.4	-5.0 ± 2.4	52.1 ± 6.2	Present study
	Night-time		10.7 ± 5.1	61.1 ± 15.2	5.8 ± 9.4	-0.13 ± 5.7	60.0 ± 8.4	
	Overall		7.7 ± 5.9	54.8 ± 15.9	4.8 ± 7.7	-1.9 ± 5.3	57.2 ± 8.5	
Shanghai	24-48 hrs	Winter (Nov-Dec)	15.1 ± 10.0			3.7 ± 3.8	80.1 ± 9.9	Zhu et al., 2021
		Summer(Aug-Sept)	5.0 ± 1.6			0.7 ± 3.2	62.1 ± 12.8	
Beijing	Day-time	Winter(Nov-Dec)	12.2 ± 18.3	51.3 ± 28.7		12.4 ± 5.1	81.1 ± 16.6	Fan et al., 2020
	Night-time		11.5 ± 15.1	66.7 ± 24.8		10.4 ± 4.7	85.6 ± 10.2	
	Overall		11.8 ± 16.7	58.9 ± 27.8		11.5 ± 5.0	83.8 ± 13.4	
Guiyang	morning, noon, afternoon	Winter(Dec-Jan)	10.4 ± 5.5, 9.3 ± 6.5, 8.7 ± 5.6			5.0 ± 2.6	79.0 ± 11.0	Li et al., 2021
	morning, noon, afternoon	Summer(Aug-Sept)	0.9 ± 0.3, 0.2 ± 0.1, 0.8 ± 1.5			−1.8 ± 3.5	56.1 ± 7.4	
Mt. Tai	Day-time	Spring (March- April)	*14.9 ± 9.1			1.8 ± 2.4	78.5 ± 4.5	Wu et al., 2021
	Night-time		*11.8 ± 7.4			1.4 ± 3.6	81.1 ± 4.1	
Hangzhou	24 hours	Year round	14.7 ± 12.0			5.9 ± 2.7 6	69.5 ± 17.7	Jin et al., 2020
Beijing	24 hours	Year round	8.5 ± 10.9	52.6 ± 24.3		7.3 ± 5.4		Song et al.,2019
Qingdao City	24 hours	Winter (Dec-Feb)	25.4 ± 22.8			9.5 ± 3.3	97.2 ± 6.3	Ni et al., 2024
		Summer (June-Aug)	9.0 ± 5.7			− 1.1 ± 2.2	73.3 ± 6.3	
Beijing-Tianjin-Hebei	24 hours	Year round	15.6± 13.6			-6.1 to 18.2	52.2 to 103.8	Dong et al., 2022
Nanchang	~ 24 hours	Autumn-Winter(Sept-Dec)	14.7 ± 11.6	41.5 ± 23.5		4.3 ± 4.3	71.8 ± 14.7	Xiao et al., 2020

* Calculated from NO_3^--N concentration

The isotopic composition of NO_3^- offered deeper insight into the diurnal variability of its formation processes. The overall $\delta^{15}N\text{-}NO_3^-$ was –1.9 ± 5‰, with significantly lower values during the day-time (–5.0 ± 2‰) compared to night-time (–0.13 ± 6‰) (Table 1; $p < 0.05$). A similar range of $\delta^{15}N\text{-}NO_3^-$ are also reported in existing studies over other urban regions across globe (Dong et al., 2022; Q. Li et al., 2021; Ni et al., 2024). The observed diurnal variability in $\delta^{15}N\text{-}NO_3^-$ could be attributed to multiple factors, like variability in NO_x source contributions, shifts in the formation pathways, impact of meteorology on gas-particle partitioning, availability of other cations, or a combination of all these factors. It is important to note that $\delta^{15}N\text{-}NO_3^-$ was influenced not only by the sources of the precursor gas but also by the NO_3^-formation pathways. As outlined in the preceding section, the elevated concentration of NO_3^- during night-time suggested that gas-to-particle partitioning was more favourable under cooler conditions, which could lead to a higher $\delta^{15}N\text{- }NO_3^-$ value during night-time (Q. Li et al., 2021; Walters & Michalski, 2015).

In parallel, $\delta^{18}O\text{-}NO_3^-$ values also showed distinct temporal variation, with an overall mean of 57.2 ± 8.5‰. Significantly higher values of $\delta^{18}O\text{-}NO_3^-$ were observed at night (60.0 ± 8 ‰) compared to daytime (52.1 ± 6‰) ($p < 0.05$), indicating to differences in its formation pathways. Day-time formation is primarily driven by oxidation of NO_2, by OH while during night-time, alternative pathways involving NO_3 and N_2O_5 become prevalent due to the absence of photochemically generated OH radicals, (Walters & Michalski, 2015, 2016). Details of the different pathways of NO_3^-

formation from precursors, and the influence of pathway contributions to $\delta^{18}O\text{-}NO_3^-$ and $\delta^{15}N\text{-}NO_3^-$ is discussed in the next sections.

5.2.2 Formation pathways of NO_3^-

The estimated $\delta^{18}O\text{-}NO_3^-$ formed via P_1, P_{2a}, P_{2b}, P_3 and P_4 pathways were 57 ± 5‰, 99 ± 6‰, 100 ± 6‰, 109 ± 7‰, and 127 ± 7‰, respectively. Since the $\delta^{18}O\text{-}NO_3^-$ via P_{2a} and P_{2b} were very close, they were merged as P_2 i.e., it included both the formation pathways of NO_3^- [via $N_2O_5(H_2O)$ and $N_2O_5(Cl^-)$]. The trend in calculated $\delta^{18}O\text{-}NO_3^-$ values from the different pathways in this study, was consistent to what was reported by Luo et al. 2020, where the lowest $\delta^{18}O\text{-}NO_3^-$ was associated with P_1, followed by P_2 and P_3, while P_4 showed the highest $\delta^{18}O\text{-}NO_3^-$ values. A similar pattern was also reported by Song et al. 2022. The overall estimated contributions from each pathway showed that P_1 and P_2 were dominant, accounting for 79.6 ± 7% and 16.1 ± 8% of total NO_3^- formation, respectively. The contributions from P_3 and P_4 were minimal, at 1.7 ± 3% and 2.6 ± 3%, respectively. During the day-time, the relative contributions from P_1, P_2, P_3, and P_4 were 91.5 ± 2%, 6.7 ± 6%, 1.0 ± 1%, and 0.7 ± 2%, respectively. In contrast, during the night-time, contributions shifted to 74.8 ± 7% for P_1, 21.8 ± 9% for P_2, 1.8 ± 4 % for P_3, and 1.4 ± 4% for P_4 (Figure 5.3).

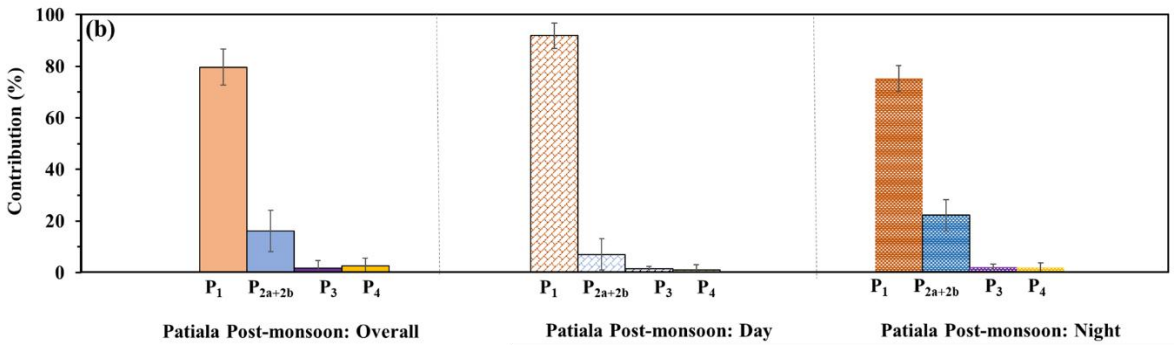

Figure 5.3. Overall and diurnal contributions of the four pathways during the sampling period

As the contributions from P_3 and P_4 were negligible, only two major pathways (P_1 and P_2) were further considered for source apportionment. Diurnal variability in pathway contributions from P_1 and P_2 were also calculated for individual samples. Details about the calculation involved can be found in Chapter 2. The NO_3^- formed via P_1 ranged from 82% to 98% (average: 94.4 ± 6 %) and via P_2 from 2% to 18% (average:

5.6 ± 6%) during day-time, whereas, P1 ranged 50% to 95% (average: 75.4 ± 14%) and P2 from 5% to 50% (average: 24.6 ± 14%) during night-time. Overall NO_3^- formed by P_1 dominated throughout the study period. Predominant contributions by OH-pathway, followed by N_2O_5 pathway, and negligible contribution by VOCs pathways was also reported during autumn by Xiao et al. (2020). During day-time, the presence of sunlight facilitated the formation of NO_3^- via the reaction of NO_2 with photochemically produced OH (P_1). During night-time, in the absence of photochemically produced OH radicals, NO_2 reacts with O_3 to form higher oxide of nitrogen like N_2O_5. However, N_2O_5 being thermally unstable with a shorter life-time could rapidly decompose back to NO_3 and NO_2 (Freyer et al., 1991; Walters & Michalski, 2016; Xiao et al., 2020). Furthermore, the life-time of NO_3^- in the lower troposphere is of the order of few days to few weeks which is much longer than the average sampling duration of 8-12 hours. The combination of temperature sensitivity of N_2O_5 and the presence of stable residual pNO_3^- could explain why NO_3^- formed via P_1 was higher as compared to that formed via P_2 even during night-time.

5.2.3 Factors affecting the formation pathways of NO_3^-

5.2.3.1 Boundary layer dynamics

A variation in planetary boundary layer (PBL) could significantly influence the diurnal variation in observed $\delta^{15}N\text{-}NO_3^-$. The average PBL heights during day-time and night-time were 592 ± 138 m and 217 ± 39 m, respectively. This diurnal difference was statistically significant ($p < 0.05$, t-test) and coincided with the observed trend in $\delta^{15}N\text{-}NO_3^-$, which showed significant higher values at night compared to the day. Similar diurnal trend in $\delta^{15}N\text{-}NO_3^-$, had been reported in earlier studies (Albertin et al., 2024; Vicars et al., 2013). During the day-time, elevated temperatures lead to a well-mixed and deeper boundary layer, which diluted surface level NO_x as well as NO_3^- concentrations due to greater vertical dispersion. This was consistent with the lower NO_x and NO_3^- concentrations recorded during the day-time.

Conversely, night-time conditions were marked by a shallow and stable boundary layer, limiting vertical mixing. This likely led to the accumulation of NO_3^- near the surface, which included both freshly formed and residual particles. Therefore,

the higher contribution from the P_1 pathway observed at night did not necessarily mean active nocturnal formation, but rather the presence of daytime-formed NO_3^- that persisted due to limited atmospheric dispersion. The influence of boundary layer dynamics on the isotopic signature of NO_3^- had also been reported by (Fan et al., 2022) who reported isotopically depleted NO_3^- under high, well-mixed boundary layers and enriched NO_3^- under shallow, stable night-time conditions.

5.2.3.2 Meteorology and chemical stability

A cooler temperature with a RH favoured the gas-particle partitioning towards the particulate phase, thus stabilizing and retaining NO_3^- in the atmosphere during night hours. However, the P_2 pathway is highly sensitive to temperature due to the thermal instability of N_2O_5. This was evident in Figure 5.4, where contributions from P_2 increased during lower temperature, further reflecting the effect of temperature. However, its contribution remained secondary and highly variable compared to the more robust and consistent behaviour of the OH pathway. While it's difficult to elucidate the effect of boundary layer or meteorology alone on the $\delta^{15}N\text{-}NO_3^-$, it was likely to be influenced by a combination of all the factors like formation pathway of NO_3^-, the temperature affected gas-particle partitioning and boundary layer dynamics with a complex interplay between them.

A significantly high (>70%) contribution of NO_2 + OH pathways to NO_3^- formation in different seasons, had also been documented in existing studies like China at latitude 22-23^{o}N (Guo et al., 2021; Chen et al.; 2022; Xi et 2023). These conditions favour the formations of OH radical and enhance the thermal instability of N_2O_5, thus resulting into higher NO_3^- formation via OH pathway (Li et al., 2018; Luo et al., 2021; Ma et al., 2019; Sofen et al., 2014; Wang et al., 2018). Moreover, the dominance of the OH pathway is consistent with global estimates of NO_3^- formation based on $\Delta^{17}O$ isotopic signatures (Alexander et al., 2009). A recent study over the IGP reported high HONO concentrations (a key precursor to OH radicals) during fog episodes characterized by high RH (~80%) and low temperatures (~10–15 °C); whereas, comparatively lower concentration of the precursor was observed at lower RH and relatively higher temperature (Pawar et al. 2024), which indicated enhanced formation of OH radicals. In the present study, the sampling time was post-monsoon with average RH and T as 48 % and 63 %, and 29 °C and 22 °C during day-time and night-time,

respectively. These atmospheric conditions were not conducive for suppressing OH formation.

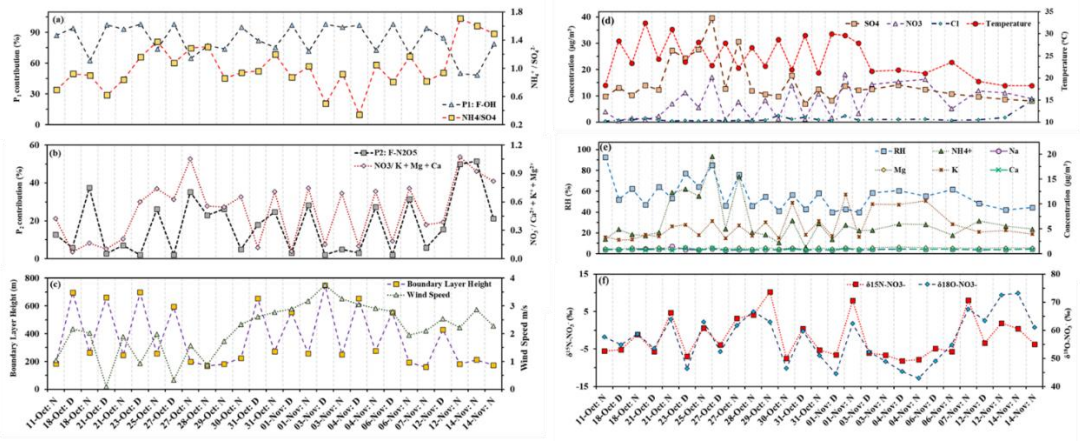

Figure 5.4. Time series of (a) P_1 (OH) contribution and NH_4^{+}/SO_4^{2-} equivalent ratio. (b) P_2 (N_2O_5) contribution and $NO_3^-/K^+ + Ca^{2+} + Mg^{2+}$ equivalent ratio. (c) Boundary layer height (BLH) and wind speed. (d) Anion concentrations (SO_4^{2-}, NO_3^-, Cl^-) and temperature. (e) RH and cation concentrations (NH_4^+, K^+, Ca^{2+}, Mg^{2+}, Na^+) (f) $\delta^{15}N\text{-}NO_3^-$ and $\delta^{18}N\text{-}NO_3^-$. D and N refer to day-time and night-time respectively.

Theoretical calculations by Walters & Michalski (2016) showed the effect of temperature on the isotopic signature of NO_3^-. The fractionation between H_2O and OH ($^{18}\alpha_{OH/H2O}$) was found to increase with a decrease in temperature, therefore a lower temperature should result in a lower $\delta^{18}O\text{-}NO_3^-$ via P_1. This effect is seen in P_1 since the fractionation between OH and H_2O occur during P_1 (Walters & Michalski, 2015, 2016). In the current study, NO_3^- formed via P_1 was dominant during both day-time and night-time. In spite of lower night-time temperature, an elevated $\delta^{18}O\text{-}NO_3^-$ was observed. This suggested that the NO_3^- collected at night likely included residuals that were formed during the day. On the other hand, as expected, the formation of NO_3^- via the N_2O_5 pathway (P_2) was significantly higher during the night-time as compared to day-time.

It was also observed that samples with a relatively lower contribution from P_1, and thus a higher contribution from P_2, had higher NH_4^+/SO_4^{2-} and $NO_3^-/(Ca^{2+} + K^+ + Mg^{2+})$ ratio (Figure 5.5). The majority of these were night-time samples. This indicated that when excess NH_4^+ was present (beyond what was needed to neutralize SO_4^{2-}), NO_3^- tended to form NH_4NO_3. However, the NH_4NO_3 being semi volatile, was stable under cooler night-time conditions but became unstable during the day-time. In contrast, NO_3^- which formed stable compound with non-volatile cations (Ca^{2+}, K^+ and

Mg^{2+}) persisted as residual NO_3^-. This further explained the relatively lower contribution of P_2 during day-time and relatively higher contribution of P_1 as compared to P_2 during night-time even if there was residual NO_3^- in both the cases.

A significant positive correlation between $\delta^{15}N\text{-}NO_3^-$ and $\delta^{18}O\text{-}NO_3^-$ was observed (Figure 5.5). Xiao et al. (2020) reported a similar relationship and attributed it to the dominance of two main oxidation pathways (OH and N_2O_5). This further supports what was considered for diurnal pathway contributions and source apportionment in this study. A similar pattern was also reported by Walters and Michalski (2016), where they compared observed $\delta^{15}N\text{-}NO_3^-$ and $\delta^{18}O\text{-}NO_3^-$ values from existing literature with those predicted by an equilibrium model. Their model, which estimated isotopic end-members for NO_3^- formed via OH and N_2O_5, and predicted an increase in $\delta^{18}O$ with an increase in $\delta^{15}N$ of NO_3^-. A similar trend was also observed in the present study, which could be attributed to the relatively higher contribution of P_2 to NO_3^- formation during night-time compared to day-time.

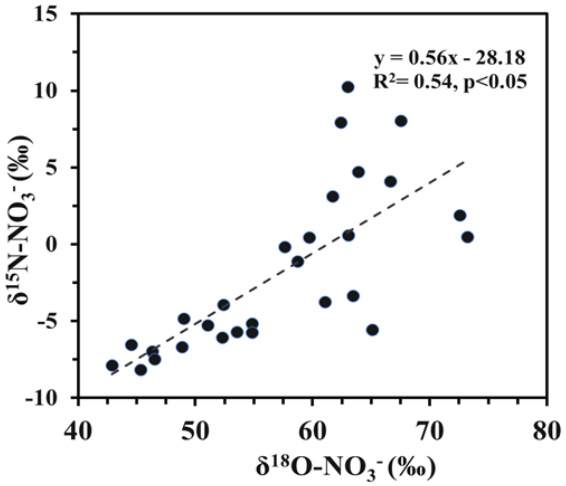

Figure 5.5. Relationship between $\delta^{15}N\text{-}NO_3^-$ and $\delta^{18}O\text{-}NO_3^-$

5.2.4 Major sources of NO_x thus NO_3^- over Patiala during post monsoon

Considering P_1 and P_2 to be the only major pathways and that thermodynamic equilibrium was achieved during the conversion of NO_2 to HNO_3, diurnal source apportionment of NO_x was carried out using MixSIAR based on the source data stated in Chapter 2. On average, traffic emissions, biomass burning, CFPPs, and soil emissions contributed about 38 ± 18%, 29 ± 18%, 20 ± 11%, and 13 ± 9%, respectively, to the

total NO_x emission. During the day-time, their respective contributions were approximately 46 ± 17%, 28 ± 16%, 16 ± 9%, and 10 ± 8%, while at night, they were about 32 ± 19%, 36 ± 23%, 19 ± 15%, and 13 ± 11%, without any significant diurnal differences ($p > 0.05$, t-test; Figure 5.6).

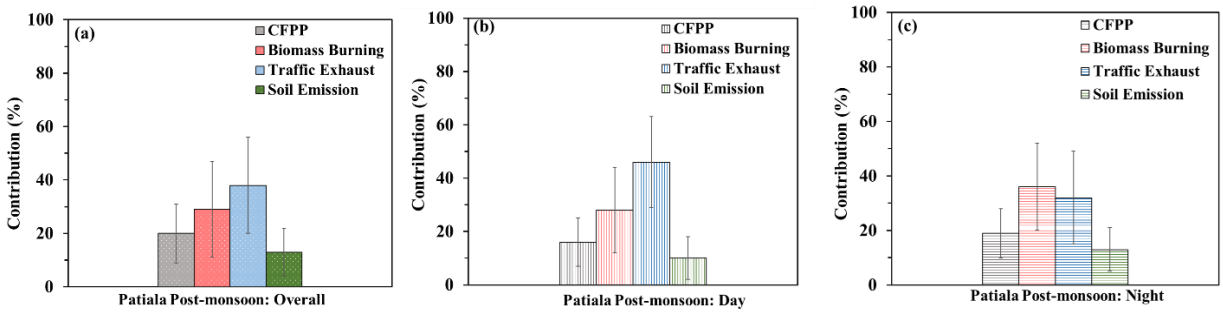

Figure 5.6. Overall (a) day-time (b) and night-time(c) source contributions of NO_x over Patiala during post-monsoon

Traffic emissions have previously been shown to be a significant contributor to the particulate matter and NO_2 in Patiala across both burning and non-burning periods (Singh et al., 2010; Singh et al., 2016). Similar findings have been reported for other cities in the IGP, such as Delhi, where factors like vehicle age, fuel type, and engine efficiency strongly influence NO_x levels (Goel et al., 2015; Lalchandani et al., 2021; Puthussery et al., 2022; Singh et al., 2021). The sampling period coincided with widespread post-harvest crop residue burning, a seasonal activity that occurs annually across the IGP, including Patiala. Biomass burning has been widely recognized as a major contributor to particulate matter and NO_x levels over Patiala, by several previous studies (Bikkina et al., 2019; Devaprasad et al., 2023; Rajput et al., 2014; Saud et al., 2011). During these burning events, high temperatures during the flaming phase can produce NO_x via Zeldovich mechanism (Walters et al., 2015; Zeldovich & Sunyaev, 1992). In contrast, lower-oxygen conditions in the smouldering phase can release gases like NH_3, which can later convert to NO_x. A higher $\delta^{15}N\text{-}NO_x$ value, similar to that

typically associated with biomass burning, was observed during the burning period in this study (Figure 5.7), indicating a strong influence from biomass burning.

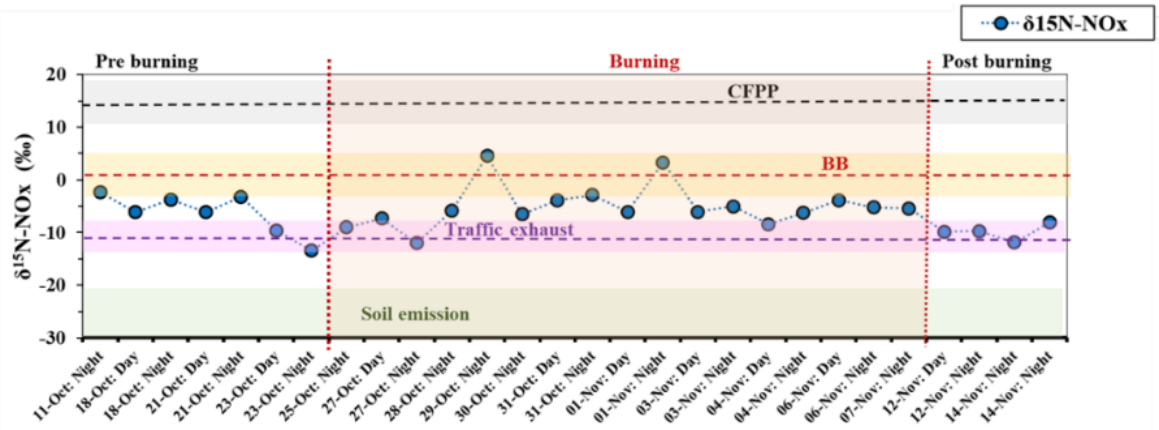

Figure 5.7. Variation of δ^{15}N-NO_x over Patiala during post-monsoon

The contribution of NO_x from CFPPs could be attributed to Patiala's proximity to several major thermal plants, including Rajpura Thermal Power Plant (1400 MW), Guru Gobind Singh Super Thermal Power Plant in Ropar (1260 MW), and Guru Hargobind Thermal Plant near National Highway 7. Previous work has shown that these plants can also emit significant amounts of NH_3 (Shaw et al., 2024). Although most CFPPs are fitted with SCR systems to control emissions, earlier studies have reported that both SCR-equipped and non-equipped plants can still release considerable amounts of NO_x (Felix et al., 2012).

5.3 Ahmedabad

5.3.1 Concentration and isotopic signature of NO_3^- during winter and summer over Ahmedabad

The overall average NO_3- concentration over Ahmedabad during winter was 9.9 ± 6 μg/m^3, while day-time and night-time concentrations were 7.5 ± 5 μg/m^3 and 12.0 ± 6 μg/m^3 respectively, with a significant diurnal difference between day-time and night-time values. The NO_3^- was present in the form of semi-volatile NH_4NO_3 as well as stable forms with NVCs throughout the sampling period as evident from the Figure 3.13. During summer the overall average NO_3- was mostly associated with NVCs with an overall concentration of 1.9 ± 2 μg /m^3. Day-time and night-time NO_3^- concentration

during summer were 1.5 ± 1 μg/m^3 and 2.2 ± 2 μg/m^3, respectively, without any significant ($p>0.05$) diurnal variation.

Winter showed elevated fNO_2 values (0.8 ± 0.1) compared to summer (0.5 ± 0.1). This was expected, as the photochemical conditions during winter inherently favour the accumulation of NO_2 in the ambient atmosphere. In the lower troposphere, NO is oxidized to NO_2 via its reaction with O_3, the NO_2 is then photolyzed back to NO under sunlight, maintaining a photo stationary state (Crutzen, 1974, 1979). However, reduced solar insolation and shorter daylight hours in winter significantly lower the photolysis rate of NO_2, thereby suppressing the conversion of NO_2 back to NO. Furthermore, lower ambient temperatures shift the equilibrium of the NO towards of NO_2 formation, as this reaction is exothermic (Kleinman, 1994; Seinfeld et al., 1998). These combined effects lead to a greater fraction of NO_2 relative to total NO_x during winter. Overall $\delta^{15}N\text{-}NO_3^-$ and $\delta^{18}O\text{-}NO_3^-$ values were -4.0 ± 5‰ and 65.3 ± 7‰, respectively, during winter, with day-time and night-time values as -6.1 ± 4 ‰ and -2.1 ± 5 ‰ for $\delta^{15}N$, and 62.1 ± 6 ‰ and 68.5 ± 7 ‰ for $\delta^{18}O$. During the summer season, the average $\delta^{15}N\text{-}NO_3^-$ and $\delta^{18}O\text{-}NO_3^-$ were -1.4 ± 4‰ and 62.1 ± 4.6 ‰, with corresponding day-time and night-time values of -1.2 ± 4‰ and -1.5 ± 4 ‰ for $\delta^{15}N$, and 60.5 ± 5‰ and 63.1± 4‰ for $\delta^{18}O$. Similar values of $\delta^{15}N\text{-}NO_3^-$ and seasonal variations in $\delta^{18}O\text{-}NO_3^-$ is reported in several existing studies (Q. Li et al., 2021; Ni et al., 2024; Zhu et al., 2021).

Diurnal variations in both $\delta^{15}N\text{-}NO_3^-$ and $\delta^{18}O\text{-}NO_3^-$ were observed in winter, but not during summer season.. The seasonal contrast could be due to variations in source influence, atmospheric mixing conditions, and the physical state of nitrate. While $\delta^{18}O\text{-}NO_3^-$ is mainly governed by the formation pathways of NO_3^- from NO_x, $\delta^{15}N\text{-}NO_3^-$ is shaped by both emission sources and isotopic fractionation. The day-night difference in $\delta^{18}O\text{-}NO_3^-$ during winter is related to the formation pathways, which is discussed in detail in the following sections. During summer, the elevated boundary layer enhanced vertical mixing and reduced the variability in isotopic signatures between day and night. In addition, NO_3^- during this period was mostly associated with NVCs, which minimized day-time losses and contributed to the observed isotopic consistency. In contrast, during winter, the lower boundary layer restricted dispersion, and NO_3^- was mainly present in more volatile forms such as NH_4NO_3. This likely led to greater loss of NO_3^- during the elevated temperature, resulting in a distinct isotopic differences between day and night.

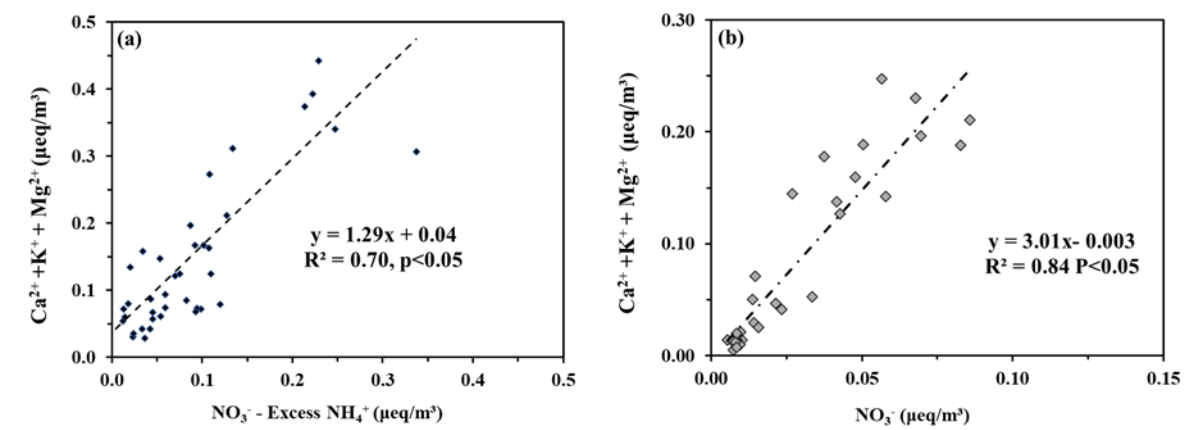

Figure 5.8. Association of NO_3^- with non-volatile cations over Ahmedabad during (a) Winter (b) Summer

5.3.2 Formation pathways of NO_3^- over Ahmedabad

During winter, the overall contributions of the NO_3^- formation pathways were as follows: P_1 (OH pathway): 61.9 ± 7%, P_2 (combined N_2O_5 hydrolysis, P_{2a+2b}): 24.6 ± 6%, P_3 (VOC pathway): 7.6 ± 4%, and P_4 ($ClONO_2$ pathway): 5.9 ± 3%. Compared to the OH and N_2O_5 driven pathways, the contributions from P_3 and P_4 remained relatively low and consistent. Notably, P_4's low influence was also consistent with the overall low Cl^- concentrations observed throughout the winter sampling period, limiting the availability of $ClONO_2$ for heterogeneous reactions. Diurnal differences were distinct, with P_1 contributing 69.4 ± 5% during the day-time and dropping to 52.3 ± 8% at night. In contrast, P_2 increased significantly from 17.6 ± 4.3% during the day to 32.8 ± 7% at night. The contributions of P_3 and P_4 remained minor across both periods, with P3 contributing 7.3 ± 4% during the day and 8.7 ± 3% at night, and P4 remaining relatively stable at 5.7 ± 3% and 6.2 ± 3%, respectively (Figure 5.9).

The relatively higher contribution of the OH pathway during day-time as compared to night-time was consistent with increased photochemical activity that facilitates the oxidation of NO_2 to HNO_3 and subsequently particulate NO_3^-. In contrast, the contribution from N_2O_5 hydrolysis (P_2) increased during the night, driven by the accumulation of NO_3 radicals in the absence of photolysis. Additionally, the thermal instability of N_2O_5 required cooler night-time temperatures, which created favourable conditions for its heterogeneous conversion on aerosol surfaces. While such diurnal patterns were also observed over Patiala during the post-monsoon season, the elevated night-time OH contribution in Patiala was likely driven by residual NO_3^- formed via

daytime OH oxidation, which was present in stable forms with NVCs as discussed in details in the previous sections. In comparison, although excess NO_3^- in Ahmedabad was also partly linked to NVCs, it predominantly existed in the form of (NH_4NO_3), which being a thermally unstable was susceptible to volatilization during the warmer hours. This difference in NO_3^- stability likely contributed to the more pronounced separation in formation pathways between day and night observed in Ahmedabad, the lower extent of vertical mixing in Ahmedabad compared to Patiala likely restricted the carryover of daytime-formed NO_3^- into the night-time, reducing the presence of residual OH-derived nitrate and amplifying the role of night-time chemistry.

During summer, NO_3^- formation was dominated by P_1, contributing 67.5 ± 7% overall, with similar contributions during the day (69.2 ± 7%) and night (65.2 ± 5%). P_2 contributed 25.3 ± 8%, while minor contributions came from P_3 (4.1 ± 3%) and P_4 (3.3 ± 2%), all showing no significant diurnal variation (figure 5.2). Similar lack of significant differences in pathways contributions during summer when compared to winter have also been reported by existing studies (M. Y. Fan et al., 2022; Zhang et al., 2022). This consistent pattern in pathway contributions aligned with the $\delta^{18}O\text{-}NO_3^-$ values measured across the day and night, likely due to enhanced vertical mixing and presence of NO3- with NVCs as stable compounds.

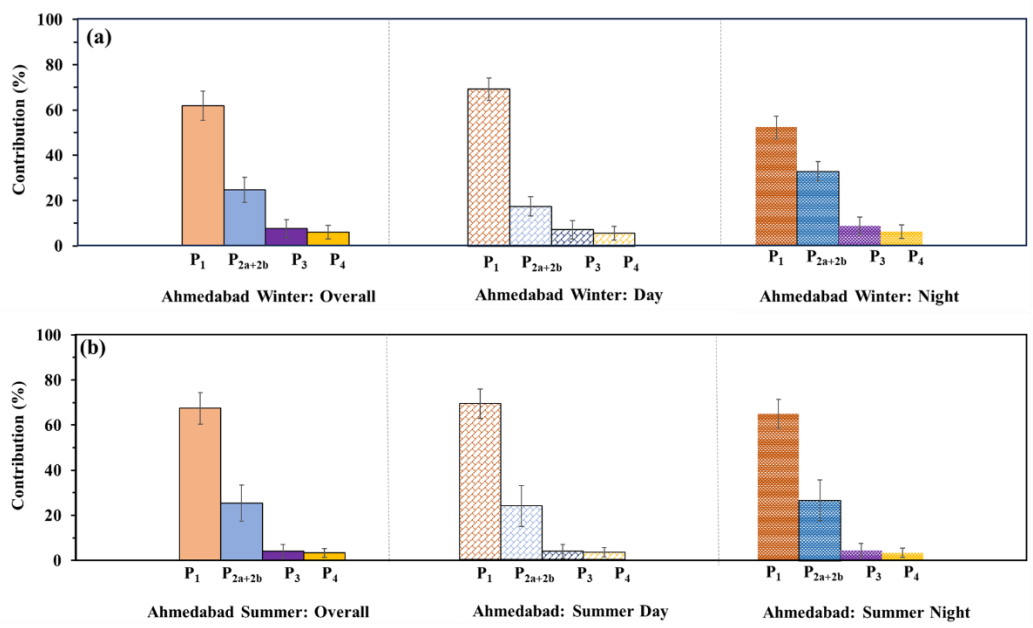

Figure 5.9. NO_3^- formation pathways over Ahmedabad during (a) Winter (b) Summer

Due to the minor contributions from P_3 and P_4, P_1 and P_2 were considered the major pathways for NO_3^- formation during both summer and winter. When considering only these two pathways, day-time NO_3^- in winter showed a 68% contribution from P_1, while night-time showed around 53%. The corresponding contributions from P_2 were 32% and 47% for day-time and night-time respectively. In summer, the contributions were more consistent, with P_1 accounting for 68% during the day-time and 66% at night-time. Further, during winter, $\delta^{15}N\text{-}NO_3^-$ showed a moderate but statistically significant positive correlation with $\delta^{18}O\text{-}NO_3^-$ over both Ahmedabad and Patiala, indicating the influence of at least two major formation pathways with different N isotopic fractionation. N_2O_5 hydrolysis pathway is associated with an elevated $\delta^{18}O\text{-}NO_3^-$ and higher N fractionation resulting in a higher $^{15}N/^{14}N$ (Walters & Michalski, 2015, 2016). Although the OH pathway was dominant in Patiala, the alternating contributions of OH-driven day-time formation and N_2O_5-driven night-time formation resulted in a diurnal variation that supported this isotopic correlation. These day-night shifts in pathway dominance were especially evident in winter due to lower boundary layer heights and presence of unstable NH_4NO_3, which allowed accumulation of freshly formed NO_3^- and limited atmospheric mixing. In contrast, no such correlation was observed in summer. This was likely due to a deeper boundary layer and stronger vertical mixing, which homogenized the air and diluted the isotopic differences between day and night NO_3^- sources (Huang et al., 2021).

Additionally, NO_3^- in summer was associated with more stable forms like non-volatile compounds, which are less sensitive to thermal loss or formation-time variability (Pathak et al., 2009; Wang et al., 2021). This chemical and meteorological stability limited the diurnal variability in $\delta^{15}N$ and $\delta^{18}O$, resulting in no meaningful correlation. Moreover, since $\delta^{15}N$ is influenced by both the formation pathway and the original NO_x source, its variability becomes more muted when chemical transformations remain consistent throughout the day. In essence, summer conditions (deep mixing layers and consistent chemistry) homogenize the nitrate isotopic composition, thereby suppressing any clear positive correlation between $\delta^{15}N$ and $\delta^{18}O$.

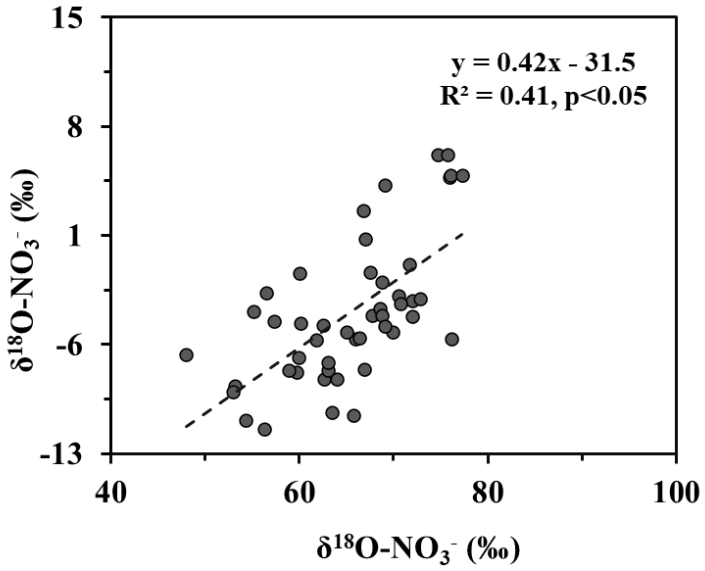

Figure 5.10. Relationship between $\delta^{18}O\text{-}NO_3^-$ and $\delta^{15}N\text{-}NO_3^-$ during winter over Ahmedabad

5.3.3 Sources of NO_x over Ahmedabad

The isotopic signatures of NO_x originating from fertilized soils and from urban or livestock waste are similarly depleted and tend to overlap, making it difficult to distinguish them. Therefore, they were grouped as a single source category (nsoil emission) for source apportionment (Felix & Elliott, 2014). Analysis using the MixSIAR model revealed no significant diurnal variation in source contributions across either season. However, a clear seasonal distinction was observed. In winter, traffic emissions contributed the highest NO_x (around 46.7 ± 19%), whereas day-time and night-time contributions of the same was 48.4 ± 17% and 51.4 ± 19% respectively. Contributions from soil emissions was, about 24.4 ± 12% overall, with day-time values of 25.8 ± 12% and night-time contribution of 20.1 ± 10%. Biomass burning, largely from domestic heating and seasonal combustion practices, contributed 18.0 ± 9% overall, with 17.2 ± 10% during the day and 19.0 ± 9% at night. Emissions from CFPPs remained relatively low throughout the season, contributing about 10.9 ± 8% overall, daytime and night-time contributions of 8.6 ± 7.1% and nigh-time 9.5 ± 8% respectively (Figure 5.11a). The consistency of CFPP contributions across both diurnal and seasonal scales suggests it acted as a relatively constant background source of NO_x.

During summer NO_x emissions were dominated by traffic exhaust and soil-related sources, contributing 40.1 ± 17% and 38.4 ± 12%, respectively. Biomass burning accounted for 11.3 ± 6%, while CFPPs consistently contributed a background

level of 10.2 ± 8%. Diurnal contributions showed no significant differences: during day-time, traffic emissions were 38.6 ± 15% and soil emissions 40.1 ± 12%, whereas at night, traffic and soil emissions increased and decreased slightly though not significantly to 41.6 ± 14% and 36.1 ± 12%. CFPPs and biomass burning remained relatively low throughout the day and night cycle (Figure 5.11b). This uniformity in source contributions during summer aligned with the N isotopic signature, which reported no diurnal variation in $\delta^{15}N\text{-}NO_3^-$ likely due to strong vertical mixing that homogenized the chemical environment across time periods. The dominance of soil emissions during summer could be attributed to high ambient temperatures (~34 °C), which enhanced microbial nitrification-denitrification cycle and accelerated the volatilization of Nr from urban and livestock wastes and fertilised lands. Although comparatively lower in winter, NO_x emission related to soil and urban/ human and livestock wastes, remained significant during the winter as well. In an urban setting like Ahmedabad, these emissions originate not only from soils but also from composting sites, sewage, and livestock areas, where microbial activity and thermal volatilization contribute to NO_x emissions. Satellite observations had also shown significant biogenic NOx across India (Ding et al., 2022). Further, existing studies has shown that urban and human waste can be a substantial source of NO_x in developing regions, particularly during warmer periods when microbial processes are more active (Casey et al., 2006; McElroy & Wang, 2005; Vinken et al., 2014; Yienger & Levy II, 1995).

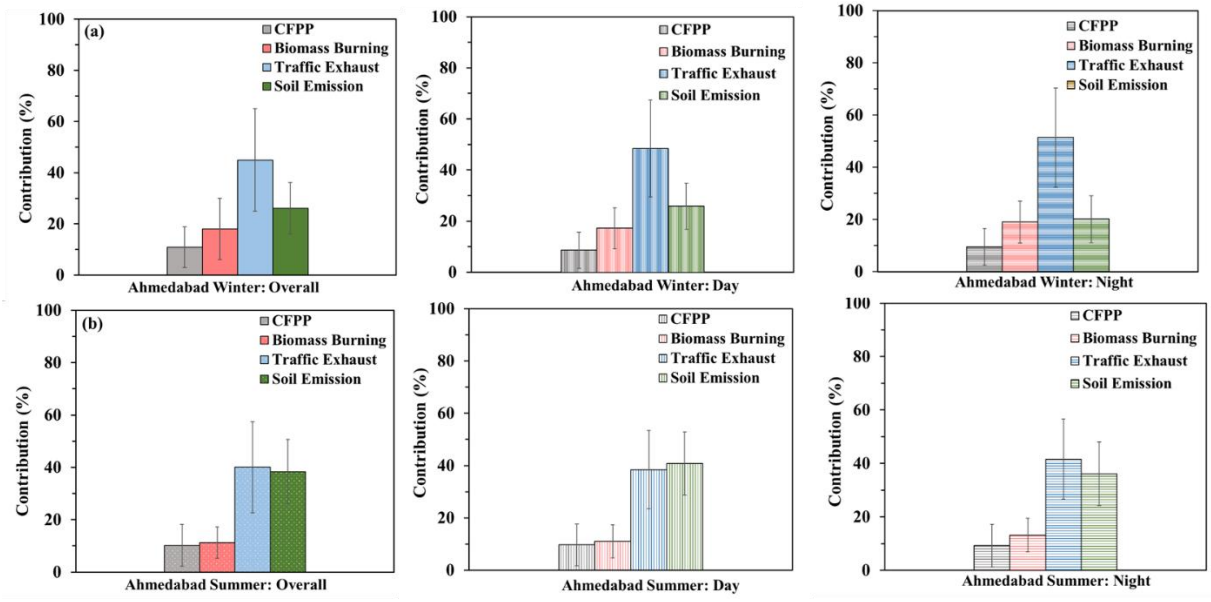

Figure 5.11. Sources of NOx over Ahmedabad during (a) Winter and (b) Summer

Vehicular emissions contributed significantly to NO_x levels in Ahmedabad during both summer and winter. Numerous studies have highlighted that traffic is a major source of both particulate matter and NO_x in big cities like Ahmedabad and Delhi, thus highlighting the consistent impact of transport-related pollution in these urban areas (Bano et al., 2024; Birenkumar & Sonali, 2023a; Goyal et al., 2013). In winter, when compared to summer, contribution of vehicular emission was significantly high. This apparent increase in vehicular contribution to NO_x during winter, compared to summer, could be attributed not only to local emissions but also to additional transport of pollutants, from northern part. This regional influence becomes more significant in winter due to prevailing northerly winds that carry an array of pollutants-both gases (including NO_x) and particulate, from highly polluted northern regions like Delhi, Uttar Pradesh, thus adding to the local atmospheric burden. In contrast, the summer season is dominated by hot, dry conditions and much deeper boundary layers (~1035 ± 495 m), which enhance vertical dispersion and reduce the impact of long-range transport. As a result, the elevated vehicular contribution observed in winter likely reflects the combined effect of continuous local traffic emissions and the added influx of transported NO_x from upwind regions in north India. Further, contribution from biomass burning also increased slightly in winter ($18 \pm 12\%$), likely due to domestic heating and regional agricultural residue burning. However, CFPPs continued to contribute a stable background level (~10%), consistent across seasons. Broadly, these source contributions reflected seasonal dynamics in Ahmedabad. Soil-related NO_x sources intensify during warmer months due to enhanced microbial activity and, on the other hand, combustion-related sources, particularly vehicular traffic, become more prominent in winter due to atmospheric stagnation. Seasonal shifts in emission sources of NO_x, with higher combustion and traffic related sources are also observed across multiple regions over the globe (Birenkumar & Sonali, 2023; Kuik et al., 2018; Lu et al., 2025; Wærsted et al., 2022; Weng et al., 2020). These trends highlight the need for season-specific air quality strategies in cities like Ahmedabad, where both anthropogenic and natural sources drive NO_x variability across the year.

Chapter 6

Summary and future scope

6.1 Summary

This thesis presents a comprehensive investigation into the partitioning behaviour, formation pathways, and source contributions of reactive nitrogen species particularly across diverse environments in India. The work combines gas-particle equilibrium modelling, stable isotopic techniques and Bayesian source apportionment (MixSIAR) to address key gaps in understanding the dynamics of reactive nitrogen under regionally variable meteorological and chemical regimes.

6.1.1 Chapter 3

This chapter provide insights into gas-particle partitioning of NH_x system and isotopic fractionation associated with it across five sites over India using $\delta^{15}N\text{-}NH_4^+$ and critical pH framework. Further, this chapter explored the effect of aerosol pH, ALWC and meteorology on the partitioning, and how the partitioning effects PM levels.

Over most of the sites, $HNO_3\text{-}NO_3^-$ was identified as the limitation factor in influencing PM concentration. This partitioning behaviour was thermodynamically consistent, and influenced by equilibrium fractionation. Over Patiala, the regime was mostly HNO_3 sensitive, with a few days fell in the dual sensitive zone. The dual sensitivity was driven by a higher ALWC and a relatively lower pH as evident from the observed correlations. Delhi was dominated by HNO_3 sensitivity, with a good match observed between high resolution online data and PM based measurements, indicating that partitioning was driven mostly by equilibrium effects, with little kinetic influence. Seasonal effect on partitioning was observed over Ahmedabad where input of NVCs from fine dusts during summer, drove the system towards HNO_3 sensitivity. A significant correlation between pH and NVCs further corroborated this, whereas insensitive samples showed a lack of significant relation. Dibrugarh and Shillong showed similar and consistent partitioning regime of HNO3 sensitivity, mostly driven by a moderately high pH. Further, good agreement of sensitivity regimes across sites between theoretical ε-pH and observed pH-ALWC plot across sites indicated that

transition from one sensitivity regime to another was primarily driven by pH. The shift from sensitivity and insensitivity was however mainly influenced by the ALWC, where a low ALWC drove the system towards insensitivity even at a similar aerosol pH.

Contrasting effect of meteorology on $\delta^{15}N\text{-}NH_4^+$ was observed. Expected positive and negative effects of RH and temperature on $\delta^{15}N\text{-}NH_4^+$ was observed, when NH_4^+ was present as stable $(NH_4)_2SO_4$. In contrast the opposite was observed when NH_4^+ also existed as semi-volatile NH_4NO_3. This indicated that when NH_4^+ was mainly in stable form, higher RH and lower temperature drove the gas-particle partitioning between NH_3 and NH_4^+ towards the particulate phase thus resulting in isotopic enrichment. whereas when NH_4^+ existed as semi-volatile form, volatilization under low RH and high temperature caused the residual NH_4^+ to have an elevated $\delta^{15}N\text{-}NH_4^+$ and the escaping NH_3 relatively depleted in ^{15}N. Further, the effects of meteorology were no always visible, as evident in Ahmedabad winter where no effects were observed. This was related to the diverse source profile observed in that area which masked the effects of meteorology.

6.1.2 Chapter 4

Source apportionment using $\delta^{15}N\text{-}NH_4^+$ coupled with MixSIAR was done across multiple sites in India encompassing both urban highly polluted to rural areas. Major sources considered were emissions from agriculture and urban wastes, biomass burning, CFPPs and traffic exhausts. Source contributions across sites showed seasonal variabilities primarily driven by meteorology.

Over Patiala, during post monsoon overall agriculture and urban waste emissions and biomass burning dominated overall during post monsoon. A clear shift in source contributions was observed, from being dominated by local combustion sources to showing a stronger regional influence from agricultural emissions. This shift in source profile from local to regional was due to wind speed changes. Elevated wind conditions marked by greater dispersion of pollutants caused the regional agricultural emissions to dominate, whereas, lower wind speed corresponded to limited mixing and more local influences from combustion sources. In winter contributions from thermal power plants were dominant owing to the proximity of the sampling site to multiple high power thermal power plants.

In Delhi, a shift in source contribution was also observed. During October to mid-November, contributions from agriculture and urban wastes dominated. This coincided with the Kharif crop harvesting activities which happen extensively in the surrounding upwind regions like Punjab, Haryana. Late November to February showed the dominance of biomass burning, consistent with the onset of winter, marked by an increase in heating needs, across northern India, contributing to enhanced NH_3 and $PM_{2.5}$.

Winter in Ahmedabad showed a diverse source profile with similar and high contributions from biomass burning (~ 33%) and agriculture and urban waste emissions (~30%). This was followed by traffic exhausts and CFPPs. In summer, however, the source profile shifted, marked by agriculture and urban wastes contributing to more than half of the total NH_3 emission. This increase in contribution during summer was related to the existence of a high ambient temperature, which promoted the volatilization of NH_3 from urban wastes and fertilizers. The contribution from biomass burning was much lower (~12%) in summer than in winter. Enhanced contributions from biomass burning were related to local heating during cold weather and could also be influenced by the transport of pollutants from northern parts. Traffic and CFPPs were consistent and similar across both seasons, representing a consistent background source over Ahmedabad. A diverse source contribution with different isotopic signatures during winter as compared to summer could have masked the effect of meteorology as seen in the previous chapter.

Dibrugarh and Shillong, located in the north eastern part of India, showed a similar source profile. Emissions from agriculture and urban wastes were the dominant contributors (~50%) in both the locations, this was followed by biomass burning contributing ~22% across both the locations. Both Dibrugarh and Shillong are mostly rural, with more than half of the land under cultivation. This, coupled with the extensive usage of fertiliser and livestock farming, enhanced NH_3 emissions across the regions. Biomass burning emissions were mostly related to domestic use of fuelwood, cow dung, and crop residue for cooking and heating purpose.

6.1.3 Chapter 5

Formation pathways of NO_3^- and sources of NO_x were estimated using dual isotopes of NO_3^- ($\delta^{15}N$ and $\delta^{18}O$) across 2 locations. Formation of NO_3^- formed via the

OH-pathway contributed dominantly over Patiala. Further, diurnal variations of pathway contributions revealed a significant difference between daytime and night-time. Although the NO_3^- formed via the OH- pathway was major during both day and night-time, its relative contribution was much higher during the day (~90%) than at night (~70%). Contributions from the N_2O_5 pathway were higher during night-time, owing to the lower ambient temperature and thermal instability of N_2O_5. A seemingly higher contribution from the OH pathway during night-time was due to residual NO_3^-, which was formed during the day but persisted and was collected at night. Presence of NO_3^- as stable compounds with NVCs during the study period further supported this. Furthermore, a shallow boundary layer at night promoted the accumulation of residual NO_3^-. Thus, the high OH-pathway contributions at night did not mean real NO_3^- formation by OH oxidation, but instead daytime-formed NO_3^- persisted at night due to the higher residence time of NO_3^- compared to the sampling durations.

Over Ahmedabad, a significant diurnal difference in formation pathways was observed only in winter. Day-time showed a higher contribution of NO_3^- formed via the OH pathway than night-time. The diurnal contrast observed over Ahmedabad in winter was much higher than that observed over Patiala. This was due to NO_3^- as semi-volatile NH_4NO_3, and as stable forms with NVCs. The presence of NO_3^- as semi-volatile NH_4NO_3 resulted in volatilization and loss of NO_3^- during elevated day-time temperature, thus reducing the residual effect. During summer, pathway contributions were diurnally consistent, aligning with the deep boundary layer height(~1000m) and greater vertical mixing.

Source apportionment revealed that traffic exhaust and biomass burning were the most significant contributors of NO_x, accounting for more than half of the NO_x emissions over Patiala during the post-monsoon. Traffic emissions are a well-established NO_x source in Patiala and other IGP cities. Further, the study period coincided with widespread agricultural residue burning across Punjab, contributing significantly to biomass burning-derived NO_x Over Patiala.

Over Ahmedabad, distinct seasonal differences in NO_x sources were observed. Traffic exhaust was the major contributor in winter, accounting for nearly half of the total NO_x emissions during winter. This was followed by contributions from biomass burning and soil emissions, which included wastewater, land composites, urban and human wastes and fertilized soil. A shift in a source profile was observed in summer,

with an increase in contribution from soil-related emissions, accounting for nearly ~40% of the total NO_x emissions. Emissions from traffic were high and similar to those of winter, indicating it to be a consistent and significant source of NO_x over Ahmedabad. The elevated contributions from soil-related emissions during summer were due to the increased microbial activity in warmer months that enhances NO_x volatilization from urban and livestock waste and fertilized soils. Satellite studies confirm significant biogenic NO_x emissions over India.

This chapter highlights the role of atmospheric stability and seasonality on the formation pathways of NO_3^- from its precursor. Further, this chapter also sheds light on the seasonal and regional variations in the sources of NO_x. This kind of work is essential, especially in the Indian Subcontinent, where NO_x emissions are among the highest, but lack comprehensive studies probing into the region-specific sources and formation mechanism of NO_x and NO_3^-.

6.2 Future Scope

1. **Seasonal and Regional Expansion of Partitioning Studies**
   Most of this study was conducted during winter and post-monsoon seasons. Including more seasons such as summer and monsoon, and extending to diverse regions like coastal/marine or forested areas, would help develop a more complete understanding of NH_3–NH_4^+ partitioning behaviours and aerosol pH sensitivity regimes across India.
2. **Linking Sensitivity Regimes to Nitrogen Deposition**
   Further research is needed to link partitioning regimes (HNO_3-sensitive, NH_3-sensitive, dual-sensitive) to depositional velocities of reactive nitrogen, particularly in ecologically sensitive zones like open oceans where nitrogen acts as a limiting nutrient.
3. **Triple Oxygen Isotopes and OH Source Attribution**
   Incorporating $\Delta^{17}O$ (^{17}O anomaly) in nitrate isotopic measurements can help distinguish the relative contribution of OH radicals derived from O_3 versus those formed from H_2O photolysis, offering deeper insight into atmospheric oxidation chemistry.
4. **Reducing Uncertainty in Source Apportionment**
   Due to lack of prior $\delta^{15}N$ data for Indian sources, current source apportionment

has high standard deviations. Establishing long-term multi-seasonal datasets for each site will allow the generation of more precise priors, improving the reliability of Bayesian models like MixSIAR.

5. **Simultaneous Measurement of Multiple Nitrogen Phases**
   Coordinated collection of gas-phase, particulate, and wet deposition samples with $\delta^{15}N$ and $\delta^{18}O$ measurements across phases can provide a comprehensive view of reactive nitrogen cycling and partitioning at a given location under specific meteorological conditions.
6. **Site-Specific Empirical Models**
   Long-term, high-resolution field data could help move beyond generalized empirical equations for partitioning and allow development of region-specific, observation-based models that better capture the unique dynamics of Indian atmospheric chemistry.

Appendix

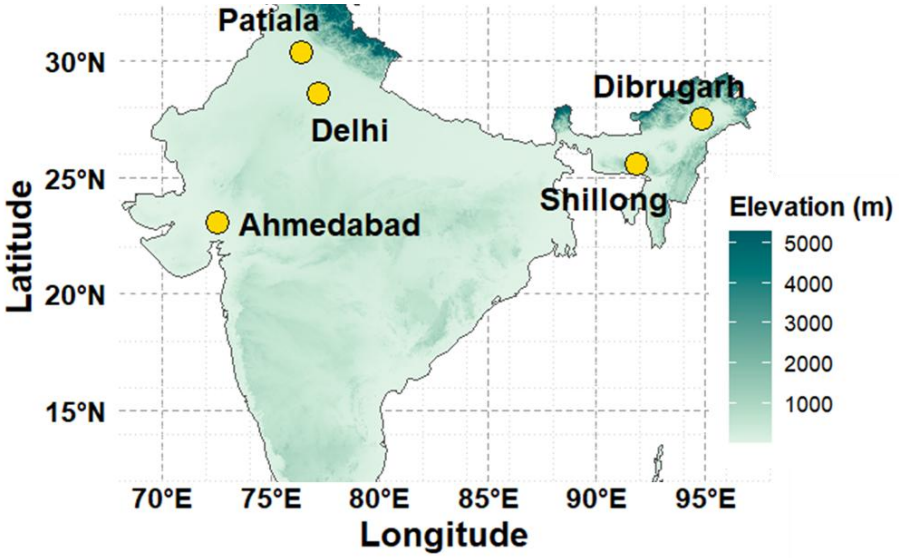

Figure S1. Map of aerosol sampling locations across India used in this study

Table S1. Major ions and PM concentrations across all sites. Numbers are denoted as Average ± 1σ

Site	Season	Species (µg/m³)								PM conc. (µg/m³)
		Na^+	NH_4^+	K^+	Ca^{2+}	Mg^{2+}	Cl^-	NO_3^-	SO_4^{2-}	
Patiala	Oct-Nov	0.5 ± 0.2	6.2 ± 4.5	5.6 ± 5.5	0.4 ± 0.1	0.7 ± 0.3	1.1 ± 1.3	7.7 ± 5.9	16.7 ± 11.3	255 ±119
Patiala	Dec-Jan	0.2 ± 0.2	17.3 ± 7.0	3.1 ± 1.2	0.3 ± 0.2	0.1 ± 0.4	4.3 ± 4.7	23.2 ± 10.0	27.5 ± 12.2	188 ± 63
Delhi	Oct-Feb	0.9 ± 0.7	13.2 ± 6.3	4.0 ± 3.5	0.6 ± 0.3	0.1 ± 0.1	3.5 ± 4.4	17.9 ± 9.2	20.5 ± 8.9	206 ± 87
Ahmedabad	Dec-Jan	0.6 ± 0.4	7.1 ± 2.9	1.7 ± 0.8	1.8 ± 1.8	0.1 ± 0.2	2.0 ± 2.5	9.9 ± 5.6	14.9 ± 7.3	137 ± 74
Ahmedabad	May-June	1.4 ± 1.1	1.7 ± 0.7	0.4 ± 0.2	1.3 ± 1.4	0.1 ± 0.1	1.7 ± 1.7	1.9 ± 1.5	6.6 ± 2.8	60 ± 52
Dibrugarh: $PM_{2.5}$	Jan-May	0.2 ± 0.2	1.5 ± 0.6	0.4 ± 0.2	0.1 ± 0.1	0.0 ± 0.0	0.2 ± 0.2	0.1 ± 0.1	3.3 ± 1.1	44 ± 16
Dibrugarh: PM_{10}	Jan-May	0.3 ± 0.2	1.4 ± 0.6	0.4 ± 0.2	0.3 ± 0.1	0.0 ± 0.0	0.3 ± 0.3	0.3 ± 0.2	4.4 ± 1.5	63 ± 24
Shillong	Jan-May	0.3 ± 0.2	3.7 ± 1.4	1.0 ± 0.5	0.2 ± 0.1	0.0 ± 0.0	0.3 ± 0.2	0.2 ± 0.2	9.3 ± 4.3	81 ± 109

References

Agnihotri, R., Mandal, T. K., Karapurkar, S. G., Naja, M., Gadi, R., Ahammmed, Y. N., Kumar, A., Saud, T., & Saxena, M. (2011). Stable carbon and nitrogen isotopic composition of bulk aerosols over India and northern Indian Ocean. *Atmospheric Environment*, *45*(17), 2828–2835. https://doi.org/10.1016/j.atmosenv.2011.03.003

Ahern, A. T., Goldberger, L., Jahl, L., Thornton, J., & Sullivan, R. C. (2018). Production of N2O5 and ClNO2 through Nocturnal Processing of Biomass-Burning Aerosol. *Environmental Science and Technology*, *52*(2), 550–559. https://doi.org/10.1021/acs.est.7b04386

Albertin, S., Savarino, J., Bekki, S., Barbero, A., Grilli, R., Fournier, Q., Ventrillard, I., Caillon, N., & Law, K. (2024). Diurnal variations in oxygen and nitrogen isotopes of atmospheric nitrogen dioxide and nitrate: implications for tracing NOx oxidation pathways and emission sources. *Atmospheric Chemistry and Physics*, *24*(2), 1361–1388. https://doi.org/10.5194/acp-24-1361-2024

Alexander, B., Hastings, M. G., Allman, D. J., Dachs, J., Thornton, J. A., & Kunasek, S. A. (2009). Atmospheric Chemistry and Physics Quantifying atmospheric nitrate formation pathways based on a global model of the oxygen isotopic composition (17 O) of atmospheric nitrate. In *Atmos. Chem. Phys* (Vol. 9). www.atmos-chem-phys.net/9/5043/2009/

Alexander, B., Sherwen, T., D Holmes, C., A Fisher, J., Chen, Q., J Evans, M., & Kasibhatla, P. (2020). Global inorganic nitrate production mechanisms: Comparison of a global model with nitrate isotope observations. *Atmospheric Chemistry and Physics*, *20*(6), 3859–3877. https://doi.org/10.5194/acp-20-3859-2020

Allen, S. A. A., Ree, A. G., Ayodeji, S. A. M., Deborah, S. A. E., & Ejike, O. M. (2019). Secondary inorganic aerosols: impacts on the global climate system and human health. *Biodiversity International Journal*, *3*(6), 249–259. https://doi.org/10.15406/bij.2019.03.00152

Altabet, M. A., Wassenaar, L. I., Douence, C., & Roy, R. (2019). A Ti(III) reduction method for one-step conversion of seawater and freshwater nitrate into N2O for stable isotopic analysis of 15N/14N, 18O/16O and 17O/16O. *Rapid Communications in Mass Spectrometry*, *33*(15), 1227–1239. https://doi.org/10.1002/rcm.8454

Andreae, M. O., & Merlet, P. (2001). Emission of trace gases and aerosols from biomass burning. *Global Biogeochemical Cycles*, *15*(4), 955–966. https://doi.org/10.1029/2000GB001382

Ansari, A. S., & Pandis, S. N. (2000). Water Absorption by Secondary Organic Aerosol and Its Effect on Inorganic Aerosol Behavior. *Environmental Science & Technology*, *34*(1), 71–77. https://doi.org/10.1021/es990717q

Arub, Z., Bhandari, S., Gani, S., Apte, J. S., Hildebrandt Ruiz, L., & Habib, G. (2020). Air mass physiochemical characteristics over New Delhi: Impacts on aerosol hygroscopicity and cloud condensation nuclei (CCN) formation. *Atmospheric Chemistry and Physics*, *20*(11), 6953–6971. https://doi.org/10.5194/acp-20-6953-2020

Asman, W. A. H. (1995). Parameterization of below-cloud scavenging of highly soluble gases under convective conditions. *Atmospheric Environment*, *29*(12), 1359–1368. https://doi.org/https://doi.org/10.1016/1352-2310(95)00065-7

Aumont, B., Madronich, S., Ammann, M., Kalberer, M., Baltensperger, U., Hauglustaine, D., & Brocheton, F. (1999). On the NO2 + soot reaction in the atmosphere. *Journal of Geophysical Research Atmospheres*, *104*(D1), 1729–1736. https://doi.org/10.1029/1998JD100023

Awasthi, A., Sinha, B., Hakkim, H., Mishra, S., Mummidivarapu, V., Singh, G., Ghude, S. D., Soni, V. K., Nigam, N., Sinha, V., & Rajeevan, M. N. (2024). Biomass-burning sources control ambient particulate matter, but traffic and industrial sources control volatile organic compound (VOC) emissions and secondary-pollutant formation during extreme pollution events in Delhi. *Atmospheric Chemistry and Physics*, *24*(18), 10279–10304. https://doi.org/10.5194/acp-24-10279-2024

Bano, S., Anand, V., Kalbande, R., Beig, G., & Rathore, D. S. (2024). Spatio-temporal variability and possible source identification of criteria pollutants from Ahmedabad-a megacity of Western India. *Journal of Atmospheric Chemistry*, *81*(1). https://doi.org/10.1007/s10874-023-09456-5

Beale, C. A., Paulot, F., Randles, C. A., Wang, R., Guo, X., Clarisse, L., Van Damme, M., Coheur, P. F., Clerbaux, C., Shephard, M. W., Dammers, E., Cady-Pereira, K., & Zondlo, M. A. (2022). Large sub-regional differences of ammonia seasonal patterns over India reveal inventory discrepancies. *Environmental Research Letters*, *17*(10). https://doi.org/10.1088/1748-9326/ac881f

Behera, S. N., Cheng, J., & Balasubramanian, R. (2015). In situ acidity and pH of size-fractionated aerosols during a recent smoke-haze episode in Southeast Asia. *Environmental Geochemistry and Health*, *37*(5), 843–859. https://doi.org/10.1007/s10653-014-9660-1

Behera, S. N., Sharma, M., Aneja, V. P., & Balasubramanian, R. (2013). Ammonia in the atmosphere: A review on emission sources, atmospheric chemistry and deposition on terrestrial bodies. In *Environmental Science and Pollution Research* (Vol. 20, Issue 11, pp. 8092–8131). https://doi.org/10.1007/s11356-013-2051-9

Bhargava, akshey, Bhargava, A., & Gopani, N. (2016). Assessment and Forecasting of Automobile Air Pollution Load in Ahmedabad based on different methods Assessment and Forecasting of Automobile Air Pollution Load in Ahmedabad based on different methods Authors. *Article in International Journal Of Scientific Research And Education*, *4*. https://doi.org/10.18535/ijsre/v4i04

Bhattarai, N., Wang, S., Pan, Y., Xu, Q., Zhang, Y., Chang, Y., & Fang, Y. (2021). δ15N-stable isotope analysis of NHx: An overview on analytical measurements, source sampling and its source apportionment. In *Frontiers of Environmental Science and Engineering* (Vol. 15, Issue 6). Higher Education Press Limited Company. https://doi.org/10.1007/s11783-021-1414-6

Bikkina, S., Andersson, A., Kirillova, E. N., Holmstrand, H., Tiwari, S., Srivastava, A. K., Bisht, D. S., & Gustafsson, Ö. (2019). Air quality in megacity Delhi affected by countryside biomass burning. *Nature Sustainability*, *2*(3), 200–205. https://doi.org/10.1038/s41893-019-0219-0

Bikkina, S., Kawamura, K., & Sarin, M. (2016). Stable carbon and nitrogen isotopic composition of fine mode aerosols (PM2.5) over the Bay of Bengal: Impact of continental sources. *Tellus, Series B: Chemical and Physical Meteorology*, *68*(1). https://doi.org/10.3402/tellusb.v68.31518

Birenkumar, P. B., & Sonali, P. D. (2023). Assessment of particulate matters from vehicular emission using operational street pollution model at Panjrapole, Ahmedabad (India). *Research Journal of Chemistry and Environment*, *27*(8), 66–75. https://doi.org/10.25303/2708rjce066075

Bray, C. D., Battye, W. H., Aneja, V. P., & Schlesinger, W. H. (2021). Global emissions of NH3, NOx, and N2O from biomass burning and the impact of climate change. *Journal of the Air & Waste Management Association*, *71*(1), 102–114. https://doi.org/10.1080/10962247.2020.1842822

Carter, T. J., Shaw, D. R., Carslaw, D. C., & Carslaw, N. (2024). Indoor cooking and cleaning as a source of outdoor air pollution in urban environments. *Environmental Science: Processes and Impacts*, *26*(6), 975–990. https://doi.org/10.1039/d3em00512g

Casey, K. D., Bicudo, J. R., Schmidt, D. R., Singh, A., Gay, S. W., Gates, R. S., Jacobson, L. D., & Hoff, S. J. (2006). *in Animal Agriculture and the Environment: National Center for Manure and Animal Waste Management White Papers*. ASABE. Pub.

Central Pollution Control Board (CPCB). *Continuous ambient air quality monitoring (CAAQM) dashboard. Government of India.* https://airquality.cpcb.gov.in/ccr/#/caaqm-dashboard-all/caaqm-landing

Chandra, N., Lal, S., Venkataramani, S., Patra, P. K., & Sheel, V. (2016). Temporal variations of atmospheric CO2 and CO at Ahmedabad in western India. *Atmospheric Chemistry and Physics*, *16*(10), 6153–6173. https://doi.org/10.5194/acp-16-6153-2016

Chang, Y., Cheng, K., Kuang, Y., Hu, Q., Gao, Y., Huang, R. J., Huang, C., Walters, W. W., & Lehmann, M. F. (2022). Isotopic Variability of Ammonia (δ15N-NH3) Slipped from Heavy-Duty Vehicles under Real-World Conditions. *Environmental Science and Technology Letters*, *9*(9), 726–732. https://doi.org/10.1021/acs.estlett.2c00526

Chang, Y., Zhang, Y., Tian, C., Zhang, S., Ma, X., Cao, F., Liu, X., Zhang, W., Kuhn, T., & Lehmann, M. F. (2018). Nitrogen isotope fractionation during gas-particle conversion of NOx to NO3- in the atmosphere – implications for isotope-based NOx source apportionment. *Atmospheric Chemistry and Physics*, *18*(16). https://doi.org/10.5194/ACP-2018-385

Chang, Y., Zou, Z., Deng, C., Huang, K., Collett, J. L., Lin, J., & Zhuang, G. (2016). The importance of vehicle emissions as a source of atmospheric ammonia in the megacity of Shanghai. *Atmospheric Chemistry and Physics*, *16*(5), 3577–3594. https://doi.org/10.5194/acp-16-3577-2016

Chen, T. Y., Chen, C. L., Chen, Y. C., Chou, C. C. K., Ren, H., & Hung, H. M. (2022). Source apportionment and evolution of N-containing aerosols at a rural cloud forest in Taiwan by isotope analysis. *Atmospheric Chemistry and Physics*, *22*(19), 13001–13012. https://doi.org/10.5194/acp-22-13001-2022

Chen, Z. L., Song, W., Hu, C. C., Liu, X. J., Chen, G. Y., Walters, W. W., Michalski, G., Liu, C. Q., Fowler, D., & Liu, X. Y. (2022). Significant contributions of combustion-related

sources to ammonia emissions. *Nature Communications*, *13*(1). https://doi.org/10.1038/s41467-022-35381-4

Choudhury, B. U., Fiyaz, A. R., Mohapatra, K. P., & Ngachan, S. (2016). Impact of Land Uses, Agrophysical Variables and Altitudinal Gradient on Soil Organic Carbon Concentration of North-Eastern Himalayan Region of India. *Land Degradation and Development*, *27*(4), 1163–1174. https://doi.org/10.1002/ldr.2338

Clegg, S. L., Brimblecombe, P., & Wexler, A. S. (1998). Thermodynamic model of the system H^+–NH_4^+–SO_4^{2-}–NO_3^-–H_2O at tropospheric temperatures. *The Journal of Physical Chemistry A, 102*(12), 2137–2154. https://doi.org/10.1021/jp973042r

Clegg, S. L., & Brimblecombe, Peter. (1990). Equilibrium partial pressures and mean activity and osmotic coefficients of 0-100% nitric acid as a function of temperature. *The Journal of Physical Chemistry*, *94*(13), 5369–5380. https://doi.org/10.1021/j100376a038

Cohen, A. J., Brauer, M., Burnett, R., Anderson, H. R., Frostad, J., Estep, K., Balakrishnan, K., Brunekreef, B., Dandona, L., Dandona, R., Feigin, V., Freedman, G., Hubbell, B., Jobling, A., Kan, H., Knibbs, L., Liu, Y., Martin, R., Morawska, L., … Forouzanfar, M. H. (2017). Estimates and 25-year trends of the global burden of disease attributable to ambient air pollution: an analysis of data from the Global Burden of Diseases Study 2015. *The Lancet*, *389*(10082), 1907–1918. https://doi.org/10.1016/S0140-6736(17)30505-6

Crutzen, P. J. (1970). The influence of nitrogen oxides on the atmospheric ozone content. *Quarterly Journal of the Royal Meteorological Society, 96*(408), 320–325. https://doi.org/10.1002/qj.49709640815

Crutzen, P. J. (1974). Photochemical reactions initiated by and influencing ozone in unpolluted tropospheric air. *Tellus*, *26*(1–2), 47–57. https://doi.org/10.1111/j.2153-3490.1974.tb01951.x

Crutzen, P. J. (1979). The role of NO and NO_2 in the chemistry of the troposphere and stratosphere. *Annual Review of Earth and Planetary Sciences, 7*(1), 443–472. https://doi.org/10.1146/annurev.ea.07.050179.002303

de Vries, W. (2021). Impacts of nitrogen emissions on ecosystems and human health: A mini review. In *Current Opinion in Environmental Science and Health* (Vol. 21). Elsevier B.V. https://doi.org/10.1016/j.coesh.2021.100249

Department of Animal Husbandry & Dairying. (2022). Government of India

Dentener, F., Drevet, J., Lamarque, J. F., Bey, I., Eickhout, B., & others. (2006). Nitrogen and sulfur deposition on regional and global scales: A multimodel evaluation. *Global Biogeochemical Cycles, 20*, GB4003. https://doi.org/10.1029/2005GB002672

Deshpande, R. D., Maurya, A. S., Kumar, B., Sarkar, A., & Gupta, S. K. (2010). Rain-vapor interaction and vapor source identification using stable isotopes from semiarid western India. *Journal of Geophysical Research Atmospheres*, *115*(23). https://doi.org/10.1029/2010JD014458

Devaprasad, M., Rastogi, N., Satish, R., Patel, A., Singh, A., Dabhi, A., Shivam, A., Bhushan, R., & Meena, R. (2023). Characterization of paddy-residue burning derived carbonaceous aerosols using dual carbon isotopes. *Science of the Total Environment*, *864*. https://doi.org/10.1016/j.scitotenv.2022.161044

Ding, J., van der A, R., Mijling, B., de Laat, J., Eskes, H., & Boersma, K. F. (2022). NOx emissions in India derived from OMI satellite observations. *Atmospheric Environment: X*, *14*. https://doi.org/10.1016/j.aeaoa.2022.100174

Dong, X., Guo, Q., Han, X., Wei, R., & Tao, Z. (2022). The isotopic patterns and source apportionment of nitrate and ammonium in atmospheric aerosol. *Science of the Total Environment*, *803*. https://doi.org/10.1016/j.scitotenv.2021.149559

Elliott, E. M., Kendall, C., Wankel, S. D., Burns, D. A., Boyer, E. W., Harlin, K., Bain, D. J., & Butler, T. J. (2007). Nitrogen isotopes as indicators of NOx source contributions to atmospheric nitrate deposition across the midwestern and northeastern United States. *Environmental Science and Technology*, *41*(22), 7661–7667. https://doi.org/10.1021/es070898t

Ellison, G. B., Tuck, A. F., & Vaida, V. (1999). Atmospheric processing of organic aerosols. *Journal of Geophysical Research Atmospheres*, *104*(D9), 11633–11641. https://doi.org/10.1029/1999JD900073

Emery, C., Liu, Z., Russell, A. G., Odman, M. T., Yarwood, G., & Kumar, N. (2017). Recommendations on statistics and benchmarks to assess photochemical model performance. *Journal of the Air and Waste Management Association*, *67*(5), 582–598. https://doi.org/10.1080/10962247.2016.1265027

Erisman, J. W., Galloway, J. N., Seitzinger, S., Bleeker, A., Dise, N. B., Roxana Petrescu, A. M., Leach, A. M., & de Vries, W. (2013). Consequences of human modification of the global nitrogen cycle. *Philosophical Transactions of the Royal Society B: Biological Sciences*, *368*(1621). https://doi.org/10.1098/rstb.2013.0116

Fan, M. Y., Zhang, W., Zhang, Y. L., Li, J., Fang, H., Cao, F., Yan, M., Hong, Y., Guo, H., & Michalski, G. (2023). Formation Mechanisms and Source Apportionments of Nitrate Aerosols in a Megacity of Eastern China Based On Multiple Isotope Observations. *Journal of Geophysical Research: Atmospheres*, *128*(6). https://doi.org/10.1029/2022JD038129

Fan, M. Y., Zhang, Y. L., Lin, Y. C., Hong, Y., Zhao, Z. Y., Xie, F., Du, W., Cao, F., Sun, Y., & Fu, P. (2022). Important Role of NO3Radical to Nitrate Formation Aloft in Urban Beijing: Insights from Triple Oxygen Isotopes Measured at the Tower. *Environmental Science and Technology*, *56*(11), 6870–6879. https://doi.org/10.1021/acs.est.1c02843

Fan, M.-Y., Zhang, Y.-L., Hong, Y., Lin, Y.-C., Zhao, Z.-Y., Cao, F., Sun, Y., Guo, H., & Fu, P. (2022). Vertical Differences of Nitrate Sources in Urban Boundary Layer Based on Tower Measurements. *Environmental Science & Technology Letters*, *9*(11), 906–912. https://doi.org/10.1021/acs.estlett.2c00600

Fang, Z., Dong, S., Huang, C., Jia, S., Wang, F., Liu, H., Meng, H., Luo, L., Chen, Y., Zhang, H., Li, R., Zhu, Y., & Tang, M. (2024). On using an aerosol thermodynamic model to calculate aerosol acidity of coarse particles. *Journal of Environmental Sciences (China)*, *148*, 46–56. https://doi.org/10.1016/j.jes.2023.07.001

Felix, J. D., & Elliott, E. M. (2014). Isotopic composition of passively collected nitrogen dioxide emissions: Vehicle, soil and livestock source signatures. *Atmospheric Environment*, *92*, 359–366. https://doi.org/10.1016/j.atmosenv.2014.04.005

Felix, J. D., Elliott, E. M., & Shaw, S. L. (2012). Nitrogen isotopic composition of coal-fired power plant NOx: Influence of emission controls and implications for global emission

inventories. *Environmental Science and Technology*, *46*(6), 3528–3535. https://doi.org/10.1021/es203355v

Fibiger, D. L., & Hastings, M. G. (2016). First Measurements of the Nitrogen Isotopic Composition of NOx from Biomass Burning. *Environmental Science and Technology*, *50*(21), 11569–11574. https://doi.org/10.1021/acs.est.6b03510

Forzatti, P. (2001). Present status and perspectives in de-NOx SCR catalysis. *Applied Catalysis A: General*, *222*(1), 221–236. https://doi.org/https://doi.org/10.1016/S0926-860X(01)00832-8

Fountoukis, C., & Nenes, A. (2007). Atmospheric Chemistry and Physics ISORROPIA II: a computationally efficient thermodynamic equilibrium model for K +-Ca 2+-Mg 2+-NH + 4-Na +-SO 2− 4-NO − 3-Cl −-H 2 O aerosols. In *Atmos. Chem. Phys* (Vol. 7). www.atmos-chem-phys.net/7/4639/2007/

Fowler, D., Coyle, M., Skiba, U., Sutton, M. A., Cape, J. N., Reis, S., Sheppard, L. J., Jenkins, A., Grizzetti, B., Galloway, J. N., Vitousek, P., Leach, A., Bouwman, A. F., Butterbach-Bahl, K., Dentener, F., Stevenson, D., Amann, M., & Voss, M. (2013). The global nitrogen cycle in the Twentyfirst century. *Philosophical Transactions of the Royal Society B: Biological Sciences*, *368*(1621). https://doi.org/10.1098/rstb.2013.0164

Freyer H.d. (1991). Seasonal variation of 15N/14N ratios in atmospheric nitrate species. *Tellus B*, *43*(1), 30–44. https://doi.org/10.1034/j.1600-0889.1991.00003.x

Galanter, M., Levy, H., & Carmichael, G. R. (2000). Impacts of biomass burning on tropospheric CO, NOx, and O3. *Journal of Geophysical Research Atmospheres*, *105*(D5), 6633–6653. https://doi.org/10.1029/1999JD901113

Galloway, J. N. (1998). *The global nitrogen cycle: Changes and consequences. Environmental Pollution, 102,* 15–24.

Galloway, J. N., & Cowling, E. B. (2002). *Reactive nitrogen and the world: 200 years of change. Ambio, 31(2),* 64–71. https://doi.org/10.1579/0044-7447-31.2.64

Galloway, J. N., Dentener, F. J., Capone, D. G., Boyer, E. W., Howarth, R. W., Seitzinger, S. P., Asner, G. P., Cleveland, C. C., Green, P. A., Holland, E. A., Karl, D. M., Michaels, A. F., Porter, J. H., Townsend, A. R., & Vörösmarty, C. J. (2004). *Nitrogen cycles: Past, present, and future. Biogeochemistry, 70(2),* 153–226. https://doi.org/10.1007/s10533-004-03700

Galloway, J. N., Bleeker, A., & Erisman, J. W. (2025). *The human creation and use of reactive nitrogen: A global and regional perspective. Annual Review of Environment and Resources.* https://doi.org/10.1146/annurev-environ-012420

Ghude, S. D., Pfister, G. G., Jena, C. K., van der A, R. J., Emmons, L. K., & Kumar, R. (2012). Satellite constraints of Nitrogen Oxide (NOX) emissions from India based on OMI observations and WRF-Chem simulations. *Geophysical Research Letters*. https://doi.org/10.1029/2012gl053926

Goel, R., Guttikunda, S. K., Mohan, D., & Tiwari, G. (2015). Benchmarking vehicle and passenger travel characteristics in Delhi for on-road emissions analysis. *Travel Behaviour and Society*, *2*(2), 88–101. https://doi.org/10.1016/j.tbs.2014.10.001

Goel, V., Hazarika, N., Kumar, M., & Singh, V. (2021). Source apportionment of black carbon over Delhi: A case study of extreme biomass burning events and Diwali festival. *Urban Climate*, *39*. https://doi.org/10.1016/j.uclim.2021.100926

Gogoi, M. M., Pathak, B., Moorthy, K. K., Bhuyan, P. K., Babu, S. S., Bhuyan, K., & Kalita, G. (2011). Multi-year investigations of near surface and columnar aerosols over Dibrugarh, northeastern location of India: Heterogeneity in source impacts. *Atmospheric Environment*, *45*(9), 1714–1724. https://doi.org/10.1016/j.atmosenv.2010.12.056

Government of Assam. (2021). *Statistical Handbook Assam*.

Government of Meghalaya. (2019). *Statistical Handbook Meghalaya*.

Goyal, P., Mishra, D., & Kumar, A. (2013). Vehicular emission inventory of criteria pollutants in Delhi. *SpringerPlus*, *2*(1), 1–11. https://doi.org/10.1186/2193-1801-2-216

Guo, H., Liu, J., Froyd, K. D., Roberts, J. M., Veres, P. R., Hayes, P. L., Jimenez, J. L., Nenes, A., & Weber, R. J. (2017). Fine particle pH and gas-particle phase partitioning of inorganic species in Pasadena, California, during the 2010 CalNex campaign. *Atmospheric Chemistry and Physics*, *17*(9), 5703–5719. https://doi.org/10.5194/acp-17-5703-2017

Guo, H., Otjes, R., Schlag, P., Kiendler-Scharr, A., Nenes, A., & Weber, R. J. (2018). Effectiveness of ammonia reduction on control of fine particle nitrate. *Atmospheric Chemistry and Physics*, *18*(16), 12241–12256. https://doi.org/10.5194/acp-18-12241-2018

Guo, H., Sullivan, A. P., Campuzano-Jost, P., Schroder, J. C., Lopez-Hilfiker, F. D., Dibb, J. E., Jimenez, J. L., Thornton, J. A., Brown, S. S., Nenes, A., & Weber, R. J. (2016). Fine particle pH and the partitioning of nitric acid during winter in the northeastern United States. *Journal of Geophysical Research*, *121*(17), 10355–10376. https://doi.org/10.1002/2016JD025311

Guo, H., Xu, L., Bougiatioti, A., Cerully, K. M., Capps, S. L., Hite, J. R., Carlton, A. G., Lee, S. H., Bergin, M. H., Ng, N. L., Nenes, A., & Weber, R. J. (2015). Fine-particle water and pH in the southeastern United States. *Atmospheric Chemistry and Physics*, *15*(9), 5211–5228. https://doi.org/10.5194/acp-15-5211-2015

Guo, W., Luo, L., Zhang, Z., Zheng, N., Xiao, H., & Xiao, H. (2021). The use of stable oxygen and nitrogen isotopic signatures to reveal variations in the nitrate formation pathways and sources in different seasons and regions in China. *Environmental Research*, *201*. https://doi.org/10.1016/j.envres.2021.111537

Guo, W., Zheng, N., & Zhang, Z. (2021). Stable nitrogen isotopic signatures reveal the NH4+ evolution processes in pollution episodes in urban southwestern China. *Atmospheric Research*, *253*. https://doi.org/10.1016/j.atmosres.2021.105474

Gupta, A., Kumar, R., Kumari, K. M., & Srivastava, S. S. (2003). Measurement of NO2, HNO3, NH3 and SO 2 and related particulate matter at a rural site in Rampur, India. *Atmospheric Environment*, *37*(34), 4837–4846. https://doi.org/10.1016/j.atmosenv.2003.07.008

Halder, B., Barman, S., Banik, P., Das, P., Bandyopadhyay, J., Tangang, F., Shahid, S., Pande, C. B., Al-Ramadan, B., & Yaseen, Z. M. (2023). Large-Scale Flood Hazard Monitoring and Impact Assessment on Landscape: Representative Case Study in India. *Sustainability (Switzerland)*, *15*(14). https://doi.org/10.3390/su151411413

Hastings, M. G., Sigman, D. M., & Lipschultz, F. (2003). Isotopic evidence for source changes of nitrate in rain at Bermuda. *Journal of Geophysical Research: Atmospheres*, *108*(24). https://doi.org/10.1029/2003jd003789

Heaton, T. H. E. (1987). ^15N/^14N ratios of nitrate and ammonium in rain at Pretoria, South Africa. *Atmospheric Environment, 21*(4), 843–852. https://doi.org/10.1016/0004-6981(87)90080-1

Henneman, L. R. F., Liu, C., Hu, Y., Mulholland, J. A., & Russell, A. G. (2017). Air quality modeling for accountability research: Operational, dynamic, and diagnostic evaluation. *Atmospheric Environment*, *166*, 551–565. https://doi.org/10.1016/j.atmosenv.2017.07.049

Hersbach, H., Bell, B., Berrisford, P., Hirahara, S., Horányi, A., Muñoz-Sabater, J., Nicolas, J., Peubey, C., Radu, R., Schepers, D., Simmons, A., Soci, C., Abdalla, S., Abellan, X., Balsamo, G., Bechtold, P., Biavati, G., Bidlot, J., Bonavita, M., … Thépaut, J. N. (2020). The ERA5 global reanalysis. *Quarterly Journal of the Royal Meteorological Society*, *146*(730), 1999–2049. https://doi.org/10.1002/qj.3803

Hu, J. H., & Abbatt, J. P. D. (1996). *Reaction Probabilities for N 2 O 5 Hydrolysis on Sulfuric Acid and Ammonium Sulfate Aerosols at Room Temperature*.

Huang, C., Hu, Q., Lou, S., Tian, J., Wang, R., Xu, C., An, J., Ren, H., Ma, D., Quan, Y., Zhang, Y., & Li, L. (2018). Ammonia Emission Measurements for Light-Duty Gasoline Vehicles in China and Implications for Emission Modeling. *Environmental Science and Technology*, *52*(19), 11223–11231. https://doi.org/10.1021/acs.est.8b03984

Huang, W., Ye, X., Lv, Z., Yao, Y., Chen, Y., Zhou, Y., & Chen, J. (2024). Dual isotopic evidence of δ15N and δ18O for priority control of vehicle emissions in a megacity of East China: Insight from measurements in summer and winter. *Science of the Total Environment*, *931*. https://doi.org/10.1016/j.scitotenv.2024.172918

(IPCC), I. P. on C. C. (2023). *Climate Change 2021 – The Physical Science Basis: Working Group I Contribution to the Sixth Assessment Report of the Intergovernmental Panel on Climate Change*. Cambridge University Press. https://doi.org/DOI: 10.1017/9781009157896

Ito, A. (2015). Atmospheric processing of combustion aerosols as a source of bioavailable iron. *Environmental Science and Technology Letters*, *2*(3), 70–75. https://doi.org/10.1021/acs.estlett.5b00007

Jacob, D. J. (1999). *Introduction to atmospheric chemistry*. Princeton University Press. http://site.ebrary.com/id/10514793

Johnson, T., & Joshi, A. (2018). Review of Vehicle Engine Efficiency and Emissions. *SAE International Journal of Engines*, *11*(6), 1307–1330. https://www.jstor.org/stable/26649163

Kawamura, K., Kobayashi, M., Tsubonuma, N., Mochida, M., Watanabe, T., & Lee, M. (2004). Organic and inorganic compositions of marine aerosols from East Asia: Seasonal variations of water-soluble dicarboxylic acids, major ions, total carbon and nitrogen, and stable C and N isotopic composition. *The Geochemical Society Special Publications, 9,* 243–265. https://doi.org/10.1016/S1873-9881(04)80019-1

Kirshenbaum, I., Smith, J. S., Crowell, T., Graff, J., & McKee, R. (1947). Separation of the nitrogen isotopes by the exchange reaction between ammonia and solutions of ammonium nitrate. *The Journal of Chemical Physics*, *15*(7), 440–446. https://doi.org/10.1063/1.1746562

Kleinman, L. I. (1994). Low and high NOx tropospheric photochemistry. *Journal of Geophysical Research*, *99*(D8). https://doi.org/10.1029/94jd01028

Koebel, M., Elsener, M., & Kleemann, M. (2000). Urea-SCR: a promising technique to reduce NO x emissions from automotive diesel engines. In *Catalysis Today* (Vol. 59).

Kotnala, G., Sharma, S. K., & Mandal, T. K. (2020). Influence of Vehicular Emissions (NO, NO2, CO and NMHCs) on the Mixing Ratio of Atmospheric Ammonia (NH3) in Delhi, India. *Archives of Environmental Contamination and Toxicology*, *78*(1), 79–85. https://doi.org/10.1007/s00244-019-00689-8

Krishnamurthy, A., Moore, J. K., Mahowald, N., Luo, C., & Zender, C. S. (2010). Impacts of atmospheric nutrient inputs on marine biogeochemistry. *Journal of Geophysical Research: Biogeosciences, 115*, G01006. https://doi.org/10.1029/2009JG001115

Kuhn, J., Vallabani, N. V. S., Montes, A. M., Juárez-Facio, A. T., Introna, M., Steimer, S. S., Patel, A., Manem, D. B., Tsyupa, B., Mancini, A., Olofsson, U., Elihn, K., & Karlsson, H. L. (2025). Unraveling toxicity of nanoparticles from different subway materials in lung epithelial cells and macrophages. *Environmental Research*, *271*. https://doi.org/10.1016/j.envres.2025.121027

Kuik, F., Kerschbaumer, A., Lauer, A., Lupascu, A., Von Schneidemesser, E., & Butler, T. M. (2018). Top-down quantification of NOx emissions from traffic in an urban area using a high-resolution regional atmospheric chemistry model. *Atmospheric Chemistry and Physics*, *18*(11), 8203–8225. https://doi.org/10.5194/acp-18-8203-2018

Kulshrestha, U. C., Granat, L., Engardt, M., & Rodhe, H. (2005). Review of precipitation monitoring studies in India - A search for regional patterns. *Atmospheric Environment*, *39*(38), 7403–7419. https://doi.org/10.1016/j.atmosenv.2005.08.035

Kumar, S., Sharma, D. K., Singh, D. R., Biswas, H., Praveen, K. V., & Sharma, V. (2019). Estimating loss of ecosystem services due to paddy straw burning in North-west India. *International Journal of Agricultural Sustainability*, *17*(2), 146–157. https://doi.org/10.1080/14735903.2019.1581474

Kundu, S., Kawamura, K., & Lee, M. (2010). Seasonal variation of the concentrations of nitrogenous species and their nitrogen isotopic ratios in aerosols at Gosan, Jeju Island: Implications for atmospheric processing and source changes of aerosols. *Journal of Geophysical Research Atmospheres*, *115*(20). https://doi.org/10.1029/2009JD013323

Kuttippurath, J., Singh, A., Dash, S. P., Mallick, N., Clerbaux, C., Van Damme, M., Clarisse, L., Coheur, P. F., Raj, S., Abbhishek, K., & Varikoden, H. (2020). Record high levels of atmospheric ammonia over India: Spatial and temporal analyses. *Science of the Total Environment*, *740*. https://doi.org/10.1016/j.scitotenv.2020.139986

Lalchandani, V., Kumar, V., Tobler, A., M. Thamban, N., Mishra, S., Slowik, J. G., Bhattu, D., Rai, P., Satish, R., Ganguly, D., Tiwari, S., Rastogi, N., Tiwari, S., Močnik, G., Prévôt, A. S. H., & Tripathi, S. N. (2021). Real-time characterization and source apportionment of

fine particulate matter in the Delhi megacity area during late winter. *Science of the Total Environment*, *770*. https://doi.org/10.1016/j.scitotenv.2021.145324

Leighton, P. (1961). Photochemistry of Air Pollution. *Academic, New York*.

Li, H., Zhang, Q., Zheng, B., Chen, C., Wu, N., Guo, H., Zhang, Y., Zheng, Y., Li, X., & He, K. (2018). Nitrate-driven urban haze pollution during summertime over the North China Plain. *Atmospheric Chemistry and Physics*, *18*(8), 5293–5306. https://doi.org/10.5194/acp-18-5293-2018

Li, Q., Jiang, J., Cai, S., Zhou, W., Wang, S., Duan, L., & Hao, J. (2016). Gaseous Ammonia Emissions from Coal and Biomass Combustion in Household Stoves with Different Combustion Efficiencies. *Environmental Science and Technology Letters*, *3*(3), 98–103. https://doi.org/10.1021/acs.estlett.6b00013

Li, Q., Li, X. D., Yang, Z., Cui, G., & Ding, S. (2021). Diurnal and seasonal variations in water-soluble inorganic ions and nitrate dual isotopes of PM2.5: Implications for source apportionment and formation processes of urban aerosol nitrate. *Atmospheric Research*, *248*. https://doi.org/10.1016/j.atmosres.2020.105197

Li, T., Li, J., Sun, Z., Jiang, H., Tian, C., & Zhang, G. (2023). *High contribution of anthropogenic combustion sources to atmospheric inorganic reactive nitrogen in South China evidenced by isotopes*. https://doi.org/10.5194/acp-2023-49

Li, Y., Liu, J., George, C., Herrmann, H., Gu, M., Yang, M., Wang, Y., Mellouki, A., Pan, Y., Felix, J. D., Kawashima, H., Zhang, Z., Wang, S., & Zeng, Y. (2023). Apportioning Atmospheric Ammonia Sources across Spatial and Seasonal Scales by Their Isotopic Fingerprint. *Environmental Science and Technology*, *57*(43), 16424–16434. https://doi.org/10.1021/acs.est.3c04027

Lim, S., Yang, X., Lee, M., Li, G., Gao, Y., Shang, X., Zhang, K., Czimczik, C. I., Xu, X., Bae, M. S., Moon, K. J., & Jeon, K. (2020). Fossil-driven secondary inorganic PM2.5 enhancement in the North China Plain: Evidence from carbon and nitrogen isotopes. *Environmental Pollution*, *266*. https://doi.org/10.1016/j.envpol.2020.115163

Lin, Y. C., Zhang, Y. L., Yu, M., Fan, M. Y., Xie, F., Zhang, W. Q., Wu, G., Cong, Z., & Michalski, G. (2021). Formation Mechanisms and Source Apportionments of Airborne Nitrate Aerosols at a Himalayan-Tibetan Plateau Site: Insights from Nitrogen and Oxygen Isotopic Compositions. *Environmental Science and Technology*, *55*(18), 12261–12271. https://doi.org/10.1021/acs.est.1c03957

Liu, C., Wang, H., & Guo, H. (2019). Redistribution of PM2.5-associated nitrate and ammonium during outdoor-to-indoor transport. *Indoor Air*, *29*(3), 460–468. https://doi.org/10.1111/ina.12549

Liu, J., Cohen, J. B., He, Q., Tiwari, P., & Qin, K. (2024). Accounting for NOx emissions from biomass burning and urbanization doubles existing inventories over South, Southeast and East Asia. *Communications Earth and Environment*, *5*(1). https://doi.org/10.1038/s43247-024-01424-5

Liu, X. (2023). Aerosols and Climate Effects. In *Fast Processes in Large-Scale Atmospheric Models* (pp. 53–86). American Geophysical Union (AGU). https://doi.org/https://doi.org/10.1002/9781119529019.ch3

Liu, X., Zhang, Y., Han, W., Tang, A., Shen, J., Cui, Z., Vitousek, P., Erisman, J. W., Goulding, K., Christie, P., Fangmeier, A., & Zhang, F. (2013). Enhanced nitrogen deposition over China. *Nature*, *494*(7438), 459–462. https://doi.org/10.1038/nature11917

Liu, Y., Ge, Y., Tan, J., Wang, H., & Ding, Y. (2021). Research on ammonia emissions characteristics from light-duty gasoline vehicles. *Journal of Environmental Sciences (China)*, *106*, 182–193. https://doi.org/10.1016/j.jes.2021.01.021

Liu, Y., Wang, H., Li, N., Tan, J., & Chen, D. (2021). Research on ammonia emissions from three-way catalytic converters based on small sample test and vehicle test. *Science of the Total Environment*, *795*. https://doi.org/10.1016/j.scitotenv.2021.148926

Lozhkina, O. V, & Lozhkin, V. N. (2016). Estimation of nitrogen oxides emissions from petrol and diesel passenger cars by means of on-board monitoring: Effect of vehicle speed, vehicle technology, engine type on emission rates. *Transportation Research Part D: Transport and Environment*, *47*, 251–264. https://doi.org/https://doi.org/10.1016/j.trd.2016.06.008

Lu, C., Dong, S., Huang, S., Gao, S., Fu, J., Tian, X., Lin, S., Xiong, X., Wang, X., & Wang, X. (2025). Real-traffic emissions of CO, NOx, CO2, and PM2.5 from vehicles using a portable emission measurement system. *Air Quality, Atmosphere and Health*. https://doi.org/10.1007/s11869-025-01765-w

Luo, C., Mahowald, N. M., Bond, T., Chuang, P. Y., Artaxo, P., Siefert, R., Chen, Y., & Schauer, J. (2008). Combustion iron distribution and deposition. *Global Biogeochemical Cycles, 22*, GB1012. https://doi.org/10.1029/2007GB002964

Luo, C., Zender, C. S., Bian, H., & Metzger, S. (2007). Role of ammonia chemistry and coarse mode aerosols in global climatological inorganic aerosol distributions. *Atmospheric Environment, 41*(12), 2510–2533.

Luo, L., Kao, S. J., Wu, Y. F., Zhang, X. L., Lin, H., Zhang, R. J., & Xiao, H. Y. (2020). Stable oxygen isotope constraints on nitrate formation in Beijing in springtime. *Environmental Pollution*, *263*. https://doi.org/10.1016/j.envpol.2020.114515

Luo, L., Zhu, R. guo, Song, C. B., Peng, J. F., Guo, W., Liu, Y., Zheng, N., Xiao, H., & Xiao, H. Y. (2021). Changes in nitrate accumulation mechanisms as PM2.5 levels increase on the North China Plain: A perspective from the dual isotopic compositions of nitrate. *Chemosphere*, *263*. https://doi.org/10.1016/j.chemosphere.2020.127915

Ma, J., Shi, H., Zhu, Y., Li, R., Wang, S., Lu, N., Yao, Y., Bian, Z., & Huang, K. (2025). The Evolution of Global Surface Ammonia Concentrations during 2001-2019: Magnitudes, Patterns, and Drivers. *Environmental Science and Technology*. https://doi.org/10.1021/acs.est.4c14020

Ma, X., Tan, Z., Lu, K., Yang, X., Liu, Y., Li, S., Li, X., Chen, S., Novelli, A., Cho, C., Zeng, L., Wahner, A., & Zhang, Y. (2019). Winter photochemistry in Beijing: Observation and model simulation of OH and HO2 radicals at an urban site. *Science of the Total Environment*, *685*, 85–95. https://doi.org/10.1016/j.scitotenv.2019.05.329

Mahowald, N. M. (2008). Global distribution of atmospheric phosphorus sources, concentrations and deposition rates, and anthropogenic impacts. *Global Biogeochemical Cycles, 22*, GB4026. https://doi.org/10.1029/2008GB003240

Mahowald, N.M (2011). Aerosol indirect effect on biogeochemistry and climate. *Science, 334*(6057), 794–796. https://doi.org/10.1126/science.1207374

Martin, L. D., Krunkosky, T. M., Dye, J. A., Fischer, B. M., Jiang, N. F., Rochelle, L. G., Akley, N. J., Dreher, K. L., & Adler1, K. B. (1997). The Role of Reactive Oxygen and Nitrogen Species in the Response of Airway Epithelium to Particulates. In *Environ Health Perspect* (Vol. 1, Issue 5).

McElroy, M. B., & Wang, Y. X. (2005). Human and animal wastes: Implications for atmospheric N2O and NOx. *Global Biogeochemical Cycles*, *19*(2), 1–8. https://doi.org/10.1029/2004GB002429

Michalski, G., Bhattacharya, S. K., & Girsch, G. (2014). NOx cycle and the tropospheric ozone isotope anomaly: An experimental investigation. *Atmospheric Chemistry and Physics*, *14*(10), 4935–4953. https://doi.org/10.5194/acp-14-4935-2014

Michalski, G., Bhattacharya, S. K., & Mase, D. F. (2012). Oxygen Isotope Dynamics of Atmospheric Nitrate and Its Precursor Molecules. In M. Baskaran (Ed.), *Handbook of Environmental Isotope Geochemistry: Vol I* (pp. 613–635). Springer Berlin Heidelberg. https://doi.org/10.1007/978-3-642-10637-8_30

Mishra, D., & Goyal, P. (2014). Estimation of vehicular emissions using dynamic emission factors: A case study of Delhi, India. *Atmospheric Environment*, *98*, 1–7. https://doi.org/10.1016/j.atmosenv.2014.08.047

Mishra, S., Tripathi, S. N., Kanawade, V. P., Haslett, S. L., Dada, L., Ciarelli, G., Kumar, V., Singh, A., Bhattu, D., Rastogi, N., Daellenbach, K. R., Ganguly, D., Gargava, P., Slowik, J. G., Kulmala, M., Mohr, C., El-Haddad, I., & Prevot, A. S. H. (2023). Rapid night-time nanoparticle growth in Delhi driven by biomass-burning emissions. *Nature Geoscience*, *16*(3), 224–230. https://doi.org/10.1038/s41561-023-01138-x

Morin, S., Savarino, J., Frey, M. M., Domine, F., Jacobi, H. W., Kaleschke, L., & Martins, J. M. F. (2009). Comprehensive isotopic composition of atmospheric nitrate in the Atlantic Ocean boundary layer from 65°S to 79°N. *Journal of Geophysical Research Atmospheres*, *114*(5). https://doi.org/10.1029/2008JD010696

Nah, T., Guo, H., Sullivan, A. P., Chen, Y., Tanner, D. J., Nenes, A., Russell, A., Lee Ng, N., Gregory Huey, L., & Weber, R. J. (2018). Characterization of aerosol composition, aerosol acidity, and organic acid partitioning at an agriculturally intensive rural southeastern US site. *Atmospheric Chemistry and Physics*, *18*(15), 11471–11491. https://doi.org/10.5194/acp-18-11471-2018

Nenes, A., & Pandis, S. N. (1998). ISORROPIA: A New Thermodynamic Equilibrium Model for Multiphase Multicomponent Inorganic Aerosols. In *Aquatic Geochemistry* (Vol. 4).

Nenes, A., Pandis, S. N., Kanakidou, M., Russell, A. G., Song, S., Vasilakos, P., Weber, R. J., & Nenes, A. (2021). Aerosol acidity and liquid water content regulate the dry deposition of inorganic reactive nitrogen. *Atmospheric Chemistry and Physics*, *21*(8), 6023–6033. https://doi.org/10.5194/acp-21-6023-2021

Nenes, A., Pandis, S. N., Weber, R. J., & Russell, A. (2020). Aerosol pH and liquid water content determine when particulate matter is sensitive to ammonia and nitrate availability. *Atmospheric Chemistry and Physics*, *20*(5), 3249–3258. https://doi.org/10.5194/acp-20-3249-2020

Ni, Y., Luo, L., Liu, S., Huang, J., Li, Y., & Qi, J. (2024). Refined source apportionment of nitrate aerosols based on isotopes and emission inventories in coastal city of northern China. *Science of the Total Environment*, *957*. https://doi.org/10.1016/j.scitotenv.2024.177388

Nieder, R., & Benbi, D. K. (2022). Reactive nitrogen compounds and their influence on human health: an overview. In *Reviews on Environmental Health* (Vol. 37, Issue 2, pp. 229–246). De Gruyter Open Ltd. https://doi.org/10.1515/reveh-2021-0021

Nojiri, R., Osada, K., Kurosaki, Y., Matsuoka, M., & Sadanaga, Y. (2022). Variations in gaseous nitric acid concentrations at Tottori, Japan: Long-range transport from the Asian continent and local production. *Atmospheric Environment*, *274*. https://doi.org/10.1016/j.atmosenv.2022.118988

Ojha, N., Sharma, A., Kumar, M., Girach, I., Ansari, T. U., Sharma, S. K., Singh, N., Pozzer, A., & Gunthe, S. S. (2020). On the widespread enhancement in fine particulate matter across the Indo-Gangetic Plain towards winter. *Scientific Reports*, *10*(1). https://doi.org/10.1038/s41598-020-62710-8

Pan, Y., Tian, S., Liu, D., Fang, Y., Zhu, X., Gao, M., Gao, J., Michalski, G., & Wang, Y. (2018). Isotopic evidence for enhanced fossil fuel sources of aerosol ammonium in the urban atmosphere. *Environmental Pollution*, *238*, 942–947. https://doi.org/10.1016/j.envpol.2018.03.038

Pan, Y., Tian, S., Liu, D., Fang, Y., Zhu, X., Zhang, Q., Zheng, B., Michalski, G., & Wang, Y. (2016). Fossil Fuel Combustion-Related Emissions Dominate Atmospheric Ammonia Sources during Severe Haze Episodes: Evidence from 15N-Stable Isotope in Size-Resolved Aerosol Ammonium. *Environmental Science and Technology*, *50*(15), 8049–8056. https://doi.org/10.1021/acs.est.6b00634

Park, Y. mi, Park, K. su, Kim, H., Yu, S. min, Noh, S., Kim, M. seob, Kim, J. young, Ahn, J. young, Lee, M. do, Seok, K. seol, & Kim, Y. hee. (2018). Characterizing isotopic compositions of TC-C, NO3−-N, and NH4+-N in PM2.5 in South Korea: Impact of China's winter heating. *Environmental Pollution*, *233*, 735–744. https://doi.org/10.1016/j.envpol.2017.10.072

Patel, A., & Rastogi, N. (2023). Oxidative Potential of Atmospheric Aerosols over Different Regions of India and Surrounding Oceans. *ACS Earth and Space Chemistry*, *7*(12), 2582–2592. https://doi.org/10.1021/acsearthspacechem.3c00250

Patel, A., Satish, R., & Rastogi, N. (2021). Remarkably High Oxidative Potential of Atmospheric PM2.5Coming from a Large-Scale Paddy-Residue Burning over the Northwestern Indo-Gangetic Plain. *ACS Earth and Space Chemistry*, *5*(9), 2442–2452. https://doi.org/10.1021/acsearthspacechem.1c00125

Pathak, B., Bhuyan, P. K., Gogoi, M., & Bhuyan, K. (2012). Seasonal heterogeneity in aerosol types over Dibrugarh-North-Eastern India. *Atmospheric Environment*, *47*, 307–315. https://doi.org/10.1016/j.atmosenv.2011.10.061

Pawar, P. V., Mahajan, A. S., & Ghude, S. D. (2024). HONO chemistry and its impact on the atmospheric oxidizing capacity over the Indo-Gangetic Plain. In *Science of the Total Environment* (Vol. 947). Elsevier B.V. https://doi.org/10.1016/j.scitotenv.2024.174604

Payne, R. J., Dise, N. B., Field, C. D., Dore, A. J., Caporn, S. J. M., & Stevens, C. J. (2017). Nitrogen deposition and plant biodiversity: past, present, and future. *Frontiers in Ecology and the Environment*, *15*(8), 431–436. https://doi.org/10.1002/fee.1528

Peel, J. L., Haeuber, R., Garcia, V., Russell, A. G., & Neas, L. (2013). Impact of nitrogen and climate change interactions on ambient air pollution and human health. *Biogeochemistry*, *114*(1–3), 121–134. https://doi.org/10.1007/s10533-012-9782-4

Pikmann, J., Drewnick, F., Fachinger, F., & Borrmann, S. (2024). Particulate emissions from cooking: emission factors, emission dynamics, and mass spectrometric analysis for different cooking methods. *Atmospheric Chemistry and Physics*, *24*(21), 12295–12321. https://doi.org/10.5194/acp-24-12295-2024

Porter, E. M., Bowman, W. D., Clark, C. M., Compton, J. E., Pardo, L. H., & Soong, J. L. (2013). Interactive effects of anthropogenic nitrogen enrichment and climate change on terrestrial and aquatic biodiversity. *Biogeochemistry*, *114*(1–3), 93–120. https://doi.org/10.1007/s10533-012-9803-3

Puthussery, J. V, Dave, J., Shukla, A., Gaddamidi, S., Singh, A., Vats, P., Salana, S., Ganguly, D., Rastogi, N., Tripathi, S. N., & Verma, V. (2022). Effect of Biomass Burning, Diwali Fireworks, and Polluted Fog Events on the Oxidative Potential of Fine Ambient Particulate Matter in Delhi, India. *Environmental Science & Technology*, *56*(20), 14605–14616. https://doi.org/10.1021/acs.est.2c02730

Rai, P., Furger, M., El Haddad, I., Kumar, V., Wang, L., Singh, A., Dixit, K., Bhattu, D., Petit, J. E., Ganguly, D., Rastogi, N., Baltensperger, U., Tripathi, S. N., Slowik, J. G., & Prévôt, A. S. H. (2020). Real-time measurement and source apportionment of elements in Delhi's atmosphere. *Science of the Total Environment*, *742*. https://doi.org/10.1016/j.scitotenv.2020.140332

Rajput, P., Sarin, M. M., Sharma, D., & Singh, D. (2014). Organic aerosols and inorganic species from post-harvest agricultural-waste burning emissions over northern India: Impact on mass absorption efficiency of elemental carbon. *Environmental Science: Processes and Impacts*, *16*(10), 2371–2379. https://doi.org/10.1039/c4em00307a

Rastogi, N., Agnihotri, R., Sawlani, R., Patel, A., Babu, S. S., & Satish, R. (2020). Chemical and isotopic characteristics of PM10 over the Bay of Bengal: Effects of continental outflow on a marine environment. *Science of the Total Environment*, *726*. https://doi.org/10.1016/j.scitotenv.2020.138438

Rastogi, N., Singh, A., Sarin, M. M., & Singh, D. (2016). Temporal variability of primary and secondary aerosols over northern India: Impact of biomass burning emissions. *Atmospheric Environment*, *125*, 396–403. https://doi.org/10.1016/j.atmosenv.2015.06.010

Reisen, F., Meyer, C. P. M., & Keywood, M. D. (2013). Impact of biomass burning sources on seasonal aerosol air quality. *Atmospheric Environment*, *67*, 437–447. https://doi.org/10.1016/j.atmosenv.2012.11.004

Renard, J. J., Calidonna, S. E., & Henley, M. V. (2004). Fate of ammonia in the atmosphere - A review for applicability to hazardous releases. In *Journal of Hazardous Materials* (Vol. 108, Issues 1–2, pp. 29–60). https://doi.org/10.1016/j.jhazmat.2004.01.015

Sahu, S. K., Beig, G., & Parkhi, N. S. (2012). Emerging pattern of anthropogenic NOX emission over Indian subcontinent during 1990s and 2000s. *Atmospheric Pollution Research*, *3*(3), 262–269. https://doi.org/10.5094/APR.2012.021

Sahu, S. K., Mangaraj, P., Beig, G., Samal, A., Chinmay Pradhan, Dash, S., & Tyagi, B. (2021). Quantifying the high resolution seasonal emission of air pollutants from crop residue burning in India. *Environmental Pollution*, *286*. https://doi.org/10.1016/j.envpol.2021.117165

Saraswati, Sharma, S. K., & Mandal, T. K. (2018). Five-year measurements of ambient ammonia and its relationships with other trace gases at an urban site of Delhi, India. *Meteorology and Atmospheric Physics*, *130*(2), 241–257. https://doi.org/10.1007/s00703-017-0512-2

Satish, R., Rastogi, N., Singh, A., & Singh, D. (2020). Change in characteristics of water-soluble and water-insoluble brown carbon aerosols during a large-scale biomass burning. *Environmental Science and Pollution Research*, *27*, 33339–33350. https://doi.org/10.1007/s11356-020-09388-7/Published

Saud, T., Mandal, T. K., Gadi, R., Singh, D. P., Sharma, S. K., Saxena, M., & Mukherjee, A. (2011). Emission estimates of particulate matter (PM) and trace gases (SO2, NO and NO2) from biomass fuels used in rural sector of Indo-Gangetic Plain, India. *Atmospheric Environment*, *45*(32), 5913–5923. https://doi.org/10.1016/j.atmosenv.2011.06.031

Savard, M. M., Cole, A., Smirnoff, A., & Vet, R. (2017). Δ15N values of atmospheric N species simultaneously collected using sector-based samplers distant from sources – Isotopic inheritance and fractionation. *Atmospheric Environment*, *162*, 11–22. https://doi.org/10.1016/j.atmosenv.2017.05.010

Savarino, J., Morin, S., Erbland, J., Grannec, F., Patey, M. D., Vicars, W., Alexander, B., & Achterberg, E. P. (2013). Isotopic composition of atmospheric nitrate in a tropical marine boundary layer. *Proceedings of the National Academy of Sciences of the United States of America*, *110*(44), 17668–17673. https://doi.org/10.1073/pnas.1216639110

Scott, W. D., & Cattell, F. C. R. (1978). *Vapor pressure of ammonium sulphates*. https://doi.org/https://doi.org/10.1016/0004-6981(79)90174-4

Seinfeld, J. H. , P. S. N. ,.(2016). From Air Pollution to Climate Change. In *Atmospheric Chemistry and Physics*. 3rd Edition

Seinfeld, J. H., Pandis, S. N., & Noone, K. (1998). Atmospheric Chemistry and Physics: From Air Pollution to Climate Change. *Physics Today*, *51*(10), 88–90. https://doi.org/10.1063/1.882420

Seitzinger, S. P., Harrison, J. A., Dumont, E., Beusen, A. H. W., & Bouwman, A. F. (2005). Sources and delivery of carbon, nitrogen, and phosphorus to the coastal zone: An overview of Global Nutrient Export from Watersheds (NEWS) models and their application. *Global Biogeochemical Cycles, 19*, GB4S01. https://doi.org/10.1029/2005GB002606

Sharma, G., Sinha, B., Pallavi, Hakkim, H., Chandra, B. P., Kumar, A., & Sinha, V. (2019). Gridded Emissions of CO, NOx, SO2, CO2, NH3, HCl, CH4, PM2.5, PM10, BC, and NMVOC from Open Municipal Waste Burning in India. *Environmental Science and Technology*, *53*(9), 4765–4774. https://doi.org/10.1021/acs.est.8b07076

Sharma, S. K., Kotnala, G., & Mandal, T. K. (2020). Spatial Variability and Sources of Atmospheric Ammonia in India: A Review. In *Aerosol Science and Engineering* (Vol. 4, Issue 1). Springer. https://doi.org/10.1007/s41810-019-00052-3

Sharma, S. K., Mandal, T. K., Shenoy, D. M., Bardhan, P., Srivastava, M. K., Chatterjee, A., Saxena, M., Saraswati, Singh, B. P., & Ghosh, S. K. (2015). Variation of Stable Carbon and Nitrogen Isotopic Composition of PM10 at Urban Sites of Indo Gangetic Plain (IGP) of India. *Bulletin of Environmental Contamination and Toxicology*, *95*(5), 661–669. https://doi.org/10.1007/s00128-015-1660-z

Shaw, C., Rastogi, N., Mandal, R., & Sanyal, P. (2025). Formation pathways of particulate NO3− and sources of its precursor over the northwest India: Insights through dual isotopes. *Atmospheric Environment*, *360*, 121426. https://doi.org/10.1016/j.atmosenv.2025.121426

Shaw, C., Rastogi, N., Rathi, A., Kumar, S., & Meena, R. (2024). Sources and processes affecting the abundances of atmospheric NHx using δ15N over northwestern Indo-Gangetic plain. *Chemosphere*, *359*. https://doi.org/10.1016/j.chemosphere.2024.142356

Shi, X., Nenes, A., Xiao, Z., Song, S., Yu, H., Shi, G., Zhao, Q., Chen, K., Feng, Y., & Russell, A. G. (2019). High-Resolution Data Sets Unravel the Effects of Sources and Meteorological Conditions on Nitrate and Its Gas-Particle Partitioning. *Environmental Science and Technology*, *53*(6), 3048–3057. https://doi.org/10.1021/acs.est.8b06524

Shiraiwa, M., Selzle, K., & Pöschl, U. (2012). Hazardous components and health effects of atmospheric aerosol particles: reactive oxygen species, soot, polycyclic aromatic compounds and allergenic proteins. *Free Radical Research*, *46*(8), 927–939. https://doi.org/10.3109/10715762.2012.663084

Shiraiwa, M., Ueda, K., Pozzer, A., Lammel, G., Kampf, C. J., Fushimi, A., Enami, S., Arangio, A. M., Fröhlich-Nowoisky, J., Fujitani, Y., Furuyama, A., Lakey, P. S. J., Lelieveld, J., Lucas, K., Morino, Y., Pöschl, U., Takahama, S., Takami, A., Tong, H., … Sato, K. (2017). Aerosol Health Effects from Molecular to Global Scales. In *Environmental Science and Technology* (Vol. 51, Issue 23, pp. 13545–13567). American Chemical Society. https://doi.org/10.1021/acs.est.7b04417

Singh, A., Patel, A., Satish, R., Tripathi, S. N., & Rastogi, N. (2023). Wintertime oxidative potential of PM2.5 over a big urban city in the central Indo-Gangetic Plain. *Science of The Total Environment*, *905*, 167155. https://doi.org/https://doi.org/10.1016/j.scitotenv.2023.167155

Singh, A., Rastogi, N., Patel, A., & Singh, D. (2016). Seasonality in size-segregated ionic composition of ambient particulate pollutants over the Indo-Gangetic Plain: Source apportionment using PMF. *Environmental Pollution*, *219*, 906–915. https://doi.org/10.1016/j.envpol.2016.09.010

Singh, N., Mittal, S. K., Agarwal, R., Awasthi, A., & Gupta, P. K. (2010). Impact of rice crop residue burning on levels of SPM, SO2 and NO2 in the ambient air of Patiala (India). *International Journal of Environmental Analytical Chemistry*, *90*(10), 829–843. https://doi.org/10.1080/03067310903023874

Singh, T., Ravindra, K., Beig, G., & Mor, S. (2021). Influence of agricultural activities on atmospheric pollution during post-monsoon harvesting seasons at a rural location of Indo-Gangetic Plain. *Science of the Total Environment*, *796*. https://doi.org/10.1016/j.scitotenv.2021.148903

Singh, V., Biswal, A., Kesarkar, A. P., Mor, S., & Ravindra, K. (2020). High resolution vehicular PM10 emissions over megacity Delhi: Relative contributions of exhaust and non-exhaust sources. *Science of the Total Environment*, *699*. https://doi.org/10.1016/j.scitotenv.2019.134273

Sofen, E. D., Alexander, B., Steig, E. J., Thiemens, M. H., Kunasek, S. A., Amos, H. M., Schauer, A. J., Hastings, M. G., Bautista, J., Jackson, T. L., Vogel, L. E., Mcconnell, J. R., Pasteris, D. R., & Saltzman, E. S. (2014). WAIS Divide ice core suggests sustained changes in the atmospheric formation pathways of sulfate and nitrate since the 19th century in the extratropical Southern Hemisphere. *Atmospheric Chemistry and Physics*, *14*(11), 5749–5769. https://doi.org/10.5194/acp-14-5749-2014

Sommer, S. G., Webb, J., & Hutchings, N. D. (2019). New Emission Factors for Calculation of Ammonia Volatilization From European Livestock Manure Management Systems. In *Frontiers in Sustainable Food Systems* (Vol. 3). Frontiers Media S.A. https://doi.org/10.3389/fsufs.2019.00101

Song, S., Gao, M., Xu, W., Shao, J., Shi, G., Wang, S., Wang, Y., Sun, Y., & McElroy, M. B. (2018). Fine-particle pH for Beijing winter haze as inferred from different thermodynamic equilibrium models. *Atmospheric Chemistry and Physics*, *18*(10), 7423–7438. https://doi.org/10.5194/acp-18-7423-2018

Song, T., Feng, M., Song, D., Zhou, L., Qiu, Y., Tan, Q., & Yang, F. (2022). Enhanced nitrate contribution during winter haze events in a megacity of Sichuan Basin, China: Formation mechanism and source apportionment. *Journal of Cleaner Production*, *370*. https://doi.org/10.1016/j.jclepro.2022.133272

Song, W., Wang, Y. L., Yang, W., Sun, X. C., Tong, Y. D., Wang, X. M., Liu, C. Q., Bai, Z. P., & Liu, X. Y. (2019). Isotopic evaluation on relative contributions of major NOx sources to nitrate of PM2.5 in Beijing. *Environmental Pollution*, *248*, 183–190. https://doi.org/10.1016/j.envpol.2019.01.081

Srinivas, B., & Sarin, M. M. (2013). Atmospheric deposition of N, P and Fe to the Northern Indian Ocean: Implications to C- and N-fixation. *Science of the Total Environment*, *456–457*, 104–114. https://doi.org/10.1016/j.scitotenv.2013.03.068

Stock, B. C., Jackson, A. L., Ward, E. J., Parnell, A. C., Phillips, D. L., & Semmens, B. X. (2018). Analyzing mixing systems using a new generation of Bayesian tracer mixing models. *PeerJ*, *2018*(6). https://doi.org/10.7717/peerj.5096

Stock, B., & Semmens, B. (2017). *MixSIAR GUI User Manual v3.1*. https://doi.org/10.5281/zenodo.47719

Sudheer, A. K., & Rengarajan, R. (2015). Time-resolved inorganic chemical composition of fine aerosol and associated precursor gases over an urban environment in western India: Gas-aerosol equilibrium characteristics. *Atmospheric Environment*, *109*, 217–227. https://doi.org/10.1016/j.atmosenv.2015.03.028

Sun, K., Tao, L., Miller, D. J., Pan, D., Golston, L. M., Zondlo, M. A., Griffin, R. J., Wallace, H. W., Leong, Y. J., Yang, M. M., Zhang, Y., Mauzerall, D. L., & Zhu, T. (2017). Vehicle Emissions as an Important Urban Ammonia Source in the United States and China. *Environmental Science and Technology*, *51*(4), 2472–2481. https://doi.org/10.1021/acs.est.6b02805

Textor, C., Schulz, M., Guibert, S., Kinne, S., Balkanski, Y., Bauer, S., Berntsen, T., Berglen, T., Boucher, O., Chin, M., Dentener, F., Diehl, T., Easter, R., Feichter, H., Fillmore, D., Ghan, S., Ginoux, P., Gong, S., Grini, A., … Tie, X. (2006). Analysis and quantification of the diversities of aerosol life cycles within AeroCom. In *Atmos. Chem. Phys* (Vol. 6). www.atmos-chem-phys.net/6/1777/2006/

Thiruvengadam, A., Besch, M., Carder, D., Oshinuga, A., Pasek, R., Hogo, H., & Gautam, M. (2016). Unregulated greenhouse gas and ammonia emissions from current technology heavy-duty vehicles. *Journal of the Air & Waste Management Association*, *66*(11), 1045–1060. https://doi.org/10.1080/10962247.2016.1158751

Thode, H. G., & Urey, H. C. (1939). The further concentration of N15. *The Journal of Chemical Physics*, *7*(1), 34–39. https://doi.org/10.1063/1.1750320

Thomas, R. Q., Canham, C. D., Weathers, K. C., & Goodale, C. L. (2010). Increased tree carbon storage in response to nitrogen deposition in the United States. *Nature Geoscience, 3*(1), 13–17. https://doi.org/10.1038/ngeo721

Tomasi, C., & Lupi, A. (2017). *Primary and Secondary Sources of Atmospheric Aerosol*.

Tripathi, S. N., Yadav, S., & Sharma, K. (2024). Air pollution from biomass burning in India. In *Environmental Research Letters* (Vol. 19, Issue 7). Institute of Physics. https://doi.org/10.1088/1748-9326/ad4a90

Urey, H. C. (1947). The thermodynamic properties of isotopic substances. Liversidge lecture, delivered before the Chemical Society in the Royal Institution on December 18th, 1946. *Journal of the Chemical Society (Resumed)*, 562–581. https://doi.org/10.1039/jr9470000562

Urey, H. C., Huffman, J. R., Thode, H. G., & Fox, M. (1937). Concentration of N15 by chemical methods. *The Journal of Chemical Physics*, *5*(11), 856–868. https://doi.org/10.1063/1.1749954

Van Damme, M., Clarisse, L., Whitburn, S., Hadji-Lazaro, J., Hurtmans, D., Clerbaux, C., & Coheur, P. F. (2018). Industrial and agricultural ammonia point sources exposed. *Nature*, *564*(7734), 99–103. https://doi.org/10.1038/s41586-018-0747-1

Venkataraman, C., Habib, G., Kadamba, D., Shrivastava, M., Leon, J. F., Crouzille, B., Boucher, O., & Streets, D. G. (2006). Emissions from open biomass burning in India: Integrating the inventory approach with high-resolution Moderate Resolution Imaging Spectroradiometer (MODIS) active-fire and land cover data. *Global Biogeochemical Cycles*, *20*(2). https://doi.org/10.1029/2005GB002547

Viana, M., Pey, J., Querol, X., Alastuey, A., de Leeuw, F., & Lükewille, A. (2014). Natural sources of atmospheric aerosols influencing air quality across Europe. *Science of the Total Environment*, *472*, 825–833. https://doi.org/10.1016/j.scitotenv.2013.11.140

Vicars, W. C., Morin, S., Savarino, J., Wagner, N. L., Erbland, J., Vince, E., Martins, J. M. F., Lerner, B. M., Quinn, P. K., Coffman, D. J., Williams, E. J., & Brown, S. S. (2013). Spatial and diurnal variability in reactive nitrogen oxide chemistry as reflected in the isotopic composition of atmospheric nitrate: Results from the CalNex 2010 field study. *Journal of Geophysical Research Atmospheres*, *118*(18), 10,567-10,588. https://doi.org/10.1002/jgrd.50680

Vinken, G. C. M., Boersma, K. F., Maasakkers, J. D., Adon, M., & Martin, R. V. (2014). Worldwide biogenic soil NOxemissions inferred from OMI NO2observations. *Atmospheric Chemistry and Physics*, *14*(18), 10363–10381. https://doi.org/10.5194/acp-14-10363-2014

Vira, J., Hess, P., Melkonian, J., & Wieder, W. R. (2020). An improved mechanistic model for ammonia volatilization in Earth system models: Flow of Agricultural Nitrogen version 2 (FANv2). *Geoscientific Model Development*, *13*(9), 4459–4490. https://doi.org/10.5194/gmd-13-4459-2020

Wærsted, E. G., Sundvor, I., Denby, B. R., & Mu, Q. (2022). Quantification of temperature dependence of NOx emissions from road traffic in Norway using air quality modelling and monitoring data. *Atmospheric Environment: X*, *13*. https://doi.org/10.1016/j.aeaoa.2022.100160

Walters, W. W., Chai, J., & Hastings, M. G. (2019). Theoretical Phase Resolved Ammonia-Ammonium Nitrogen Equilibrium Isotope Exchange Fractionations: Applications for Tracking Atmospheric Ammonia Gas-to-Particle Conversion. *ACS Earth and Space Chemistry*, *3*(1), 79–89. https://doi.org/10.1021/acsearthspacechem.8b00140

Walters, W. W., Goodwin, S. R., & Michalski, G. (2015). Nitrogen stable isotope composition (δ15N) of vehicle-emitted NOx. *Environmental Science and Technology*, *49*(4), 2278–2285. https://doi.org/10.1021/es505580v

Walters, W. W., & Michalski, G. (2015). Theoretical calculation of nitrogen isotope equilibrium exchange fractionation factors for various NOy molecules. *Geochimica et Cosmochimica Acta*, *164*, 284–297. https://doi.org/10.1016/j.gca.2015.05.029

Walters, W. W., & Michalski, G. (2016). Theoretical calculation of oxygen equilibrium isotope fractionation factors involving various NOy molecules, OH, and H2O and its implications for isotope variations in atmospheric nitrate. *Geochimica et Cosmochimica Acta*, *191*, 89–101. https://doi.org/10.1016/j.gca.2016.06.039

Walters, W. W., Simonini, D. S., & Michalski, G. (2016). Nitrogen isotope exchange between NO and NO2 and its implications for δ15N variations in tropospheric NOx and atmospheric nitrate. *Geophysical Research Letters*, *43*(1), 440–448. https://doi.org/10.1002/2015GL066438

Walters, W. W., Song, L., Chai, J., Fang, Y., Colombi, N., & Hastings, M. G. (2020). *Constraining Ammonia Emissions in Vehicle Plumes Utilizing Nitrogen Stable Isotopes*. https://doi.org/10.5194/acp-2020-188

Walters, W. W., Tharp, B. D., Fang, H., Kozak, B. J., & Michalski, G. (2015). Nitrogen Isotope Composition of Thermally Produced NOx from Various Fossil-Fuel Combustion Sources. *Environmental Science and Technology*, *49*(19), 11363–11371. https://doi.org/10.1021/acs.est.5b02769

Wang, H., Lu, K., Chen, X., Zhu, Q., Wu, Z., Wu, Y., & Sun, K. (2018). Fast particulate nitrate formation via N2O5 uptake aloft in winter in Beijing. *Atmospheric Chemistry and Physics*, *18*(14), 10483–10495. https://doi.org/10.5194/acp-18-10483-2018

Wang, P., Cao, J., Tie, X., Wang, G., Li, G., Hu, T., Wu, Y., Xu, Y., Xu, G., Zhao, Y., Ding, W., Liu, H., Huang, R., & Zhan, C. (2015). Impact of meteorological parameters and gaseous pollutants on PM2.5 and PM10 mass concentrations during 2010 in Xi'an, China. *Aerosol and Air Quality Research*, *15*(5), 1844–1854. https://doi.org/10.4209/aaqr.2015.05.0380

Wang, Y., Zhang, Q. Q., He, K., Zhang, Q., & Chai, L. (2013). Sulfate-nitrate-ammonium aerosols over China: Response to 2000-2015 emission changes of sulfur dioxide, nitrogen oxides, and ammonia. *Atmospheric Chemistry and Physics*, *13*(5), 2635–2652. https://doi.org/10.5194/acp-13-2635-2013

Warner, J. X., Wei, Z., Larrabee Strow, L., Dickerson, R. R., & Nowak, J. B. (2016). The global tropospheric ammonia distribution as seen in the 13-year AIRS measurement record. *Atmospheric Chemistry and Physics*, *16*(8), 5467–5479. https://doi.org/10.5194/acp-16-5467-2016

Webb, J. (2001). *Estimating the potential for ammonia emissions from livestock excreta and manures*. https://doi.org/https://doi.org/10.1016/S0269-7491(00)00090-7

Weber, R. J., Guo, H., Russell, A. G., & Nenes, A. (2016). High aerosol acidity despite declining atmospheric sulfate concentrations over the past 15 years. *Nature Geoscience*, *9*(4), 282–285. https://doi.org/10.1038/ngeo2665

Weng, H., Lin, J., Martin, R., Millet, D. B., Jaeglé, L., Ridley, D., Keller, C., Li, C., Du, M., & Meng, J. (2020). Global high-resolution emissions of soil NOx, sea salt aerosols, and biogenic volatile organic compounds. *Scientific Data*, *7*(1). https://doi.org/10.1038/s41597-020-0488-5

Whitburn, S., Van Damme, M., Kaiser, J. W., Van Der Werf, G. R., Turquety, S., Hurtmans, D., Clarisse, L., Clerbaux, C., & Coheur, P. F. (2015). Ammonia emissions in tropical biomass burning regions: Comparison between satellite-derived emissions and bottom-up fire inventories. *Atmospheric Environment*, *121*, 42–54. https://doi.org/10.1016/j.atmosenv.2015.03.015

Woo Jeong, J., Baek, S., Park, S., Lee, S., Lim, Y., & Lee, K. (2024). Trends in NOx and NH3 emissions caused by three-way catalysts. *Fuel*, *366*, 131282. https://doi.org/https://doi.org/10.1016/j.fuel.2024.131282

Wu, C., Wang, G., Li, J., Li, J., Cao, C., Ge, S., Xie, Y., Chen, J., Liu, S., Du, W., Zhao, Z., & Cao, F. (2020). Non-agricultural sources dominate the atmospheric NH3 in Xi'an, a megacity in the semi-arid region of China. *Science of the Total Environment*, *722*. https://doi.org/10.1016/j.scitotenv.2020.137756

Wu, L., Ren, H., Wang, P., Chen, J., Fang, Y., Hu, W., Ren, L., Deng, J., Song, Y., Li, J., Sun, Y., Wang, Z., Liu, C. Q., Ying, Q., & Fu, P. (2019). Aerosol Ammonium in the Urban Boundary Layer in Beijing: Insights from Nitrogen Isotope Ratios and Simulations in Summer 2015. *Environmental Science and Technology Letters*, *6*(7), 389–395. https://doi.org/10.1021/acs.estlett.9b00328

Wu, L., Yue, S., Shi, Z., Hu, W., Chen, J., Ren, H., Deng, J., Ren, L., Fang, Y., Yan, H., Li, W., Harrison, R. M., & Fu, P. (2021). Source forensics of inorganic and organic nitrogen using δ15N for tropospheric aerosols over Mt. Tai. *Npj Climate and Atmospheric Science*, *4*(1). https://doi.org/10.1038/s41612-021-00163-0

Wyer, K. E., Kelleghan, D. B., Blanes-Vidal, V., Schauberger, G., & Curran, T. P. (2022). Ammonia emissions from agriculture and their contribution to fine particulate matter: A review of implications for human health. In *Journal of Environmental Management* (Vol. 323). Academic Press. https://doi.org/10.1016/j.jenvman.2022.116285

Xi, D., Xiao, Y., Mgelwa, A. S., & Kuang, Y. (2023). Formation pathways and source apportionments of inorganic nitrogen-containing aerosols in urban environment: Insights

from nitrogen and oxygen isotopic compositions in Guangzhou, China. *Atmospheric Environment*, *309*. https://doi.org/10.1016/j.atmosenv.2023.119888

Xiao, H., Ding, S., & Li, X. (2024). Sources of NH4+ in PM2.5 and Their Seasonal Variations in Urban Tianjin China: New Insights From the Seasonal δ15N Values of NH3 Source. *Journal of Geophysical Research: Atmospheres*, *129*(9). https://doi.org/10.1029/2023JD040169

Xiao, H. W., Wu, J. F., Luo, L., Liu, C., Xie, Y. J., & Xiao, H. Y. (2020). Enhanced biomass burning as a source of aerosol ammonium over cities in central China in autumn. *Environmental Pollution*, *266*. https://doi.org/10.1016/j.envpol.2020.115278

Xiao, H. W., Zhu, R. G., Pan, Y. Y., Guo, W., Zheng, N. J., Liu, Y. H., Liu, C., Zhang, Z. Y., Wu, J. F., Kang, C. A., Luo, L., & Xiao, H. Y. (2020). Differentiation Between Nitrate Aerosol Formation Pathways in a Southeast Chinese City by Dual Isotope and Modeling Studies. *Journal of Geophysical Research: Atmospheres*, *125*(13). https://doi.org/10.1029/2020JD032604

Xin, K., Chen, J., & Soyol-Erdene, T. O. (2023). Formation mechanism and source apportionment of nitrate in atmospheric aerosols. *APN Science Bulletin*, *2023*(13), 102–111. https://doi.org/10.30852/SB.2023.2225

Yadav, I. C., & Devi, N. L. (2019). Biomass burning, regional air quality, and climate change. In *Encyclopedia of Environmental Health* (pp. 386–391). Elsevier. https://doi.org/10.1016/B978-0-12-409548-9.11022-X

Yadav, S., Katoch, A., Singh, Y., & Kulshrestha, U. C. (2023). Abundance and variation of gaseous NH3 in relation with inorganic fertilizers and soil moisture during Kharif and Rabi season. *Environmental Monitoring and Assessment*, *195*(1). https://doi.org/10.1007/s10661-022-10777-3

Yamaji, K., Ohara, T., & Akimoto, H. (2004). Regional-specific emission inventory for NH3, N2O, and CH4 via animal farming in South, Southeast, and East Asia. *Atmospheric Environment*, *38*(40 SPEC.ISS.), 7111–7121. https://doi.org/10.1016/j.atmosenv.2004.06.045

Yienger, J. J., & Levy II, H. (1995). Empirical model of global soil-biogenic NOχ emissions. *Journal of Geophysical Research: Atmospheres*, *100*(D6), 11447–11464. https://doi.org/https://doi.org/10.1029/95JD00370

Zaehle, S., Friend, A., Friedlingstein, P., Dentener, F., Peylin, P., & Schulz, M. (2010). Carbon and nitrogen dynamics in the O-CN land surface model: 2. Role of the nitrogen cycle in the historical terrestrial carbon balance. *Global Biogeochemical Cycles, 24*(1), GB1006. https://doi.org/10.1029/2009GB003522

Zeldovich, Y. B., & Sunyaev, R. A. (1992). *25. The Oxidation of Nitrogen in Combustion and Explosions*. https://api.semanticscholar.org/CorpusID:99591855

Zhang, C., Geng, X., Wang, H., Zhou, L., & Wang, B. (2017). Emission factor for atmospheric ammonia from a typical municipal wastewater treatment plant in South China. *Environmental Pollution*, *220*, 963–970. https://doi.org/10.1016/j.envpol.2016.10.082

Zhang, K., Liu, S., Wu, N., & Xu, W. (2022). Isotopic components and source analysis of inorganic nitrogen in coastal aerosols of the Yellow Sea. *Frontiers in Marine Science*, *9*. https://doi.org/10.3389/fmars.2022.993160

Zhang, Y., Benedict, K. B., Tang, A., Sun, Y., Fang, Y., & Liu, X. (2019). Persistent Nonagricultural and Periodic Agricultural Emissions Dominate Sources of Ammonia in Urban Beijing: Evidence from 15N Stable Isotope in Vertical Profiles. *Environmental Science and Technology*. https://doi.org/10.1021/acs.est.9b05741

Zhang, Y., Benedict, K. B., Tang, A., Sun, Y., Fang, Y., & Liu, X. (2020). Persistent Nonagricultural and Periodic Agricultural Emissions Dominate Sources of Ammonia in Urban Beijing: Evidence from 15N Stable Isotope in Vertical Profiles. *Environmental Science and Technology*, *54*(1), 102–109. https://doi.org/10.1021/ACS.EST.9B05741

Zhang, Y. L., Zhang, W., Fan, M. Y., Li, J., Fang, H., Cao, F., Lin, Y. C., Wilkins, B. P., Liu, X., Bao, M., Hong, Y., & Michalski, G. (2022). A diurnal story of Δ17O(NO3−) in urban Nanjing and its implication for nitrate aerosol formation. *Npj Climate and Atmospheric Science*, *5*(1). https://doi.org/10.1038/s41612-022-00273-3

Zhang, Z., Tian, C., Liang, Y., & Zheng, N. (2021). Recent Isotopic Evidence for Elevated Vehicular NOx Emission to Atmospheric Nitrate Formation in Chinese Megacities. *ACS Earth and Space Chemistry*, *5*(9), 2372–2379. https://doi.org/10.1021/acsearthspacechem.1c00166

Zhang, Z., Zeng, Y., Zheng, N., Luo, L., Xiao, H., & Xiao, H. (2020). Fossil fuel-related emissions were the major source of NH3 pollution in urban cities of northern China in the autumn of 2017. *Environmental Pollution*, *256*. https://doi.org/10.1016/j.envpol.2019.113428

Zhu, F., Gilliam, F. S., Mulder, J., Yoh, M., Mo, J., & Lu, X. (2022). Effects of Excess Nitrogen (N) on Fine Root Growth in Tropical Forests of Contrasting N Status. *Forests*, *13*(8). https://doi.org/10.3390/f13081328

Zhu, Y., Zhou, S., Li, H., Luo, L., Wang, F., Bao, Y., & Chen, Y. (2021). Formation pathways and sources of size-segregated nitrate aerosols in a megacity identified by dual isotopes. *Atmospheric Environment*, *264*. https://doi.org/10.1016/j.atmosenv.2021.118708

List of Publications

Shaw, C., *Rastogi, N., Mandal, R. and Sanyal, P., 2025. Formation pathways of particulate NO3- and sources of its precursor over the northwest India: Insights through dual isotopes. Atmospheric Environment, 121426. https://doi.org/10.1016/j.atmosenv.2025.121426* ***(Publication related to thesis)***

Shaw, C.*, Rastogi, N., Rathi, A., Kumar, S. and Meena, R., 2024. Sources and processes affecting the abundances of atmospheric NHx using δ15N over northwestern Indo-Gangetic Plain. Chemosphere, 142356. https://doi.org/10.1016/j.chemosphere.2024.142356* ***(Publication related to thesis)***

Shaw, C., *Sarkar, S., Kumar, S., and Rastogi, N. 2023. High release of isotopically depleted CO2 and CH4 from the photo-degradation of plastic: A pilot laboratory study, Physics and Chemistry of the Earth, Parts A/B/C, 103474. https://doi.org/10.1016/j.pce.2023.103474*